Ultra-Low Frequency Standing Alfvén Waves: Global Magnetospheric Modeling of Resonant Wave-Wave Interactions

by

Sidney Ellington

A dissertation submitted in partial fulfillment
of the requirements for the degree of
Doctor of Philosophy
(Applied Physics)
in The University of Michigan
2016

Doctoral Committee:

Professor Mark Moldwin, Chair
professor Michael Balikhin
Research Scientist Natalia Ganushkina
Professor Michael Liemohn

TABLE OF CONTENTS

LIST OF FIGURES iv

ABSTRACT ix

CHAPTER

I. Introduction 1

1.1 Ultra-Low Frequency Geomagnetic Pulsations 1
1.2 Ideal Magnetohydrodynamic Eigenmodes 4
1.3 Excitation Mechanisms 8
1.3.1 Solar wind Dynamic Pressure Fluctuations 10
1.3.2 Internal Instabilities 11
1.4 Wave-Wave Coupling Mechanisms 16
1.4.1 Linear Resonances 19
1.4.2 Nonlinear Parametric Resonances 21
1.5 Global Magnetospheric Modeling of Ultra-Low Frequency Waves 25
1.5.1 Global Model 27
1.6 Outline of Thesis 30

II. Field Line Resonances and Local Time Asymmetries 32

2.1 Introduction 33
2.2 Methodology and Simulation Results 37
2.2.1 Global Model 37
2.2.2 Field Line Resonance Signatures 42
2.2.3 Signatures of Asymmetries in FLR Amplitudes . . . 42
2.3 Discussion 48
2.3.1 Demonstration of FLRs 48
2.3.2 Potential Sources of Asymmetry 51
2.4 Conclusion 54

III. Oblique Parametric Decay Instability of Standing Magnetospheric Surface Waves: Nonlinear Resonant Coupling to Internal Magnetotail Kink Modes 57

3.1 Introduction: Nonlinear Resonances and Internal Kink Modes in the Terrestrial Magnetosphere 58
3.2 Methodology: Variation of Solar wind Speed, Ionospheric Conductance, and Differences in Local Plasma Properties 62
3.3 Parametric Excitation of Standing Magnetopause Surface Waves: Mode Characteristics 66
3.4 Parametric Decay Instability: Excitation of Obliquely-Propagating Daughter Waves 78
3.4.1 Transverse and Longitudinal Waves: Frequency, Amplitude, and Second-Harmonic Generation 88
3.4.2 Induced Density Fluctuations: Implied Ponderomotive Forces 93
3.4.3 Mode Coupling and the Application of Conservation Laws: Conservation of Energy and Phase Space Evolution 98
3.5 Magnetotail Kink Mode Waves: Propagation of Daughter Waves through Magnetotail 102
3.5.1 Wave Spectra and Counterpropagating Modes . . . 103
3.5.2 Induced Density and Temperature Fluctuations . . 105
3.6 Discussion and Summary: Numerical Constraints, Cold Dense Plasma Sheet Ions, Magnetotail Dynamics, and Dawn-Dusk Asymmetries 108

IV. Conclusion 110

BIBLIOGRAPHY 114

LIST OF FIGURES

Figure

1.1 From *Jacobs et al.,* 1964: Classification scheme for geomagnetic pulsations. 2

1.2 *Credit: NASA*. Global view of the magnetosphere with labeled structures. 4

1.3 From *Hughes et al.* [1994]: Illustration of toroidal (left) and poloidal (right) field line resonances with fundamental and second harmonics on top and bottom, respectively. 20

1.4 Graphical illustration of the different components of the Space Weather Modeling Framework (SWMF). We use the Global Magnetospheric and Ionospheric Electrodynamics Models exclusively. 27

2.1 Solar wind dynamic pressure as a function of simulation time with an embedded power spectral density plotted in log scale showing a uniform distribution of frequencies between 0 and 100 mHz. The dynamic p_{dyn} fluctuations increase linearly in amplitude starting three hours into the simulation. The fluctuations at the end of the simulation are approximately 100 percent of the mean and span 3 nPa peak-to-peak. 39

2.2 Number density profiles taken along the 1500 and 900 LTs at various radii. Note the small, modulated time-dependent variation. 41

2.3 The radial power spectral density along the 1500 LT meridian shows at least three well-defined harmonics as indicated by the WKB estimated eigenfrequencies. Note the radial resonance widths, determined primarily by the ionospheric Pedersen conductance. 43

2.4 The radial cross-phase along the 1500 LT with WKB estimated eigenfrequencies. The phase reversals show the location of the FLR, except for the region closest to the inner boundary, which may be the location of the turning point. 44

2.5 a) Ratio of the time-averaged spectral energy in the compressive B_z fields in the postnoon and prenoon sectors along radial cuts from the inner boundary through to the magnetopause spanning from 800 to 1600 LT. Regions of the curves above 1 indicate that more energy in the postnoon sector, and vice versa. b) Same as (a) but for the radial electric fields, E_r. c) Coupling efficiency as measured by the ratio of the time-averaged spectral energy of the radial electric and compressional magnetic fields. Note the marginal local time asymmetry and general increase in efficiency moving outward from the noon meridian. 46

2.6 a) Time-averaged spectral energy of the radial electric field postnoon/prenoon ratios at L=6 and L=8 for the first and third harmonics and across the entire spectral range as a function of simulation time. Each spectral component shows distinct time-dependent behavior. b) Coupling efficiency as a function of simulation time comparing the 1500 and 900 LT meridians at L=6, 8 and 10. The time variation is bounded with marginal post/prenoon asymmetry. Note that the coupling efficiency decreases moving sunward. 47

2.7 a),b), and c) show time-averaged dayside equatorial wave energy maps of the radial electric field with side plots capturing the radial and local time variation therein at color-coded locations for the [5,10],[10,15], and [15,20] mHz spectral bands. These maps illustrate the global structure of the shear eigenmodes. The pre/postnoon asymmetries are clearly identifiable. 49

3.1 Logarithmic scale of solar wind temperature fluctuations with a linearly increasing amplitude profile after the three hour mark. 63

3.2 Equatorial maps, clockwise from the top left, of the magnitude of the transverse Alfvén waves, field-aligned current density, plasma beta, and field-aligned electric field at four hours into the simulation run. These snapshots occur at the maximum azimuthal extent of the magnetotail kink modes. 65

3.3 Illustration of the large-amplitude transverse Alfvén waves normalized to the background field, B_{z0}, four hours into the simulation where we observe maximum azimuthal penetration across the magnetotail. The wave distribution suggests an internal kink mode externally driven by magnetopause surface waves seen propagating tailward from the dayside. 66

3.4 Spatiotemporal contour maps along the dawn-side magnetopause of representative detrended MHD state variables: $\delta|\mathbf{B}_{x,y}|$, δB_z, δn, δj_x, δj_y, δj_z, δu_x, δu_y, and δu_z. These data illustrate significant magnetopause surface wave structures. 67

3.5 Line plots of MHD state variables sampled from within the magnetopause at 640, 600, and 520 LT. Transverse and longitudinal wave signatures are clearly distinguishable by frequency. Note the amplitude modulation in the the magnetic field and current density variables and the additional lower frequency wave component in B_z at 600 and 520 LT. These features suggest and illustrate the products of the transition to a parametrically unstable regime. 70

3.6 Power spectral densities of the compressional B_z field (red lines) and number density (blue line) along the magnetopause. Note the excitation of 1.5 mHz monochromatic signals in B_z and n and an additional 0.5 mHz signal in B_z near the dawn-terminator. B_z and n appear to decouple–no longer spatially linearly correlated–at 640 and 520 LT. 71

3.7 Power spectral density of transverse wave component B_y at the 600 LT meridian with an inset of the Lissajous curves of the equatorial transverse wave components sampled along the magnetopause. . . . 72

3.8 Moving time average with two hour time windows of spectral energies along the magnetopause of: *top*, B_y, and *bottom*, v_A bandpass filtered between 1 and 2 mHz. Correspondence between characteristic shapes of curves indicates strong correlation between 1.5 mHz fluctuations in the Alfvén wave speed and the 0.73 mHz fluctuations in the standing Alfvén wave modes. This may be suggestive of a nonlinear excitation mechanism. 73

3.9 Characteristic wave and magnetosheath flow speeds sampled along local times from 640 to 420 LT. While the magnetosheath flow speed monotonically increases towards the solar wind speed of 600 km/s, the sum of the Alfvén and sound speeds decrease accordingly. Flow speeds are supersonic $U_{sh} > c_A$ all along this stretch of magnetopause but become super-Alfvénic between 540 and 500 LT. This transition allows magnetopause surface waves to become spatially oscillatory within the magnetosphere. 79

3.10 Global structure of transverse Alfvén wave component B_x in the equatorial plane illustrating the time-integrated spectral energy in two frequency bands and spatiotemporal contour plots along azimuthal and radial cuts. 80

3.11 Global structure of transverse Alfvén wave component B_y in the equatorial plane illustrating the time-integrated spectral energy in two frequency bands and spatiotemporal contour plots along azimuthal and radial cuts. 83

3.12 Global structure of longitudinal wave component B_z in the equatorial plane illustrating the time-integrated spectral energy in two frequency bands and spatiotemporal contour plots along azimuthal and radial cuts. 85

3.13 2D and 3D spectrographs of B_y, B_z, and n at the 440 LT meridian. Refer to Figure 3.16 for details. 89

3.14 2D and 3D spectrographs of B_y, B_z, and n at the 520 LT meridian. Refer to Figure 3.16 for details. 90

3.15 2D and 3D spectrographs of B_y, B_z, and n at the 600 LT meridian. Refer to Figure 3.16 for details. 91

3.16 2D and 3D spectrographs of B_y, B_z, and number density n at 640 LTs with PSDs sampled along radial segment in a neighborhood spanning several R_E of the magnetopause. The spatial overlap of the two transverse spectral signals is co-located with signicant power in the density and compressional waves at 0.5 mHz. 92

3.17 *Top*: Normalized, time-averaged density fluctuations over spectral band spanning beat frequencies of shear modes as a function of radii. *Middle*: Time-averaged projection of pump to daughter shear modes–beat waves–as a function of radii. *Bottom*: Plot of top to middle figure spatially-averaged from 10 to 16 R_E depicting expected linear relationship between induced density fluctuations and amplitude of beat waves. Linear relationship implies ponderomotive acceleration. 94

3.18 Phase space evolution of B_y component of tranverse wave modes starting from magnetopause locations–plots along first column–at 600, 540, 520, and 500 LT moving Earthward by 0.5 R_E increments. Inscribed elliptical structures indicate the presence of an additional co-propagating, coupled wave mode. 99

3.19 Line plots of phase-locked transverse modes along 440 LT across the magnetopause. The phase difference of nearly 0 degrees indicates mode coupling. 100

3.20 Stacked line plots of time series of B_y component from -130 to -149 degrees (bottom to top) longitude depicting amplitude structure of transverse waves as they propagate azimuthally through the magnetotail from the dawn flank. Regions of notable wave steepening of backward and forward-propagating wave populations are marked. . 104

3.21 Global structure of the number density and thermal pressure taken along semi-circular rays with constant radiis of 10, 12, 14, and 16 R_E spanning from 600 to 1800 LT across magnetotail. Note the spatiotemporally localized depressions in n and p. 106

3.22 Line plots of MHD state variables at -138 degrees longitude and 16 R_E from Earth center. Shaded areas with vertical line indicate times where we observed an enhancement in the amplitude of the transverse kink modes with associated depression in number and field-aligned current densities. 107

ABSTRACT

Ultra-Low Frequency Standing Alfvén Waves: Global Magnetospheric Modeling of Resonant Wave-Wave Interactions

by

Sidney Ellington

Chair: Mark Moldwin

Alfvén waves are an important energy transport modality in the collisionless plasmas that dominate Earth's magnetosphere. While wave-particle interactions are well understood, the mechanisms that govern wave-wave interactions and their associated phenomenological impacts are still poorly understood and have received little attention. To examine both linear and nonlinear resonant mode coupling, we use the Space Weather Modeling Framework (SWMF) with a resistive, ionospheric inner boundary with ideal MHD governing equations in order to explore the excitation of field line resonances and the stability of standing Alfvén waves along the magnetopause by using synthetic upstream solar wind drivers. In reproducing the essential features of broadband FLRs, we found multi-faceted local time FLR asymmetries not exclusively determined by correlated asymmetries in the compressional driver. In examining the stability of transverse magnetopause surface waves, we found evidence of an oblique parametric decay instability exciting large-scale, counterpropagating magnetotail kink modes via ponderomotive forces mediated by transverse magnetic beat waves. The latter is responsible for a backward-propagating compressional wave along the mag-

netopause. These magnetotail waves bear the signature of slow magnetosonic-shear Alfvénic coupling with associated density holes and soliton-like transverse waves with strong field-aligned currents. Our results have significant implications for magnetotail dynamics and the energization of radiation belts in the dayside magnetospheric cavity and is the first study to examine a) negative energy surface waves, b) parametric decay instability of transverse magnetopause surface waves, c) ponderomotive forces via magnetic beat waves, d) the coupling of MP surface waves to magnetotail kink mode waves, e) counterpropagating kink mode waves, and f) the coupling of slow magnetosonic and transverse wave modes.

CHAPTER I

Introduction

1.1 Ultra-Low Frequency Geomagnetic Pulsations

The interaction of Earths dipole magnetic field with the magnetized, supersonic plasma emanating from the sun known as the solar wind is the basis for an entire class of phenomenological, theoretical, and numerical modeling problems that constitute the field of magnetospheric physics. The solar wind acts as an outer boundary for the terrestrial magnetosphere that results from this interaction with a low-density, predominately low energy collisionless, multi-component plasma pervading the billions of cubic kilometers within. Since most of the convective dynamics therein occur at spatiotemporal scales much greater than the ion gyroradius where most of the plasma remains electromagnetically frozen to field lines, the plasma is often modeled as a fluid. The study of governing behavior of plasmas embedded within magnetic and electric fields on such scales is known as magnetohydrodynamics, and this framework forms the basis of our approach in this dissertation. The collisionless plasmas of the terrestrial magnetosphere support a gamut of magnetic perturbations known collectively as Alfvén waves [*Alfvén*, 1942]. These modes have characteristic dispersion relations–the fundamental relationship between the wavenumber, phase speed, and angular frequency, polarizations, and propagation angles that allow us to discern their excitation and generation mechanisms and determine how they propagate through-

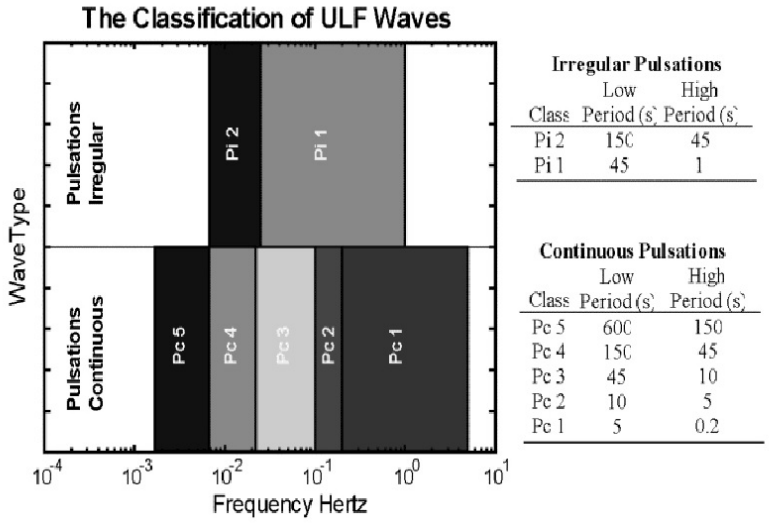

Figure 1.1: From *Jacobs et al.,* 1964: Classification scheme for geomagnetic pulsations.

out the magnetosphere. Since the magnetospheric plasmas are inhomogeneous with regions with large gradients in density, temperature, or magnetic curvature, the construction of these dispersion relations through either theoretical investigation or *in situ* measurements is important for determining how these waves interact with the plasma and with other wave modes. A particular class of Alfvén waves known as ultra-low frequency (ULF) geomagnenetic pulsations plays a large role in magnetospheric dynamics. This is because for all positive spectral indices, the lowest frequency components carry most of the wave energy by several orders of magnitude. With finite wavelengths approaching the characteristic size of the magnetospheric cavities, they can nonlocally impact plasma dynamics on global scales. A classification scheme divides these waves into continuous or impulsive waves for a range of wave periods, and the frequencies range from sub- millihertz up to the ion cyclotron frequencies as seen in Figure 1. This is to say that most of these wave modes can be modeled self-consistently with the ideal MHD governing equations, which suggests that ULF waves are synonymous with the ideal MHD wave eigenmodes. We study here ULF waves in the Pc5 and Pc6 class, or waves with frequencies between 0.2 to 25 mHz.

Multi-point observational measurements of ULF wave signatures–electric and magnetic field and associated bulk plasma fluctuations–via ground-based magnetometers and *in situ* satellite measurements have elucidated and helped form questions to many aspects of wave dynamics within the magnetosphere [*Engebretson et al.*, 1987; *Takahashi et al.*, 1998]. For example, the excitation and role of ULF waves in substorms and the aurorae, the energetization of the radiation belts, field-line resonances and cavity/waveguide modes, and shear flow instabilities all have a history borne from these efforts. However, satellites sample only a tiny fraction of the volume of the magnetosphere, and ground-based magnetometers are constrained to sample field-aligned, 'line of sight' magnetic disturbances for ULF wave phenomena that are not so spatiotemporally confined. Thus, global magnetospheric models using numerical simulations can offer unparalleled three dimensional space plus time information about the global structure and evolution of wave modes and give us the ability to perform detailed numerical experiments. However, it is important to note that global magnetospheric models are often limited by the sheer computational effort to perform fully three-dimensional, self-consistent simulations of field and particles. Simplifying assumptions are usually made to make these problems tractable–ideal MHD, and the numerical solutions have to be interpreted carefully to distinguish between what could reasonably be expected to occur in nature and what is ultimately a numerical artifact. In the next few chapters, we will construct the dispersion relations of the three ULF eigenmodes starting from the ideal magnetohydrodynamic equations of motions. After discussing both the internal and external excitation mechanisms of ULF waves, we will explore the linear and nonlinear coupling mechanisms that allow one ULF eigenmode to transform into another. Since we conduct this study using data from the global magnetospheric code the Space Weather Modeling Framework (SWMF), we briefly present the numerical schemes, physics and parameter-based modules that allow users to fully customized their global simulations to ever increasing degrees of

sophistication. The limitations of these models such as numerical diffusion, finite grid effects, and ultimately the breakdown of MHD is discussed last.

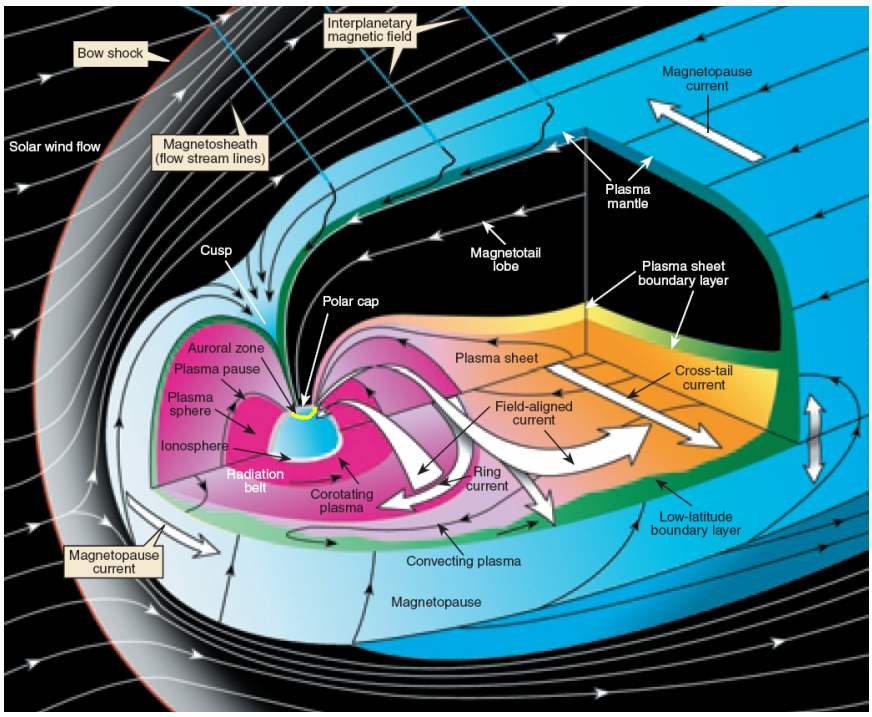

Figure 1.2: *Credit: NASA*. Global view of the magnetosphere with labeled structures.

1.2 Ideal Magnetohydrodynamic Eigenmodes

We begin the simple mathematical treatment of ULF waves with the single fluid ideal MHD equations, which are a set of nonlinear, coupled conservation laws governing the self-consistent interaction of fluid elements and electromagnetic fields. The assumptions that inform the ideal MHD equations are not insignificant. The range of permissible dynamics is restricted to periodicities greater than the ion gyroperiod, length scales greater than the ion gyroradius, and infinite heat conduction obeying local thermodynamic equilibria, which implies strong collisionality without explicit resistivity. Note that pressure is therefore isotropic, which completely eliminates an entire order of wave excitation and dissipation mechanisms. Without two-fluid– electron and ion fluids, even with strict quasi-neutrality, drift waves are not possible

solutions. Since the wave frequencies are sufficiently low, charge separation can be neglected as quasi-neutrality is maintained. The follow derivation follows from *Kivelson and Russell* [1995]. Lets begin with an ambient uniform magnetic field along the z direction, $B = B_0\hat{z}$, and consider waves with an arbitrary respective propagation angle, θ, in a finite temperature, homogeneous fluid. Incorporating Maxwells equations, the MHD equations are

$$\frac{\partial \rho}{\partial t} + \nabla(\rho \mathbf{u}) = 0 \tag{1.1}$$

$$\rho \frac{\partial \mathbf{u}}{\partial t} + \rho(\mathbf{u} \cdot \nabla)\mathbf{u} + \nabla \cdot \left[\left(p + \frac{B^2}{2 * \mu_0} \right) I - \frac{\mathbf{BB}}{\mu_0} \right] = 0 \tag{1.2}$$

$$\frac{\partial \mathbf{B}}{\partial t} + \nabla \cdot (\mathbf{uB} - \mathbf{Bu}) = 0 \tag{1.3}$$

$$\frac{1}{\gamma - 1}\frac{\partial \rho}{\partial t} + \frac{1}{\gamma - 1}(\mathbf{u} \cdot \nabla)p + \frac{\gamma}{\gamma - 1}p(\nabla \cdot \mathbf{u}) = 0 \tag{1.4}$$

$$\mathbf{E} = -\mathbf{u} \times \mathbf{B} \tag{1.5}$$

The MHD state variables are $\mathbf{B}$, $\mathbf{u}$, and ρ with an adiabatic index, γ, typically chosen to be 3/2. To find the MHD eigenmodes we expand these variables to first order about the equilibrium using a small perturbation (in practice, this perturbation is less than 10 percent of the equilibrium) such that

$$\rho = \rho_0 + \rho_1 \tag{1.6}$$

$$\mathbf{B} = \mathbf{B}_0 + \mathbf{B}_1 \tag{1.7}$$

$$\mathbf{u} = \mathbf{u}_1 \tag{1.8}$$

where we assume that the fluid is at rest and the quantities with subscript 1 are perturbed quantities. Note that to first order, large amplitude Alfvén waves where $\mathbf{B}_1/|\mathbf{B}_0| \sim 1$ cannot be treated with this approach. Substituting the perturbed state

variables into equations 1.1, 1.2, and 1.3 and collecting terms, the linearized MHD equations become

$$\frac{\partial \rho_1}{\partial t} + \nabla(\rho_0 \mathbf{u}_1) = 0 \tag{1.9}$$

$$\rho_0 \frac{\partial \mathbf{u}_1}{\partial t} + \rho(\mathbf{u} \cdot \nabla)\mathbf{u} + \nabla \cdot \left[\left(p + \frac{B^2}{2\mu_0} \right) I - \frac{\mathbf{BB}}{\mu_0} \right] = 0 \tag{1.10}$$

$$\frac{\partial \mathbf{B}_1}{\partial t} + \nabla \times (\mathbf{u}_1 \times \mathbf{B}_0) = 0. \tag{1.11}$$

By differentiating equation 1.10 with respect to time and using using equations 1.7 and 1.9, we get

$$\rho_0 \frac{\partial^2 \mathbf{u}_1}{\partial t^2} - c_S^2 \nabla(\nabla \cdot \mathbf{u}_1) + \mathbf{v}_A \times (\nabla \times (\nabla \times (\mathbf{u}_1 \times \mathbf{v}_A))) = 0 \tag{1.12}$$

$$\mathbf{v}_A = \frac{\mathbf{B}_0}{\sqrt{\mu_0 \rho_0}} \tag{1.13}$$

$$c_S = \sqrt{\frac{\gamma p_0}{\rho_0}}. \tag{1.14}$$

We can transform to the frequency domain by assuming the Fourier ansatz $\nabla \to ik$ and $\partial/\partial t \to -i\omega$ where $\omega = \omega(\mathbf{k})$ for plane wave solutions of $\mathbf{u}_1(\mathbf{r}, t) = \mathbf{u}_1 \exp(i\mathbf{k} \cdot \mathbf{r} - i\omega t)$ propagating with a phase velocity $v_{ph} = \omega/k$ in the $\mathbf{k}$-direction. This gives the dispersion relation for MHD eigenmodes as

$$-\omega^2 \mathbf{u}_1 + c_S^2(\mathbf{k} \cdot \mathbf{u}_1)k - v_A \times (\mathbf{k} \times (\mathbf{k} \times (\mathbf{u}_1 \times \mathbf{v}_A))) = 0 \tag{1.15}$$

We can expand the velocity vector perturbation into a Cartesian basis set and rewrite equation 1.15 to obtain an eigenfunction whose nontrivial eigenvalues yields

$$(\omega^2 - k^2 v_A^2 \cos^2 \omega)(\omega^4 - \omega^2 k^2 (v_A^2 + c_S^2) + k^4 v_A^2 c_s^2 \cos^2 \omega) = 0. \tag{1.16}$$

This equation yields four solutions with an additional limiting case. The first is the entropy mode for $\omega = 0$, which is satisfied for waves with infinite wavelength or vanishing phase speeds. The intermediate or shear Alfvén wave but generally thee transverse mode whose dispersion relation is given by

$$\omega = kv_A \cos\theta \tag{1.17}$$

with associated u_{1y} velocity fluctuations perpendicular to the background field. This eigenmode vanishes, however, or becomes degenerate with the entropy mode for perpendicular propagation and is decoupled from density or pressure perturbations since $\mathbf{k}\cdot\mathbf{u}_1 = 0$, which implies plasma temperature has no impact on its propagation or dispersion characteristics. The two remaining solutions to Equation 1.16 are the known as the *magnetosonic* or *compressional* waves or generally the *longitudinal* modes given by the solution

$$\omega_{\pm}^2 = \frac{1}{2}k^2\left(v_A^2 + c_S^2 \pm \sqrt{\left(v_A^2 + c_S^2\right)^2 - 4v_A^2 c_S^2 \cos^2\omega}\right) \tag{1.18}$$

where $\pm$ refers to the fast (FMS) and slow magnetosonic modes (SMS), respectively, where the phase speed of the fast mode is unconditionally greater than the slow mode. These waves have velocity perturbations u_{1x} , u_{1y} and associated density and pressure fluctuations. There are several differences that distinguish these modes. The slow mode cannot propagate perpendicular to the background field, and like the intermediate mode, becomes degenerate with the entropy mode. In this limit, the fast mode frequency reduces to $\omega_{fm}^2 = k^2(v_A^2 + c_S^2)$, where the magnitude of the sound and Alfvén waves speeds is known as the fast magnetosonic phase speed. The induced density fluctuations have distinct phase relations with the magnetosonic waves as well: these fluctuations are in phase with the FMS and out of phase with the SMS modes. We note that generally the relationship between the induced density fluctuations and the

magnetosonic modes is linear, which has experimental and theoretical implications. One limiting case is important. For plasma beta, β, much less than the one, where the sound speed is much less than the Alfvén speed, the slow wave becomes the sound wave given by the dispersion relation

$$\omega = kc_S \cos\theta. \tag{1.19}$$

In the dayside magnetosphere, we usually neglect the finite pressure and assume a zero temperature plasma, in which case the slow wave becomes degenerate with the shear Alfvén wave. As a closing comment, it is important to note that the ideal MHD wave eigenmodes are all non-dispersive, that is the phase velocity is linear with respect to the wavenumber. This, however, should not be taken to mean that the inhomogeneities within the magnetosphere do not introduce spatial dispersion, which can lead to ducting and nonlinear phenomena that can drive these wave modes to larger wavenumbers [*Sarris et al.*, 2009]. Some of these mechanisms include phase mixing and parametric decay instabilities. In either case, for ideal MHD, the solutions should obey self-similarity.

1.3 Excitation Mechanisms

The interaction of the solar wind with the magnetosphere is the predominant free energy source for the excitation of ULF waves, but magnetic and plasma structures internal to the magnetosphere ultimately control their propagation, dissipation, and decay or amplification through a large variety of mechanisms. Here we explore two general excitation mechanisms for ULF waves: solar wind dynamic pressure fluctuations and internal instabilities. Each generate ULF waves with unique spectral characteristics including polarization, amplitude, frequency, wavelength, and propagation vectors. Generations of spacecraft missions and ground-based magnetometer stations

have observed signatures of ULF waves and their transport of energy [*Engebretson et al.*, 1987]. Through drift-bounce resonances, ULF waves can energize radiation belt electrons [*Elkington et al.*, 1999]. Through the generation of field-aligned currents, they can energize ionospheric plasma to produce aurorae. The long-period magnetic perturbations associated with ULF waves can destabilize instabilities known to lead to magnetic reconnection in the nightside magnetotail. Each of these processes probably produces ULF waves. Magnetic reconnection itself likely produces Pi2 pulsations and broadband compressional waves and strong, field-aligned currents along the plasma sheet boundary layer as the rapid reorganization of the magnetic topology generates compressional shocks. The relaxation of ballooning instabilities can trigger these sorts of waves as well [*Cheng and Chian*, 1994]. And thermal ions in the ring current with thermal velocities greater than the local Alfvén speed can produce small azimuthal fast magnetosonic waves that can further energize ions downstream, leading to the relaxation of non-equilibrium distributions [*Ozeke and Mann*, 2008]. This process also applies to anisotropic distributions. Lastly, plasma sheet flapping driven by buoyancy-drag forces can excite long-wavelength fluctuations of the entire magnetotail, which although is not properly a MHD eigenmode per se, speaks to the paradigms that govern how large-scale phenomena can excite ULF waves [*Golovchanskaya and Maltsev*, 2005]. The fundamental idea here is that real observations of ULF wave phenomena taken *in situ* are different from results of numerical MHD simulations by one point of fact: actual data represent intrinsically *kinetic* wave dynamics. ULF waves are properly described by kinetic equations in the limit of small frequency ($\omega \ll \Omega_i$), and kinetic dynamics often mediate ULF phenomena. Field line resonances and magnetic reconnection are two examples. We keep this in mind when discussing the excitation mechanisms below.

1.3.1 Solar wind Dynamic Pressure Fluctuations

Fluctuations in the solar wind density, temperature, or bulk velocity can dynamically compress the dayside magnetosphere and directly drive periodic magnetopause displacements that can launch compressional waves into the magnetospheric cavity. A broadband spectra of fluctuations can drive broadband fast magnetosonic waves with amplitudes that increase proportionally with the solar wind dynamic pressure. These waves propagate isotropically from the subsolar point at the local Alfvén wave speed. The solar wind is often modeled as continuous series of planar fronts impinging on the magnetosphere, but irregularities in these fronts less than the characteristic surface area of the magnetosphere or finite IMF clock angle, e.g. non-zero B_y, can drive asymmetries in azimuthal mode structure and phase speed that impact the distribution of ULF wave amplitude, frequency, and polarization [*Lee and Lysak*, 1990]. Numerous statistical studies using multipoint measurements–satellites and ground-based magnetometers–have analyzed how variations in the solar wind structure correlate with the spectral characteristics of magnetospheric pulsations to conclude that the solar wind drives a majority of ULF wave occurrence rates [*Takahashi et al.*, 1998]. The propagation characteristics and frequency selection of ULF waves is an outstanding problem. Analysis of the ULF wave spectra suggest that some modes can be driven by wideband pressure pulses. The dayside magnetospheric cavity can trap fast mode waves between the magnetopause and ionospheric inner boundary, forming a discrete spectra with wavelengths comparable to the characteristic size of the magnetospheric cavity known as cavity modes. For waves that can propagate downtail past the dawn-dusk terminators, their spectra take on waveguide characteristics modified by the open magnetotail geometry [*Mann et al.*, 1999].

1.3.2 Internal Instabilities

Instabilities couple free energy to the growth of waves and generally require a finite amplitude perturbation to drive the plasma or wave from equilibrium. All plasma instabilities excite waves with unique spectral profiles. Some instabilities known to excite ULF waves in the Pc5 frequency range are the ballooning instabilities in the magnetotail and shear-flow instabilities along boundary layers such as the magnetopause and plasma sheet boundary layer [*Hasegawa*, 1969; *Cheng and Qian*, 1994; *Elkington et al.*, 1999]. Both instabilities are mediated by wave-particle interactions; the former involving the rapid relaxation of the stressed magnetic topology transferring free magnetic energy to ambient plasma, and the latter relative streaming of plasma providing the free energy for the growth of compressive perturbations. Other instabilities involve the stability of wave fields themselves, such as parametric decay or convective instabilities, which are mediated by field-aligned gradients in the transverse magnetic field and relative drift between the waves and plasma flow, respectively [*Cramer*, 1977]. By internal instabilities, we mean those of local origin proximate to or within the magnetosphere, including the magnetopause. For this dissertation, the primary instability excitation mechanism for ULF waves are shear- flow, which we discuss here. The Kelvin-Helmholtz instability along the magnetopause flanks is the most well- known shear-flow instability in plasma physics generated from the differential flow between two fluids and excites magnetopause (MP) surface waves with circular to elliptical polarization and phase velocities along the MP with about half the flow shear across the boundary layer [*Lee and Olson*, 1980]. Surface waves are waves that are trapped in the magnetic and/or electric equipotentials within the boundary layer or given an appropriate cut-off frequency are ducted along the layer. Consistent with linear treatments in the compressible regime, the wavenumbers with maximum growth rate depend on the thickness of the magnetopause boundary layer, d, such that the azimuthal mode number is $kd \sim 0.5 - 1.0$. In this case, physically, the

saturation of the KH modes depends on the boundary layer thickness or in numerical models the width of a grid cell, whichever is smaller. From *Lee and Olson* [1980] the onset criterion of the instability depends on the magnetosheath flow speeds, and magnetic field magnitude and density on either side of the boundary layer given by

$$\mathbf{v}^2 > \frac{1}{\mu_0 m_i}\left(\frac{1}{n_1}+\frac{1}{n_2}\right)\left(\mathbf{B}_1^2+\mathbf{B}_2^2\right). \tag{1.20}$$

Numerical studies conducted by *Guo et al.* [2010] and *Merkin et al.* [2013] have examined the generation and evolution of the KH instability for northward B_z while *Claudepierre et al.* [2008] used southward B_z using spectral techniques to determine where along the magnetopause these surface modes were generated and their wavelengths, phase speeds, and frequencies. Each found significant, solar wind speed dependent spectral power in the compressional fast mode B_z signature with frequencies between 2 and 5 mHz. While *Merkin et al.* [2013] reported observing evidence of field-aligned currents, no effort has been reported in the literature to examine the associated magnetic field components therein or their field-aligned structure. Additionally, in an attempt to explain the source of field line resonances–to be discussed later–observed in the outer magnetosphere near the flanks, many authors have invoked the coupling of KH surface waves to magnetic pulsations propagating through magnetospheric waveguides with a perfectly reflecting magnetopause and a frequency-dependent Earthward turning point serving as boundaries [*Samson et al.*, 1992; *Southwood and Kivelson*, 1990]. However, it is unclear whether these magnetic pulsations are simply the evanescent tails of the KH surface waves typically seen in global magnetospheric simulations sunward of the dawn-dusk terminators, or some decoupled magnetosonic wave mode freely propagating into the magnetosphere. And if these magnetic pulsations are the latter, these models have failed to suggest or substantiate a coupling mechanism that would permit this energy transport across the magne-

topause. In the latter case, *Pu and Kivelson* [1988] explain the transition from surface to body modes in compressible plasmas for varying magnetosheath flow speeds and propagation angles with respect to the mean, background field. For non-zero, finite sound speeds, only magnetosheath flow speeds which surpass the fast magnetosonic speed allow surface waves to couple to body modes that propagate transversely to the magnetopause, which suggests the coupling mechanism is a cusp resonance between fast mode waves. *Pu and Kivelson* [1988] did not address whether body modes could be slow magnetosonic waves even for non-transverse propagation angles where sound speeds greater than the Alfvén wave speed would readily admit such modes. This holds true on the nightside where the background magnetic field lies parallel to the magnetosheath flow and the density across the boundary layer is the same. However, this model does not address the impact turning points within the magnetosphere have on the body mode, which would only admit wavelengths less than the characteristic size of the waveguide. And even here, for the turning point to have an impact on the wave modes, it must lie close enough to the magnetopause so that the e-folding time of the body wave is greater than the coupling rate with the surface wave. For the typical nightside magnetic topology and Alfvén wave speed distribution in the equatorial plane for northward B_z, this imposes a local time dependent coupling paradigm [Turkakin et al., 2013]. Mann et al. [1998] examined the impact a bounded magnetosphere has on the excitation of global modes via KH surface waves. Generally, for super-Alfvénic ($U_{sh} > v_A + v_S$) flow speeds, the surface waves generate overreflected–reflection with amplification–waves within the magnetosphere with a characteristic azimuthal mode number of

$$k_y d = \frac{n\pi}{\left[(M+\delta)^2 - 1\right]^{1/2}} \tag{1.21}$$

where M is the Mach number, δ is the ratio of the sound to Alfvén wave speeds, n is the harmonic number, k_y is the wavenumber parallel to the magnetosheath flow, and d is the waveguide width bounded by the magnetopause and an Earthward turning point. He also suggests that for these flow speeds, the KH surface waves have negative Doppler-shifted frequencies, which suggests the coupling to global wave modes is mediated via negative energy surface waves. Since body waves carry energy away from the magnetopause, the KH instability saturates without an increase in wavenumber as its growth rate drops to zero. A bounded magnetosphere imposes constraints on the wavelength and frequency of body modes, but the Alfvén wave speed distribution across the flanks and magnetotail forces us to revisit the cusp resonance as the excitation mechanism of the waveguide modes. Typically the Alfvén wave speed drops considerably in crossing from thee magnetosheath into the plasma sheet past the dawn-dusk terminators, which rules out the cusp resonance as it requires the coupled wave modes to have the same phase velocity. Even then, finite beta and sound speeds along with the non-uniformity of the magnetic fields allow degenerate magnetoacoustic modes, specifically the generation of slow magnetosonic waves. For large amplitude surface waves with small wavenumbers propagating obliquely to the background field in this region of the magnetosphere, even small density perturbations and field-aligned spatial variations in wave amplitude can lead to parametric decay instabilities, which we revisit later [*Yumoto*, 1982]. These instabilities spawn backward-propagating–negative energy–waves and forward-propagating waves with half the frequency, a hierarchy of modes incidentally consistent with present theoretical treatments of KH surface waves [*Cramer*, 1977; *Mann et al.*, 1999]. To reconcile the gap in the theoretical treatment of the transition from surface to spatially-oscillatory wave modes, *Mills et al.* [1999] examined the excitation of fast and slow magnetoacoustic body modes by including oblique propagation in their analysis. Since the wave frequencies and phase speeds are modified by the propagation angle, the con-

straints imposed by local Alfvén and sound speeds on cusp resonances normal to the magnetopause are removed. In this way a spectrum of wave satisfying the dispersion relation for obliquely propagating modes are moderated only by the magnetosheath flow speeds and the KH instability criteria along the magnetopause, both given as functions of local time. This closes the time-dependent local coupling paradigm treatment of *Turkakin et al.* [2013]. This gives us scope to consider whether shear Alfvén waves could be excited by KH surface waves or whether slow magnetosonic waves may become degenerate with shear Alfvén waves on the nightside, where the magnetic topology often doesn't force this distinction. Since shear wave modes couple to the ionosphere, this opens up a line of profound questions concerning the mediation of magnetotail dynamics via ULF waves. But the KH instability is notoriously difficult to reproduce in global magnetospheric models using ideal and generally non-Hall constitutive relations. As will be discussed later, KH surface waves are nominally dispersive as their wavelengths decrease as the instability transitions to the nonlinear phase where magnetic reconnnection ultimately relaxes the stressed magnetic topology. The latter is a difficult problem on its own, but the dispersive character of the KH waves means the wavelengths rapidly approach the grid cell size, below which the numerical solution becomes untenable. As such, the KH instability in arguably most simulations remains in varying states of saturation while remaining marginally unstable. However, the shear flow at the magnetopause can produce other classes of surface wave solutions. Where the KH mode is predominately compressive, the Kruskal- Schwarzchild (KS) mode is transverse as it is a standing Alfvén wave along eld lines threading the magnetopause [*Plaschke and Glassmeier*, 2011]. While not technically an instability as it is overdamped by the finite ionospheric conductance at its magnetic footpoints, it draws its free energy from the magnetosheath flow and

has a growth rate given by its complex frequency

$$\omega_{KS} = k_z \frac{B_{0z} + B_{1z}}{\mu_0(\rho_0 + \rho_1)} \tag{1.22}$$

where the subscripts indicate values sampled on either side of the magnetopause and k_z is determined by the length of the field line [*Plaschke and Glassmeier*, 2011]. Solar wind dynamic pressure fluctuations are thought to initiate the coupling to the magnetosheath free energy by periodically modulating the diamagnetic currents and allowing non-resonant perturbations to couple evanescently to frequencies resonant with the local closed field lines [*Plaschke and Glassmeier*, 2011]. Now that we have examined both external and internal primary drivers of ULF waves that provide the free energy for their excitation, we will now focus on mechanisms that allow different ULF modes to couple via resonant wave-wave interactions.

1.4 Wave-Wave Coupling Mechanisms

Mode coupling of ULF waves in the terrestrial magnetosphere has received little attention from the space physics community except in a limited number of cases [*Southwood*, 1974; *Yumoto and Saito*, 1982; *Claudepierre et al.*, 2010]. Excluding the ionosphere where dispersive and kinetic effects dissipate ULF wave energy through an untold number of mechanisms, linear mode coupling phenomena such as field line resonances (FLR) is the only actively studied resonant wave-wave interaction in the magnetosphere. Other mechanisms such as phase mixing along boundary layers including the plasmapause and plasma sheet boundary layer allow incident ULF waves to mode convert to kinetic Alfvén waves [*Sarris et al.*, 2009]; but without self-interaction, this process is not accurately described as a wave-wave phenomena, turbulent cascades included. Large amplitude, high frequency plasma wave modes such as the lower hybrid and ion cyclotron waves are known from theoretical treatments to undergo parametric

decay, but very little attention has been paid to examining their signatures in observational data or within numerical simulations. Promising work from *Yumoto* [1982] sought to explain the occurrence of Pc3 waves in the inner magnetosphere from the nonlinear decay of obliquely propagating magnetosonic waves near the plasmapause, while *Chian* [1994] explained the spectrum of waves generated near the auroral region as the parametric decay of standing waves. Limited observational data of evidence of the decay instability in the bow shock has been reported [Spangler et al., 1997]. The propagation characteristics of ULF waves are important insofar as their ability to impact magnetosheric dynamics or interact with the plasma, and the ability of ULF waves to impact dynamics nonlocally due to its ability to propagate large distances without dissipation is precisely why examining mechanisms that allow ULF waves to transform to modes that can more readily interact with the plasma is important. The distinction between linear and nonlinear resonances is in the order of the dispersion relation. As we will see, the dispersion relation for linear resonances such as the FLR is first order with respect to frequency, whereas the lowest order of the parametric or modulational decay instabilities is fifth-order in frequency. Additionally, the polarization of wave modes impacts the coupling dynamics [*Cramer*, 1977]. Non-circularly polarized pump waves introduce higher-order parametric decay products including second-harmonic generation of compressive waves [*Cramer*, 1977; *Goldstein*, 1978]. Even then, kinetic treatments of FLRs show that kinetic Alfvén waves mediate the coupling of compressional to shear Alfvén waves with non-ideal, dispersive or resistive eects allowing additional nonlinear radiative phenomena from the resonance point, but this speaks more broadly to major differences between kinetic and MHD treatments of wave-wave interactions [*Bellan*, 1996]. Dispersion is nonlinear, and generally while the ideal MHD eigenmodes we will consider here are nondispersive, inhomogeneities in the magnetosphere such as the non-uniform Alfvén wave speed distribution introduce spatial dispersion that can nonlinearly impact the local coupling dynamics. And

since all of the phenomena we consider occur on or along field lines magnetically connected to the ionosphere, nonlocal dissipation of parallel propagating modes through resistive Joule heating can introduce nonlinear, complex damping terms that fundamentally alter the coupling of wave modes as well [*Southwood*, 1974]. So far we have discussed ULF waves and wave-wave coupling broadly in terms of their roles in energy transport, and this immediately forces us to see how the coupling dynamics obey conservation laws. This could be taken for granted since these dynamics are derived from the conservative MHD equations; however nonlocal ionospheric dissipation, numerical diffusion, and a milieu of transient dynamics within numerical simulations complicate this narrative, and usually we apply the conservation laws as a diagnostic mechanism to determine the nature of the wave-wave interactions anyway [*Hoshino and Goldstein*, 1989]. Other than the adiabatic invariants, which we can neglect since we are not considering wave-particle interactions (in ideal MHD, we can invoke the virial theorem to justify this), there are three basic conservation laws that wave-wave interactions must obey: the conservation of energy, the conservation of momentum, and the conservation of helicity [*Hoshino and Goldstein*, 1989]. Energy conservation means the sum of the frequencies of the excited waves must equal the frequency of the incident wave. For a linear resonance such as the FLR, this means that the fast mode wave frequency must equal the frequency of the shear Alfvén wave, or $\omega_F = \omega_A$. For nonlinear parametric decay instabilities, this means the frequency of the pump wave must equal the sum of the frequencies of the daughter waves, or $\omega_0 = \omega_1 + \omega_2$. While this should be understood in terms of the energy quanta of these waves taken in the quantum limit, which was the original conceptual formalism, the Manley-Rowe relations connect this to the wave powers such that for any two waves in a nonlinear coupling process,

$$\frac{P_1}{\omega_1} = \frac{P_2}{\omega_2} \tag{1.23}$$

where the frequencies can be complex where dissipative effects are included [*Hoshino and Goldstein*, 1989]. Momentum conservation is entirely analogous to the conservation of energy in that the wavenumbers add accordingly, where for linear and nonlinear interactions, $k_F = k_A$ and $k_0 = k_1 + k_2$, respectively, where for the latter, we assume that the FLR is local. Conservation of helicity requires that the senses of polarization are the same for each wave.

1.4.1 Linear Resonances

A field line resonance (FLR) involves the coupling of a compressional with a standing, shear Alfvén wave where $\omega = kv_A$ is the eigenfrequency determined by integrating the wave speed along a field line. The question of the source of these compressional waves aside–numerous studies have examined solar wind driven cavity/waveguide modes or internal instabilities, for plasma betas much less than 1, we can reproduce the essential equations for low azimuthal mode number FLRs [*Zhu and Kivelson*, 1988; *Southwood and Kivelson*, 1990]; *Samson et al.*, 1992]. For all azimuthal mode numbers, m, the compressional and shear modes are coupled. For low m numbers, the shear wave modes have a predominately toroidal polarization with field components of E_r and B_θ.

We restrict our analysis to the later case. By following one of the most straightforward derivations by *Southwood* [1974], the equations governing the coupling process are as follows. For the pressure streamlines given by

$$\psi = p + \mathbf{B}_0\mathbf{B}_1/\mu_0 \tag{1.24}$$

the one-dimensional equation of motion for the plasma displacements and pressure in ideal MHD are

$$\frac{d^2\xi_x}{dx^2} + \frac{(F/G)'}{(F/G)}\frac{d\xi_x}{dx} + G\xi_x = 0 \tag{1.25}$$

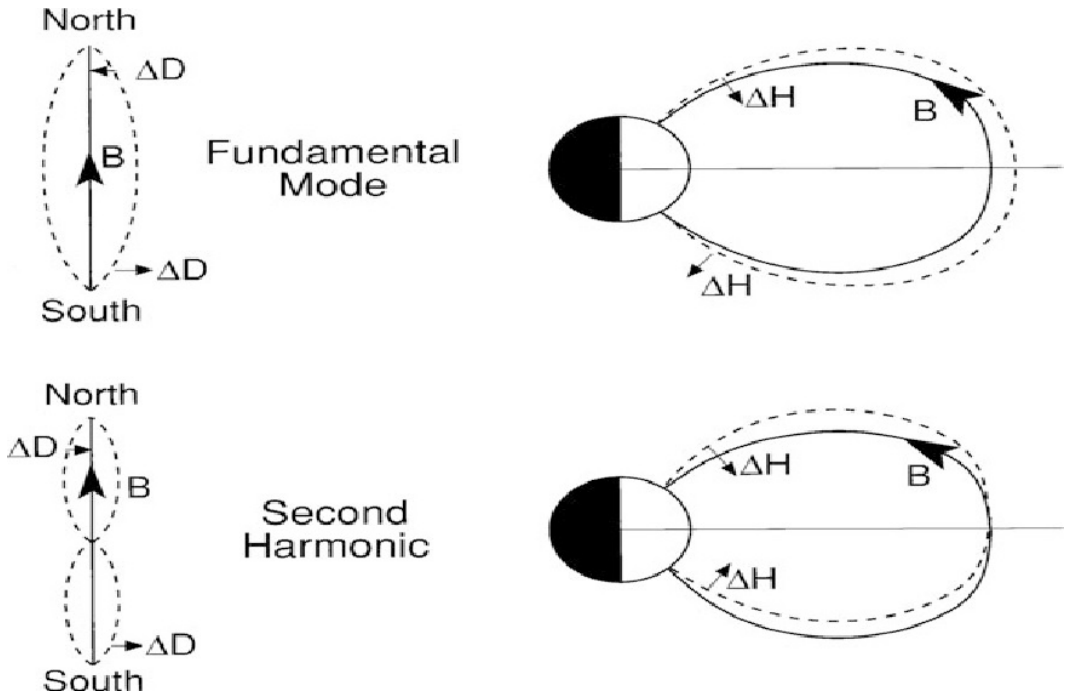

Figure 1.3: From *Hughes et al.* [1994]: Illustration of toroidal (left) and poloidal (right) field line resonances with fundamental and second harmonics on top and bottom, respectively.

and

$$\frac{d^2\psi}{dx^2} - \frac{F'}{F}\frac{d\psi}{dx} + G\psi = 0, \tag{1.26}$$

respectively, where F and G are given as

$$F(x) = \rho(\omega^2 - (\mathbf{k}\cdot\mathbf{v}_A)^2) \tag{1.27}$$

and

$$G(x) = \left(\frac{\omega}{v_A}\right)^2 - k_y^2 - k_z^2. \tag{1.28}$$

The primes denote spatial derivatives with respect to x. Solving these coupled equations yield the plasma displacements in x and y as

$$\xi_y = \frac{ik_y B_0 B_{1z}}{\mu_0\rho\left(\omega^2 - (\mathbf{k}\cdot\mathbf{v}_A)^2\right)} \tag{1.29}$$

and

$$\xi_y = \frac{d\psi/dx}{\rho\left(\omega^2 - (\mathbf{k}\cdot\mathbf{v}_A)^2\right)} \tag{1.30}$$

From the latter equations it is evidence that for ω near kv_A, the plasma displacements will experience a resonance, which is to say given a compressional driver whose frequency matches the local wave speed, a shear wave mode will be excited. The imaginary displacement in y ensures that the resonance condition must obey a 180 degree phase shift, but this actually varies in magnitude with azimuthal mode number [*Feinrich et al.*, 1997]. We note that for a bounded field line with resistive footpoints, an imaginary frequency component is added to the resonance condition, which plays the role of dissipation. This term depends on the ionospheric conductance and the local gradient in wave speed, and other than varying the equilibrium magnitude of the FLR, leaves the results of this basic analysis intact [*Southwood*, 1974].

1.4.2 Nonlinear Parametric Resonances

Nonlinear parametric resonances can be divided into two classes: the parametric decay and modulational instabilities for either parallel or obliquely propagating or standing magnetoacoustic or Alfvén pump waves. These waves can be elliptically or circularly polarized, and the local and nonlocal plasma beta, sound speed, and characteristic length of the field line or magnetospheric cavity. Here we briefly review the basic equations of the parametric decay instability because they guide our approach in sussing out the phenomenological observations therein within the magnetosphere by following the derivations and associated notations of Goldstein [1978] and Cramer [1977]. Given a pump wave with wavenumber k_0 and angular frequency ω_0 propagating along a background magnetic field in the z direction with perpendicular components in x and y,

$$\overline{\mathbf{B}}_\perp = \Re(B\exp[-i(k_0 z - \omega_0 t)]\hat{\mathbf{e}}_\pm \tag{1.31}$$

where

$$\hat{\mathbf{e}}_{\pm} = (\hat{\mathbf{x}} \pm \hat{\mathbf{y}})/\sqrt{2} \tag{1.32}$$

denotes circular polarization with left or right handedness. The analysis of *Yumoto et al.* [1982] shows that the pump wave amplitude must be finite, but the original analysis of *Goldstein* [1978] took the ansatz of a large amplitude–the fluctuations in the pump on the same order as the amplitude of the background magnetic field–wave for the basis of instability. The magnetic fluctuations of the excited daughter waves are denoted as $\mathbf{B}'_{\perp}$. Using the ideal MHD equations, we can expand the state variables v, ρ, and B by a small order parameter $\varepsilon = k_0 L \ll 1$ for L being the characteristic size of the magnetospheric cavity in this case to yield:

$$\mathbf{v}(z,t) = \overline{\varepsilon}\overline{\mathbf{v}}_{\perp}(z,t) + \varepsilon'\mathbf{v}'_{\perp}(z,t) + \varepsilon'\mathbf{v}'_{\parallel}(z,t) \tag{1.33}$$

$$\mathbf{B}(z,t) = B_0\hat{\mathbf{z}} + \varepsilon'\mathbf{B}'_{\perp}(z,t) + \varepsilon'\mathbf{B}'_{\parallel}(z,t) \tag{1.34}$$

$$\rho(z,t) = \rho_0 + \varepsilon'\rho'(z,t) \tag{1.35}$$

The variation in these linearized variables is assumed to be along the background magnetic field. The following equations of motion for excited magnetic field fluctuations,

$$\left(\frac{\partial^2}{\partial t^2} - v_A^2\frac{\partial^2}{\partial z^2}\right)\mathbf{B}'_{\perp} = -\overline{\varepsilon}\left[\frac{B_0}{\rho_0}\frac{\partial}{\partial z}\left(\rho'\frac{\partial}{\partial t}\overline{\mathbf{v}}_{\perp}\right) + \frac{\partial^2}{\partial z\partial t}(v'_{\parallel}\overline{\mathbf{B}}_{\perp}) + B_0\frac{\partial}{\partial z}\left(v'_{\parallel}\frac{\partial}{\partial z}\overline{\mathbf{v}}_{\perp}\right)\right], \tag{1.36}$$

density fluctuations,

$$\left(\frac{\partial^2}{\partial t^2} - c_S^2\frac{\partial^2}{\partial z^2}\right)\rho' = \overline{\varepsilon}\frac{1}{2\mu_0}\frac{\partial^2}{\partial z^2}\left(\overline{\mathbf{B}}_{\perp}\cdot\mathbf{B}'_{\perp}\right) \tag{1.37}$$

and the continuity equation,

$$\frac{\partial\rho'}{\partial t} + \rho_0\frac{\partial v'_{\parallel}}{\partial z} = 0 \tag{1.38}$$

fully describe the nonlinear evolution of the interaction between the pump and excited daughter waves under the presence of small field-aligned perturbations. Equation 1.37 is particularly important because it describes the ponderomotive forces generated by the beating of the spatially co-located pump and daughter waves. In ideal MHD, the induced density fluctuations drive compressional waves, so to order ε we would expect to see the excitation of a small-amplitude compressional wave such that the background field becomes $\mathbf{B}(z,t) = B_0\hat{z} + \overline{\varepsilon}B_0'(z,t)\hat{z}$. Depending on the plasma beta and frequency of the excited daughter waves, this compressional wave will either be a fast, slow, or ion acoustic disturbance. By taking the Fourier ansatz, *Goldstein* [1978] derived the dispersion relation from Equations 1.36-1.38 resulting in

$$(\omega^2 - c_s^2k^2)(\omega^2 - v_A^2k^2)[(\omega^2 + v_A^2k^2)^2 - 4\omega_0^2] = \frac{\eta v_A^2k^2}{2}(\omega^3 + \omega^2 v_A k - 3\omega\omega_0^2 + \omega_0^2 v_A k), \quad (1.39)$$

which is fifth-order in frequency for $\eta = \overline{\varepsilon}^2|B|^2/B_0^2$. Note that analytical solutions of this dispersion require many simplifying assumptions, but inspection shows that some possible–and quite possibly, the simplest–solutions are normal modes consisting of a longitudinal and transverse wave where one possible set of solutions is $\omega = (\pm k_0 v_A, \pm k_0 c_s)$. Any solution, however, must obey the frequency and wavenumber sum rules, a statement of the conservation of energy and momentum for a resonant population of waves:

$$\omega_0 = \omega_1 + |\omega_2| \quad (1.40)$$

and

$$k_0 = k_1 - |k_2|. \quad (1.41)$$

The parametric decay process often entails backward-propagating waves, but the daughter waves have the same sense of polarization as the pump wave, which in addition to the presence of ponderomotive forces and the conservation of energy and momentum, serve as important diagnostic tools to determine if magnetospheric waves

indeed parametrically decay. And for non-circular polarization or oblique propagation, the decay process can spawn additional, higher-order wave modes–sidebands–and harmonics of the longitudinal daughter waves [*Hoshino*, 1989; *Goldstein*, 1978]. The analyses afforded by *Cramer* [1977] and *Goldstein* [1978] assume a strictly one-dimensional domain, though considering oblique propagation more closely *Yumoto and Saito* [1989] find that for any finite amplitude pump wave with no local resistivity, the onset of instability is constrained by propagation angle. For the dipolar magnetosphere, they found that the magnetoacoustic waves only became parametrically unstable with finite growth rates for propagation angles between 70 and 80 degrees of the background field. This, of course, depends on the local wave speeds where his analysis assumed a very low plasma beta characteristic of the dayside magnetospheric cavity near the plasmapause. Another type of parametric resonance involves the modulation not of the carrier or pump wave, but some characteristic parameter of the system. By using the constitutive relations for a harmonic oscillator with a time-varying parameter, such as the variation of the length of a pendulum, it is found that there exists a resonance with the natural mode of the system if the parameter varies at twice that frequency. The most natural thing to vary within an MHD plasma is the Alfvén wave speed, and indeed this theoretical analysis was performed by *Shergelashvili et al.* [2004] for fast magnetosonic waves propagating through an inhomogeneous plasma inducing Alfvén wave speed variations at twice the eigenfrequency of a standing transverse wave mode. In this way, the fast magnetosonic wave couples its energy to the shear mode with half the frequency via a nonlinear parametric resonance, which is entirely different from the FLR paradigm discussed earlier. To date, this has not been seen in observations or global magnetospheric simulations, though it seems unlikely this does not occur.

1.5 Global Magnetospheric Modeling of Ultra-Low Frequency Waves

Here we briefly review relatively recent global magnetospheric modeling efforts designed to examine ULF waves driven by internal and external excitation mechanisms, which has broad applicability to the studies undertaken in this thesis. We also briefly review the global model we use in our simulations, the Space Weather Modeling Framework (SWMF), including some of its limitations as implemented. Starting with external driving mechanisms, *Claudepierre et al.* [2010] was one of the first to use synthetic, structured solar wind conditions designed to excite broadband compressional disturbances on the dayside. By driving compressional waves into the dayside inner dipole region, he showed that the LFM (Lyon-Fedder-Mobarry) model was able to reproduce a commensurate distribution of shear wave modes consistent with the feld line resonance paradigm. To determine how fluctuations in the upstream solar wind drive variations in magnetopause displacement and the resultant excitation of compressional waves, *Hartinger et al.* [2015] used synthetic solar wind drivers with modulated dynamic pressure amplitudes and frequencies. He found that for adiabatically and rapidly varying solar wind conditions, SWMF could reproduce the excitation of fast magnetosonic waves bounded between the magnetopause and a turning point at the ionospheric inner boundary. This work essentially reproduced the results of *Claudepierre et al.* [2009] in demonstrating cavity modes. To examine of the excitation of ULF waves via internal instabilities, a number of scientists have used global magnetospheric models to excite shear-flow instabilities along the magnetopause such as the Kelvin-Helmholtz instability and associated compressive surface waves in hopes of reproducing the observation of FLRs purportedly driven by such monochromatic sources. Starting with again work by *Claudepierre et al.* [2008], using a synthetic but steady solar wind driver with negative IMF B_z and various

solar wind speeds, a linearly saturated KH instability was found to excite two surface wave populations on either side of the magnetopause in broad agreement with the theoretical findings of *Kivelson and Pu* [1984]. Naturally, the frequencies and phase speeds of the surface waves increased with increasing solar wind flow speed with very little change in wavelength. To examine the development of the KH instability and its surface wave solutions with northward IMF B_z, both *Guo et al.* [2010] and *Merkin et al.* [2013] used steady solar wind drivers with 600 km/s flow speeds and reproduced Claudepierre's findings using both a Lagrangrian code and LFM, respectively. Two major differences, however, were that Guo found the inner magnetopause surface wave was actually a slow magnetosonic wave, while Merkin found evidence of strong field-aligned currents in the magnetopause and magnetospheric body waves, likely the result of the transition of the surface waves to a spatially oscillatory mode. Certainly many other global simulations run with more sophisticated MHD or kinetic and hybrid constitutive equation sets have examined the excitation of ULF waves, but this small subset represent the state-of-the-art ideal MHD studies of the FLRs, surface waves, and magnetotail modes we reproduce in the Space Weather Modeling Framework (SWMF), with some important differences as we will discuss. However, while the limitations of ideal MHD are well-known, including a lack of local dissipation, self-consistent–Landau damping–or otherwise, explicit resistivity and the use of only the ion species, magnetospheric dynamics include a number of phenomenological constructs such as the plasmasphere, ring current, polar wind outflow, and presence of multiple ion species that are not included in either of our studies. SWMF supports all of these physics and parameter-based models, and any of them may have significantly impacted our results. The point therein, however, is that while actual magnetospheric dynamics may differ substantially from the results of our model, the results are *self-consistent*, converged solutions of these numerical experiments.

1.5.1 Global Model

Since all the results in this dissertation are derived from a numerical model, we devote this section to exploring its various features, uses in scientific studies, and limitations.

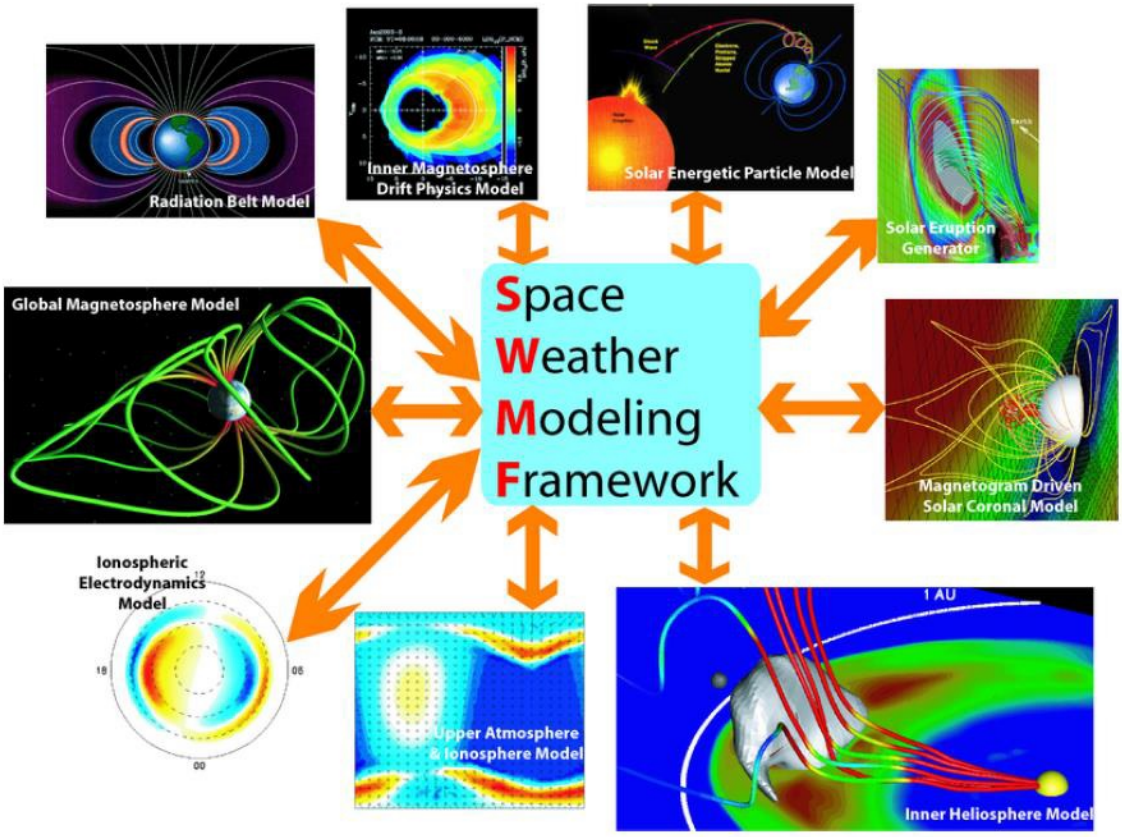

Figure 1.4: Graphical illustration of the different components of the Space Weather Modeling Framework (SWMF). We use the Global Magnetospheric and Ionospheric Electrodynamics Models exclusively.

Knowledge of the general capabilities and structure of SWMF derives from *Toth et al.* [2005] and the SWMF manual. Solving the MHD constitutive equations within the boundary conditions specified in the Global Magnetospheric (GM) model within SWMF falls to BATS-R-US, the Block-Adaptive-Tree-Solarwind-Roe-Upwind-Scheme. By 'block-adaptive-tree,' this code uses a computational grid with an adaptive, Cartesian stencil designed to provide sufficient grid resolution where needed

while efficiently solving the discretized hyperbolic, compressive MHD equations using the 2nd-order difference–upwind–scheme. Using outer boundaries with an implanted magnetic dipole with the characteristics of Earth's magnetosphere, BATS-R-US generates solutions at each grid point at a specific or implicit time step for the 3D MHD state variables for the magnetic and velocity fields and density. The upstream boundary is given time-dependent boundary conditions consistent with a solar wind driver consisting of magnetic and velocity field inputs along with density and temperature. BATS-R-US can solve the non-ideal MHD equations with multiple species with higher order solvers as well and can use with user specification numerous classes of numerical solvers like the Roe, Linde, and Rusanov schemes, which have various diffusivity, stability, shock-capturing profiles, and pressure and density positivity abilities therein. GM has the capability to employ a spherical grid too with various user specified outer boundary conditions, time steps, grid resolutions including adaptive mesh refinement, and physics parameters. To ensure the wave speeds are finite to keep the time steps reasonable, Boris corrections can be employed. Since the MHD equations are a set of coupled, multi-dimensional equations solved in a computational domain comprised of (usually) millions of grid cells, SWMF is optimized for massively-parallel core computer architectures by using a Message Passing Interface (MPI). SWMF and all of its core routines are based in Fortran 90.

The real strength, however, is the modularity of its physics and parameter-based packages that are two-way coupled to the basic numerical solver routines in BATS-R-US. Seen in Figure 1.4, these include radiation belt and plasmasphere along with inner ring current and polar wind outflow modules. Two-way coupling involves the message passing between the GM/BATS-R-US code and each module at a prescribed time cadence so that solutions within both domains are updated and interpolated locally. We used the two-way coupled Ridley ionospheric electrodynamics solver to solve the ionospheric conductance distribution at Earth where along an inner boundary, usually

at 2.5 R_E, field-aligned current solutions generated by GM/BATS-R-US are mapped to the ionospheric solver, which updates the local values of the ionospheric conductance, which subsequently changes the field-aligned currents at the inner boundary [*Ridley et al.*, 2000]. In this way, the inclusion of this particular model helps to self-consistently emulate the impact of a resistive, ionospheric inner boundary on global, magnetospheric dynamics. This module has multiple user specific commands to set the ionosphere conductance as uniform or reactive to simulated, parameterized electron precipation. We use only GM/BATS-R-US and the Ridley ionospheric module with a synthetic upstream solar wind profile.

The grid resolution–normalized to the number of grid cells along a 1 R_E line segment–is one of the most important user inputs in BATS-R-US because it determines whether the numerical solution converges and remains bounded, and whether shocks, like at the bow shock, are captured correctly with minimal diffusion. What this means is magnetospheric solutions can change dramatically with relatively small changes in not only the grid resolution but the grid resolution within particular regions of the magnetosphere. While MHD solutions are self-similar, the grid resolution needs to be set at a level corresponding to the smallest predicted dynamical length scale over the course of a simulation. Within the context of ULF waves, this is easy as it's simply a multiple of the Alfvén wave speed in the region of interest divided by the highest expected frequency. However, the field-aligned structure within dipole magnetic topologies 'breaks the symmetry' of self-similarity by providing a preferred reference frame for the dynamics and propagation of ULF waves and magnetospheric convection, which is the essential challenge in choosing the appropriate grid resolution for numerical convergence within global MHD models. Resolving field lines becomes very important especially for standing Alfvén waves, but it is difficult within uniform Cartesian geometries because the density of field lines increases with the cube of the radius on approach to the inner boundary. Choosing the 'right' grid resolution often

requires unmitigated trial and error balancing the demands of numerical convergence against computational costs.

1.6 Outline of Thesis

The main objectives of this thesis were to explore the excitation and propagation of ULF waves using global magnetospheric simulations, but the main outcomes were the observations in the simulation data of local time asymmetries in FLR amplitudes and the excitation of magnetotail kink modes via the decay of magnetopause surface waves. Internal and external excitation mechanisms underlie these resonant linear and nonlinear wave-wave interactions. As such, the dissertation is structured to reflect a progression from first-order resonant interactions to the observations of higher-order wave-wave couplings on the dayside and nightside of the magnetosphere. The list of questions we addressed in this study were: 1) Can SWMF reproduce and sustain wave-wave coupling; 2) What is the coupling mechanism between the observed magnetopause surface and magnetotail waves; and 3) What are the eigenmodes of the magnetotail waves? The answers to the last two questions as an outcome of this work comprise original contributions to the study of wave-wave coupling and propagation in the magnetosphere. We were motivated to examine wave-wave coupling mechanisms to determine how a significant amount of electromagnetic energy could propagate into the magnetotail and where these waves could impact magnetotail dynamics.

In Chapter 2, we explore local time asymmetries in and the reproduction of FLRs in SWMF driven by broadband dynamic pressure fluctuations in the upstream solar wind. While the reproduction of the FLRs was principally a numerical exercise, we found using spectral analyses that in the absence of any intrinsic asymmetries that the FLR amplitudes were different in the postnoon/prenoon sectors of the dayside cavity with a few surprises. We found that this was not reected entirely in a corresponding asymmetry in the strength of the compressional driver as there were signicant

dawn-to-dusk asymmetries in the equatorial mass density. This observation seemed consistent with local time asymmetries in ionospheric dissipation, but the effect of spatially co-located, shear wave modes with broadband frequencies with associated harmonics on the equatorial mass density distribution was left unanswered with the hypothesis that higher-order, nonlinear forces such as the ponderomotive force could mediate the equilibrium. In Chapter 3, we found that predominately transverse magnetopause surface waves not excited by a shear-flow instability coupled to kink waves propagating across the magnetotail. By ruling our linear resonance paradigms, we found that ponderomotive forces mediated the excitation via a parametric decay instability of slow magnetosonic waves and these kink mode waves. We found that the propagation characteristics of these magnetotail kink mode waves became nonlinear as demonstrated by wave steepening, density holes, and large enhancements of field-aligned currents. We conclude in chapter 4 by pointing out several difficulties straining the interpretation of our findings and its applicability to experimental observations due to the limitations of ideal MHD in accurately modeling the self-consistent dissipation of many of these wave modes. We also propose future numerical studies that might reconcile these issues while also grounding this work within a solid theoretical framework.

CHAPTER II

Field Line Resonances and Local Time Asymmetries

Abstract We present evidence of resonant wave-wave coupling via toroidal field line resonance (FLR) signatures in the Space Weather Modeling Framework's (SWMF) global, terrestrial magnetospheric model in one simulation driven by a synthetic upstream solar wind with embedded broadband dynamic pressure fluctuations. Using *in situ*, stationary point measurements of the radial electric field along the 1500 LT meridian, we show that SWMF reproduces a multi-harmonic, continuous distribution of FLRs exemplified by 180° phase reversals and amplitude peaks across the resonant L shells. By linearly increasing the amplitude of the dynamic pressure fluctuations in time, we observe a commensurate increase in the amplitude of the radial electric and azimuthal magnetic field fluctuations, which is consistent with the solar wind driver being the dominant source of the fast mode energy. While we find no discernible local time changes in the FLR frequencies despite large-scale, monotonic variations in the dayside equatorial mass density, in selectively sampling resonant points and examining spectral resonance widths, we observe significant radial, harmonic, and time dependent local time asymmetries in the radial electric field amplitudes. A weak but persistent local time asymmetry exists in measures of the estimated coupling efficiency between the fast mode and toroidal wave fields, which exhibits a radial dependence

consistent with the coupling strength examined by Mann et al. [1999] and Zhu and Kivelson [1988]. We discuss internal structural mechanisms and additional external energy sources that may account for these asymmetries as we find that local time variations in the strength of the compressional driver are not the predominant source of the FLR amplitude asymmetries. These include resonant mode coupling of observed Kelvin-Helmholtz (KH) surface wave generated Pc5 band ultra-low frequency (ULF) pulsations, local time differences in local ionospheric damping rates, and variations in azimuthal mode number, which may impact the partitioning of spectral energy between the toroidal and poloidal wave modes.

2.1 Introduction

In the collisionless, inhomogeneous plasmas typical of the terrestrial magnetosphere, global ULF waves are an important energy transport modality. With fundamental wavelengths on the order of the magnetospheric cavity, ULF waves in the Pc3-5 category with frequencies between 2 and 100 mHz are known to mediate the long-range relaxation of internally driven kinetic instabilities [*Cheng et al.*, 1994] and externally driven compressional disturbances generated in the interaction of the solar wind with the magnetosphere. There are numerous sources of these waves. Examples include drift-mirror type instabilities borne from plasma temperature anisotropy– a potential source for the energization of the radiation belt electrons [*Hasegawa*, 1969;*Elkington et al.*, 1999]; the Kelvin-Helmholtz instability, which arises due to the buffeting of the magnetopause to high-speed solar wind events; resonantly excited surface waves along the magnetopause [*Mann et al.*, 1999]; and dynamic pressure fluctuations in the upstream solar wind [*Takahashi et al.*, 1988], which is the focus of this chapter.

A field line resonance is a particular coupling phenomenon between global, fast magnetosonic and localized shear Alfvén waves and have long been used to explain

the latitudinally-dependent wave amplitude and frequency spectra observed by satellites and ground-based magnetometers [*Engebretson*, 1987]. Broadband excitations at the magnetopause are a well-known source of these waves, and many have explored a variety of paradigms to reconcile observations of field line resonances with the ongoing development of the theory [*Kivelson et al.*, 1986; *Samson et al.*, 1992]. Kivelson et al. [1986] modeled the closed dipole field with a box geometry with perfectly conducting magnetopause and ionospheric boundaries using ideal magnetohydrodynamics (MHD), where FLRs appeared as singularities in the coupled wave equations. Observational evidence of FLRs at discrete frequencies in the nightside have led Samson et al. [1992] to invoke a waveguide model to explore the propagation of wave modes between the magnetopause and turning points at the inner boundary of the magnetospheric cavity.

The field-line curvature, density distribution and gradients significantly impact the spectra, nodal and harmonic structure of these wave modes [*Radoski et al.*, 1966; *Mann et al.*, 1995]. The finite conductivity of the magnetospheric boundaries, wave-particle interactions on kinetic scales, and the generation of parallel electric fields can all dampen shear Alfvén waves through field aligned currents that close in the ionosphere, dissipate through Joule heating, and wave mode decay and phase mixing [*Newton et al.*, 1978; *Mann et al.*, 1995; *Sarris et al.*, 2009]. The amplitude peak at the resonant L shell balances the compressional energy with these loss mechanisms, and the resonance condition entails a radial 180 phase reversal across the singular point [*Kivelson et al.*, 1986].

Numerous studies have observed and examined a significant local time asymmetry in the occurrence rate and amplitude of field line resonances driven by Pc5 pulsations [*Nosé et al.*, 1995; *Chisham et al.*, 1997; *Mann et al.*, 1999; *Glassmeier et al.*, 2000]. Mann et al. [1999] for instance find evidence that the more pronounced occurrence and amplitude in the dawn quadrant is due to the coupling of magnetopause shear-

flow instabilities to the magnetospheric cavity and over-reflection of waveguide modes generated by solar wind dynamic pressure. Satellite observations bear out this hypothesis. Concerning measures of the coupling efficiency between the compressional driver and standing wave modes, Mann et al. [1999] and Zhu and Kivelson [1988] show using numerical models an azimuthal mode number and radial dependence by integrating the total, time-dependent Alfvénic energy across the domain assuming a single frequency driver. Measuring the coupling rate is important because it gives the amount of energy made available by the resonant coupling, the mechanism therein, and how numerical or local plasma conditions may impact the mode coupling process. We note that no global magnetospheric model has been used to explore local time asymmetries in FLR amplitudes nor the coupling rate, despite the need to quantify and examine the mechanisms impacting the partioning of energy in wave mode conversion.

Analyzing resonant coupling mechanisms and quantifying wave coupling strengths in global magnetospheric models may be relevant to radiation belt studies. ULF waves are a well-known energization source of electrons through either radial diffusion from a noon-midnight asymmetric toroidal electric field or drift or bounce resonance with poloidal electric fields [*Hasegawa*, 1969;*Elkington et al.*, 1999]. The former would be a more likely explanation for the low azimuthal wave modes generated in this simulation, and FLRs would naturally be the only source of the toroidal wave fields.

Numerical modeling has been used to examine field line resonances, particularly the sources of the compressional energy, wave mode coupling mechanisms, and related phenomenona within various geometries. Degeling et al. [2010], for instance, used a linear MHD model of the magnetosphere to study the effect of compressed dipole fields on the spatiotemporal sources and generation mechanisms of fast mode and coupled shear Alfvén waves. The global magnetosphere, however, presents notable challenges to these models, even where non-linear processes are included. Claudepierre et al.

[2010] were the first to show in the self-consistent, global MHD Lyon-Fedder-Mobarry model (LFM) that fluctuations in the upstream dynamic pressure can produce FLRs in the dayside magnetosphere and to show that they were driven by cavity modes. Even then, others argue that the discretization of Cartesian grids, such as in the SWMF model, and the Alfvén continuum dampen and obscure what is otherwise a localized resonance phenomena, which make them difficult to detect, particularly with broadband sources, or difficult to produce altogether [*Stellmacher et al.*, 1997]. Bellan [1996], for instance, showed that kinetic Alfvén waves mediate the coupling between fast and shear modes, which may suggest FLRs in MHD models are an unphysical, numerical artifact. This is particularly evident in cases where the grid resolution is much larger than the phase mixing length as the numerical solution may never converge. Additionally, the treatment of the ionosphere in global magnetospheric models is non-trivial as the ionosphere also plays a major role in the formation, structure, and dissipation of FLRs.

These outstanding issues compel us to test whether global magnetospheric models can reproduce field line resonances in a manner consistent with theory, though we note that very few if any have been validated systematically using observational data. The notable differences between global magnetospheric and ionospheric models allow us to explore a variety of mechanisms that impact the excitation and structure of field line resonances and to make improvements that may better reproduce FLRs and related wave-wave phenomena. The goal of this technical study is to show that the global magnetospheric model, SWMF, can produce FLRs–and generally speaking, the coupling of wave modes–using the solar wind as the compressional driver and to show that it can reproduce the local time asymmetries captured by numerous observation studies. Additionally, the linearly increasing amplitude of the dynamic pressure fluctuations used here often resembles the dynamic solar wind density profiles seen during periods of heightened geomagnetic activity, which allows us to observe

the impact on FLRs and identify Alfvén-wave driven phenomena. The study broadly follows the design employed by Claudepierre et al. [2010], who used the LFM global MHD model.

2.2 Methodology and Simulation Results

2.2.1 Global Model

We use the SWMF global MHD model coupled with a self-consistent ionospheric electric potential solver with an inner boundary placed at 2.5 R_E [*Toth et al.*, 2005]. We set the inner boundary number density to 28 particles per cm^{-3} so that the fundamental and several harmonics of the field line eigenfrequencies would lie within the spectral bandwith of this simulation. The ionospheric conductance is set with an EUV solar flux of $100{\times}10^{-22}$ J/m^2 and a 0.25 Siemen auroral oval Pedersen conductance. While the conductance within the auroral oval is much smaller than what other authors have used in numerical simulations, since the ionospheric conductance is regulated mostly by the EUV solar flux, the conductance values elsewhere are typical. SWMF uses a Cartesian grid and solves the single-fluid, ideal MHD equations using a non-conservative, second-order upwind scheme with a 0.125 R_E grid resolution throughout the dayside magnetospheric cavity. The solar wind and IMF serve as upstream boundary conditions at 32 R_E with open boundary conditions at 92 Re in the tail and +/- 92 R_E in the y and z-directions. A Boris correction to five percent the speed of light ensures a reasonable time step, and a partially implicit time-stepping scheme with a minimum time step of 5 seconds is used for stability. In this simulation, SWMF is not coupled to a plasmasphere or ring current model, which may underestimate the time-dependent ion density and pressure distribution in the inner magnetosphere. The magnetic axis is aligned with the rotational axis.

Shown in Figure 2.1, the upstream solar wind density profile includes broadband

fluctuations between 0 and 100 mHz with a spectral resolution of 0.03 mHz. This spectral bandwidth matches the time cadence of the numerical solver. There are two major differences between the simulation setup here and the ones employed by Claudepierre et al. [2010] aside from the ionospheric conductance: the inclusion of a linearly increasing in time fluctuations in the amplitude of the dynamic pressure to within a maximum envelope of 0 to 10 particles per cm^{-3} with a root mean average of 5; and a rotating dipole, which allows us to examine self-consistent diurnal impacts on ionospheric conductance and density distribution. We designed the driver as such as a trace to identify the solar wind driver as the driver of the FLRs, and indeed the amplitude of the FLRs grows continuously–albeit at different rates–with the amplitude of the pressure fluctuations and to see if we can drive ULF wave-mediated phenomena. We employ an average, quiet time solar wind velocity of 400 km/s and iniatilize SWMF in a steady-state mode for 5000 seconds in order to eliminate transient, global magnetospheric disturbances. We note that this may not have been sufficient to allow the magnetosphere to relax into a global equilibrium state. A northward B_z of 5 nT is maintained throughout the simulation run.

To examine the toroidal wave modes, we analyze the radial electric field component, E_r, in the equatorial plane at the 1500 LT meridian. We use stationary points located at 0.125 R_E increments from 3 to 11.875 R_E to sample the electric field at a 10 s cadence for 2 hours after the onset of the upstream pressure fluctuations, which together afford an approximately 0.1 mHz spectral resolution up to a Nyquist frequency of 50 mHz. We observe a similar attenuation of the high frequency–greater than 20 mHz–components of the broadband upstream density fluctuations as reported in Claudepierre et al. [2010]. We believe, however, that this is due to the 0.125 R_E grid resolution upstream of the bow shock. Given the Alfvén wave speeds of 50 km/s, the wavelengths of the frequency components greater than 20 mHz are about the width of 3 grid cells, which is much less than what is necessary to fully resolve

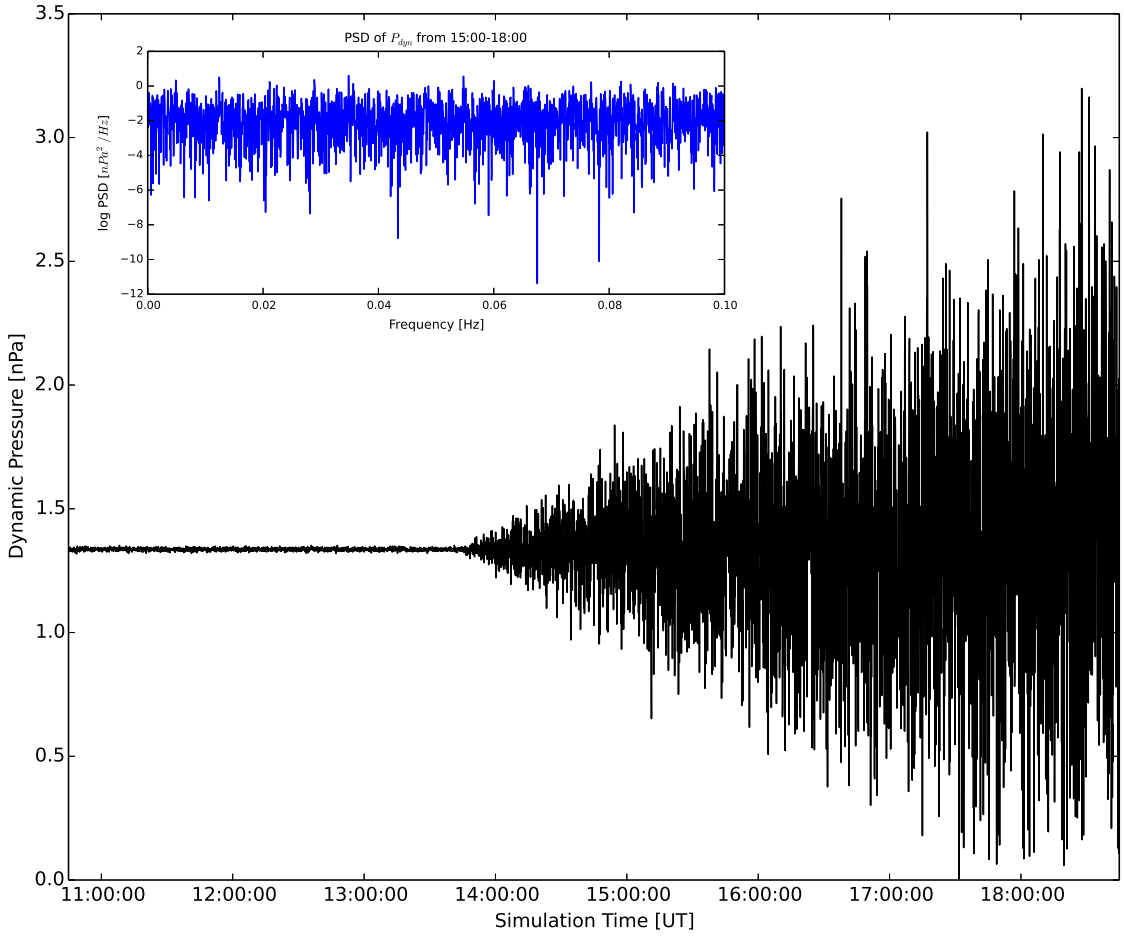

Figure 2.1: Solar wind dynamic pressure as a function of simulation time with an embedded power spectral density plotted in log scale showing a uniform distribution of frequencies between 0 and 100 mHz. The dynamic p_{dyn} fluctuations increase linearly in amplitude starting three hours into the simulation. The fluctuations at the end of the simulation are approximately 100 percent of the mean and span 3 nPa peak-to-peak.

those waves. Simulation runs with grid resolutions of about 1 R_E at the upstream boundary show a similar degree of attenuation above 10 mHz, which corrobates this interpretation.

We calculate the field line eigenfrequencies using a linear approximation using Chi et al.'s [1998] calculations of the integral of the Alfvén wave speed along a dipolar field line given by

$$\tau = 1.9\times10^{-5} {n_0}^{1/2} L^4 \int_{\theta_S}^{\theta_N} \cos^{7-p}\theta \, \mathrm{d}\theta \tag{2.1}$$

which we solve numerically. The bounds of integration are between the north and south ionospheric footpoints of the field line for a given L shell, where n_0 is the plasma density at the equatorial crossing. The p value is the density power law scaling, which we calculate directly in our simulation from the radial profile of the ion density at the 1500 LT meridian. Since the Alfvén wave speed decreases linearly through the time period chosen for analysis, we take the average power law dependence of p=1.41. While Radoski et al. [1966] solved the toroidal wave equation exactly using a p=6 density law, the wave equation cannot be solved analytically for p=1.41, so we use the WKB approximation exclusively. Additionally, since noon meridional cuts show an axisymmetric density distribution, a power law fit of the radial density distribution in the equatorial plane is appropriate for the WKB approximation of the field-line eigenfrequencies.

The coupling between the global magnetospheric and ionospheric electric potential solver required careful consideration. Even though we allow the magnetic field lines to move at the inner boundary, we consider this boundary to be closed since the solver requires the electric and magnetic field perturbations to vanish in the region between the ionosphere and inner boundary. Since only the field aligned currents along the background, dipole field are mapped to and from the ionosphere, the inner boundary behaves as a node. Even if the gap region were included in the calculation of the

eigenfrequencies, the contribution would decrease the eigenfrequencies by at most ten percent. However, this is well within the envelope of the observed spectral resonance widths of the radial electric field.

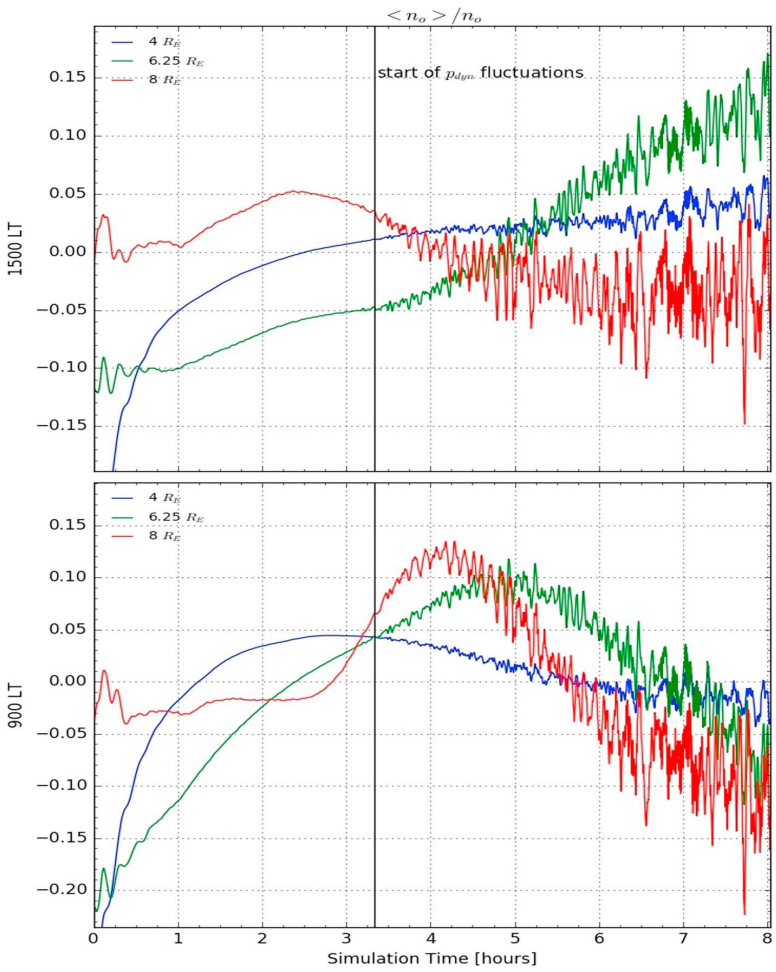

Figure 2.2: Number density profiles taken along the 1500 and 900 LTs at various radii. Note the small, modulated time-dependent variation.

The time-dependent number density profile along the 1500 and 900 LT meridians is shown in Figure 2.2. We note that the increasing amplitude of the upstream pressure fluctuations is associated with a corresponding decrease in the Alfvén wave speed profile in the inner magnetosphere such that by the end of the simulation run, there is up to a 10 percent fractional change in the Alfvén wave speed and 20 percent change across the noon meridian. While the field line eigenfrequencies are non-stationary,

the radial change in eigenfrequency over a grid cell is slightly more than the fractional change due to the increasing Alfvén wave speed, which means the change in the Alfvén wave speed ultimately has no significant impact on our resonance signatures.

2.2.2 Field Line Resonance Signatures

Figure 2.3 shows the radial power spectral density of the radial electric field component along the 1500 LT meridian with an overlay of the WKB eigenfrequencies for the odd harmonics, which following Lee et al. [1989] are the only harmonics supported with the driver we have prescribed. The profile extends from just outside the inner boundary at 3 R_E to just beyond the magnetopause–centered around 11 R_E as indicated by the single vertical line–at 11.875 R_E. Figure 2.4 shows the dynamic cross phase for an identical profile. We calculate the phase of the radial electric field between adjacent radial positions separated by one R_E such that the phase plotted at each radii is the cross phase of the electric field with a radial position one R_E upstream. We use the same two hour time interval to calculate the FFT for each radial position. This is justified because the FLRs are continuously driven and the fractional change in the Alfvén wave speed is inconsequential as discussed above, so the phase changes are appropriately stationary. The alternating bands of 90 to -90 degree phases signify the phase reversals typical of a field line resonance signature for low azimuthal wave number drivers [*Feinrich et al.*, 1997].

2.2.3 Signatures of Asymmetries in FLR Amplitudes

To observe local time asymmetries in the FLR amplitudes, we calculate the sum of the short-time spectral energies of the radial electric field and compressional magnetic field ratios at [1320,1080], [1440,920], [1500,900], 1520,840], and [1600,800] LTs from the postnoon to prenoon quadrants from one hour long intervals at 10 second sliding increments. We choose a frequency band from 0.5 to 45 mHz and plot the average of

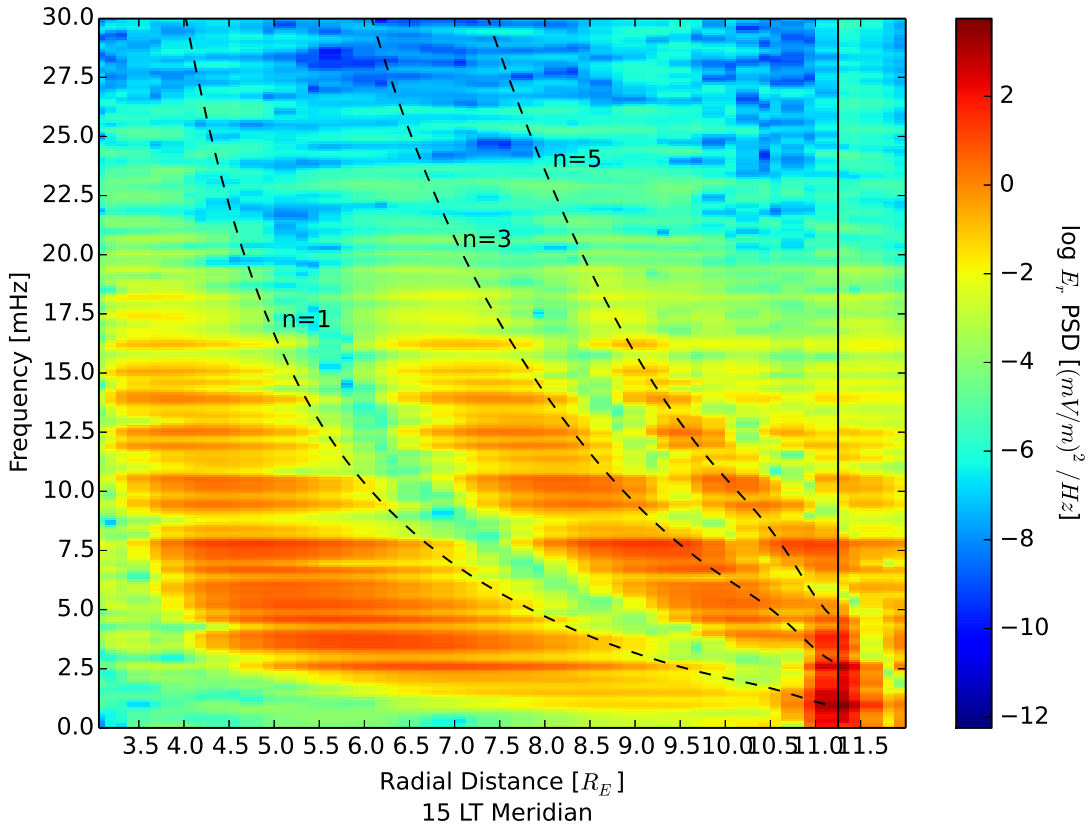

Figure 2.3: The radial power spectral density along the 1500 LT meridian shows at least three well-defined harmonics as indicated by the WKB estimated eigenfrequencies. Note the radial resonance widths, determined primarily by the ionospheric Pedersen conductance.

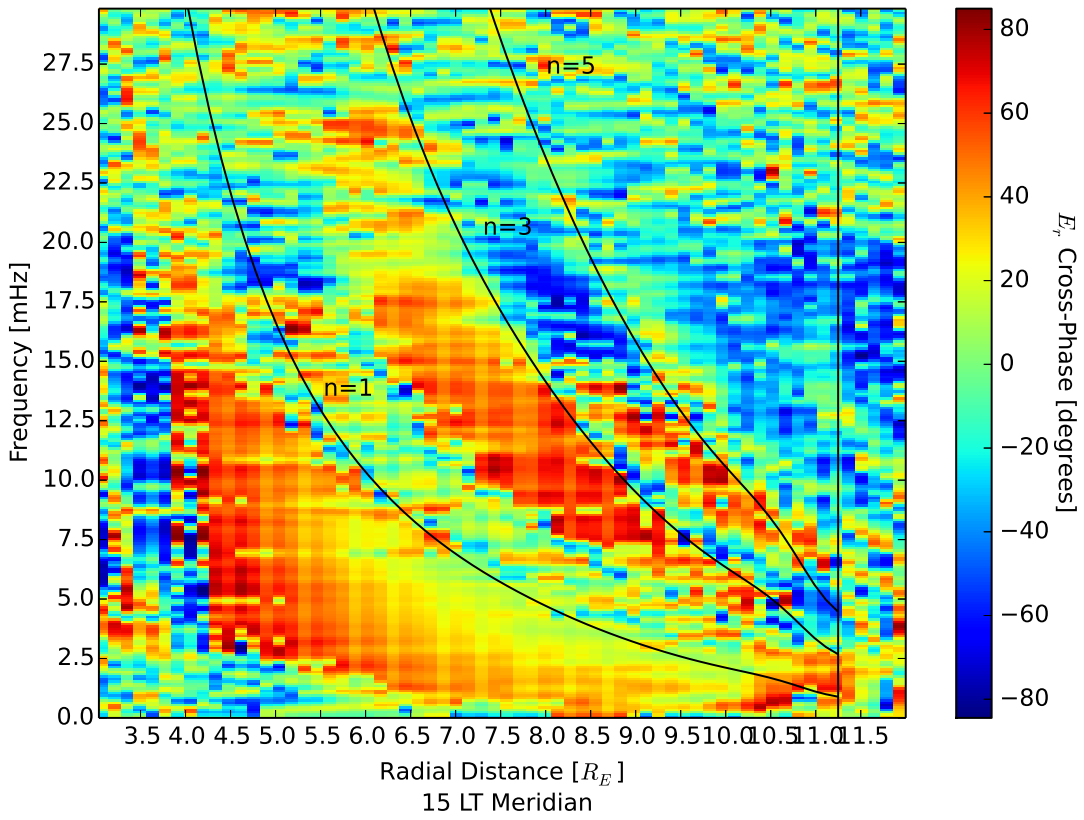

Figure 2.4: The radial cross-phase along the 1500 LT with WKB estimated eigenfrequencies. The phase reversals show the location of the FLR, except for the region closest to the inner boundary, which may be the location of the turning point.

every time-window at each radii from 3 to 10.5 R_E every 0.125 R_E as seen in Figure 2.5 (a). This method calculates the spectral energy across each harmonic spectral resonance width, which is the sum of the overlap of the spatial resonance widths of adjacent resonant L shells.

For finite bandwidths the spectral resonance width is simply the Fourier transform of the radial fluid displacements [Mann et al., 1999], so the approach is justified here. We find a persistent bias in the strength of the FLRs in the prenoon quadrant Earthward of L=7 of at least 10 percent with a general increase in the strength of FLRs in the postnoon quadrant moving towards the magnetopause. We also plot in Figure 2.6 (a) the radial electric field ratios as a function of time at the 900 and 1500 LT for the fundamental and third harmonics at L=6 and L=8. Two patterns seem robust in Figure 2.6: the third harmonic has more energy at L=8 in the postnoon quadrant while the fundamental has more energy at L=6 in the prenoon quadrant, which increases in time. By comparing the radial local time asymmetry between the compressional and radial electric fields, we observe that the compressional field does not seem to be the predominant source controlling the asymmetry in FLR amplitudes.

To estimate the coupling efficiency between the compressional driver to the FLRs, we use a similar procedure outlined above to quantify the local time asymmetry in the electric fields but instead take the ratio of the radial electric field to B_z. Since the difference in fast mode energy across a resonant shell should approximately equal the shear Alfvén energy, we can write $E_{F_0} - E_{F_1} = E_A$, where F_0 is the fast mode energy upstream of the resonant L shell and F_1 is downstream. Noting that the dominate–and readily distinguishable–signatures of the compressional and standing wave modes are B_z and E_r, respectively, ignoring fluid velocities and using Faraday's law we find that $1 - \left(\frac{B_{z1}}{B_{z0}}\right)^2 \approx \frac{1}{\omega_r^2 (z_0 - z_1)^2} \left(\frac{E_r}{B_{z0}}\right)^2$, where ω_r is the resonant frequency at the L shell and $z_0 - z_1$ is the distance along the field line. In ideal MHD the coupling of the wave fields to the fluid displacements should be lossless, thus by evoking the virial theorem,

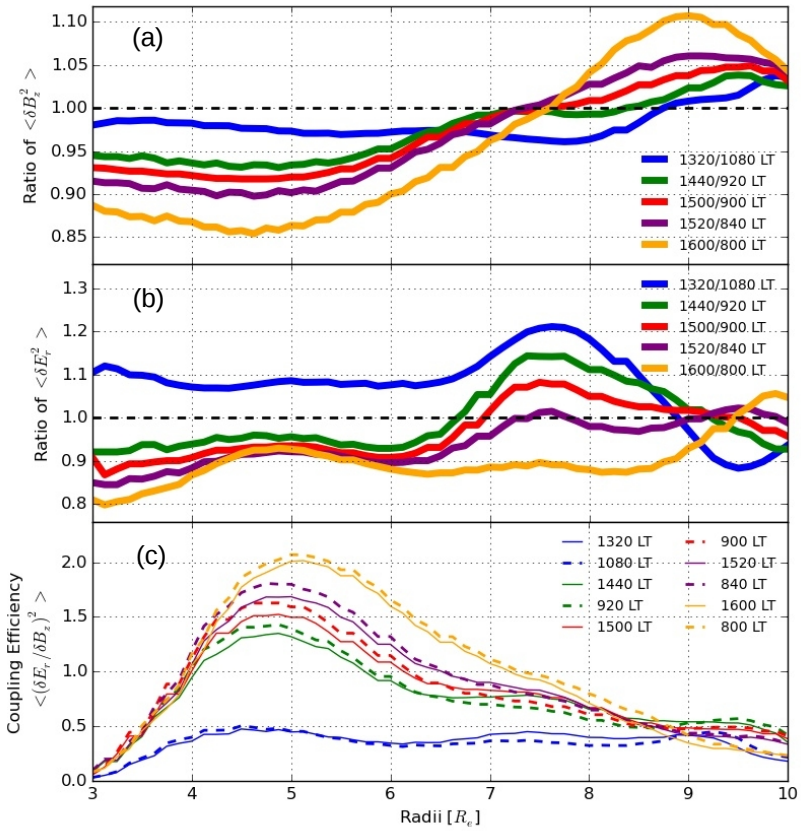

Figure 2.5: a) Ratio of the time-averaged spectral energy in the compressive B_z fields in the postnoon and prenoon sectors along radial cuts from the inner boundary through to the magnetopause spanning from 800 to 1600 LT. Regions of the curves above 1 indicate that more energy in the postnoon sector, and vice versa. b) Same as (a) but for the radial electric fields, E_r. c) Coupling efficiency as measured by the ratio of the time-averaged spectral energy of the radial electric and compressional magnetic fields. Note the marginal local time asymmetry and general increase in efficiency moving outward from the noon meridian.

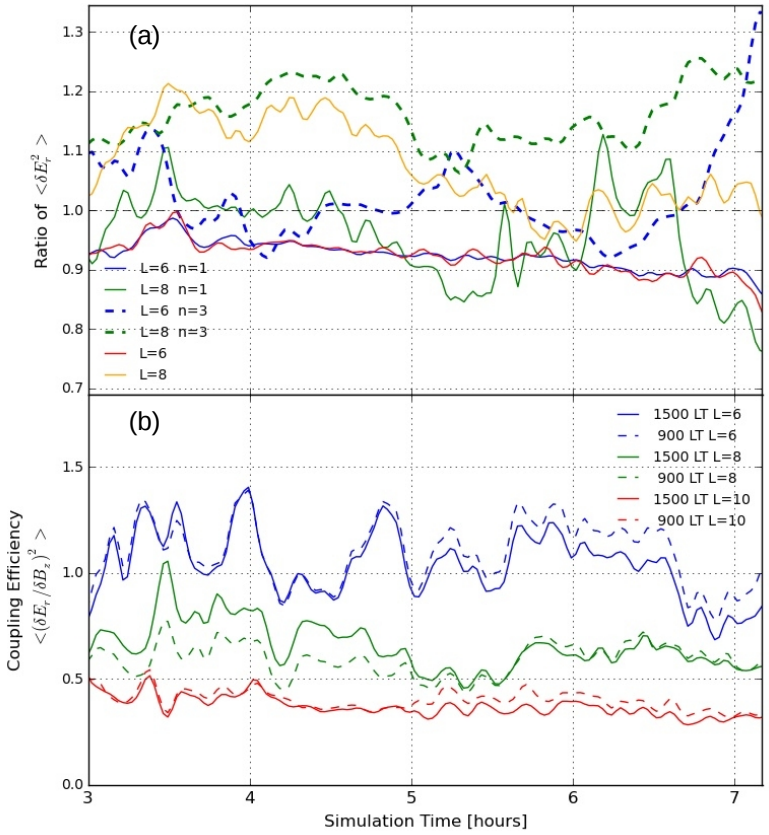

Figure 2.6: a) Time-averaged spectral energy of the radial electric field post-noon/prenoon ratios at L=6 and L=8 for the first and third harmonics and across the entire spectral range as a function of simulation time. Each spectral component shows distinct time-dependent behavior. b) Coupling efficiency as a function of simulation time comparing the 1500 and 900 LT meridians at L=6, 8 and 10. The time variation is bounded with marginal post/prenoon asymmetry. Note that the coupling efficiency decreases moving sunward.

we can justify ignoring the fluid velocities by integrating the fields over time, which should be a good approximation of the wave energy. We plot in Figure 2.5 (c) the time-averaged estimated coupling efficiency, which we justify averaging after observing a minimal time-variation in coupling efficiency at each radii. We note that the units of this measure of coupling efficiency is in units of velocity, which suggests that the spectral energy in the azimuthal drift balances the resonant coupling of the driver to the standing Alfvén waves. We note a small but persistent local time asymmetry in the coupling efficiency with a bias towards the prenoon quadrant Earthward of L=6 or L=7 and an increase in the efficiency moving from near the noon to the dawk-dusk terminators. This plot, Figure 2.6 (b), agrees qualitatively with the coupling strengths derived and calculated by Zhu et al. [1988] and Mann et al. [1999].

Dayside equatorial maps of the time-averaged spectral energy of E_r within 5 mHz bands spanning 5-10, 10-15, and 15-20 mHz from the fourth to sixth simulation hours is plotted in Figure 2.7. These maps include side plots of the radial electric field along meridional and radial rays that cut through the FLR envelopes and highlight the frequency-dependent local time asymmetries in FLR amplitudes shown in Figures 2.5 and 2.6.

2.3 Discussion

2.3.1 Demonstration of FLRs

Unambiguous evidence of a field line resonance requires a 180 degree phase reversal across an amplitude peak at the resonant L shell. Using stationary point measurements of E_r along the 1500 LT meridian provides convincing evidence in Figures 2.3 and 2.4 of a multi-harmonic–1st, 3rd, 5th, continuous FLR spectrum.

Given the linearly increasing fluctuations in the amplitude of the dynamic pressure in the upstream solar wind driver, we must carefully interpret our FLR signatures

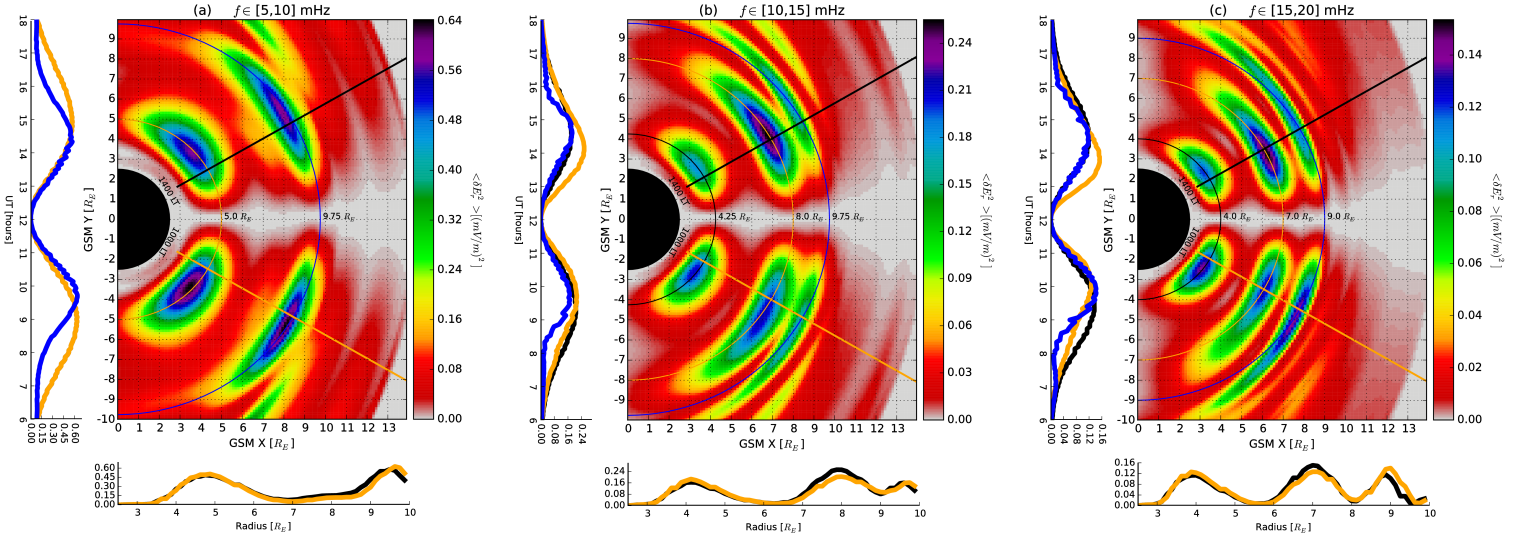

Figure 2.7: a),b), and c) show time-averaged dayside equatorial wave energy maps of the radial electric field with side plots capturing the radial and local time variation therein at color-coded locations for the [5,10],[10,15], and [15,20] mHz spectral bands. These maps illustrate the global structure of the shear eigenmodes. The pre/postnoon asymmetries are clearly identifiable.

within the context of the theory developed within the framework of impulsively or steadily-driven FLRs. In particular, the amplitude of the FLRs is an equilibrium at each point in time between the driving energy and ionospheric damping, which should be appreciable at large L shells here. The saturation widths depend additionally on the phase mixing length, coupling rate, and azimuthal mode number. Feinrich et al. [1997] concluded that the resonance widths for the amplitude and phase change across an FLR should be broad and narrow, respectively [Mann et al., 1995]. However, for drivers with slowly increasing amplitude, the FLR equilibrium amplitude would never approach its asymptotic phase mixing length because the FLR would not decay, and we would expect broad resonance widths, which is consistent with our data. And if the coupling rate were slower than the rate of increase in the amplitude of the fluctuations, the FLR would never reach equilibrium nor saturate. While a quantitative analysis of the actual coupling rate is beyond the scope of this paper, the FLR saturation widths at different time intervals in the simulation are the same, which suggests a constant coupling rate that is faster than the rate of increase in the amplitude of the fluctuations in the driver. The nearly constant coupling efficiency at each radii seen in Figure 2.6 (b) corrobates this interpretation. Since a qualitative comparison with the radial PSD of E_r from Claudepierre et al. [2010] shows a general agreement even if the mechanisms controlling for their saturation widths are different, this suggests our results with this particular driver are not extraordinary and are consistent with being FLR signatures.

Another issue is whether the grid resolution for this simulation is large enough for SWMF to converge to a physical solution. This is an important consideration because for a given density distribution and ionospheric conductance the asymptotic phase mixing length may conceivably approach the ion gyroradius or smaller, wherein an MHD solution breaks down and a two-fluid or kinetic treatment would become necessary [*Mann et al.*, 1995]. Fortunately, the phase mixing length for the density

distribution we have prescribed in this simulation is much larger than a grid cell for the entirety of the magnetospheric cavity. Since the wave amplitude of the driver increases continuously in time, the decay times should be appropriately small, and we can conclude that the phase mixing length is always strictly greater than a grid cell and that the grid resolution is sufficient to resolve FLRs in this simulation.

We observe that the WKB approximation of the field line eigenfrequencies does not accurately align with the first and third harmonics in the radial PSD, but this result is not surprising for a number of reasons. As noted earlier, the eigenfrequencies in this simulation are non-stationary since the Alfvén wave speed linearly decreases through the simulation run time. This is due to an enhancement in the plasma density in the postnoon quadrant with a corresponding density depletion in the prenoon quadrant–a typical signature of a diurnal local time asymmetry [Berube et al., 2003]. Another reason is the WKB approximation is only a first-order solution to the wave equation and does not take into account the more involved wave coupling dynamics that may influence the field line eigenfrequency and saturation widths, such as nonlinear feedback from ponderomotive forces. The WKB approximation, however proves to be a better estimate for the higher order–fifth–harmonics.

2.3.2 Potential Sources of Asymmetry

The short-time, spatiotemporal spectral energy ratios of the radial electric field show a notable local time, harmonic, and radial asymmetry that's selectively time-dependent. While observational studies have shown before more pronounced meridional asymmetries with a bias in amplitudes towards the prenoon quadrant, its harmonic and radial dependence is an unexpected result here. Here we suggest some plausible mechanisms for particular asymmetries we observe in Figures 2.5 and 2.6.

Kelvin-Helmholtz surface waves have loomed larged in studies of dawn-dusk asymmetries in FLR amplitudes. Mann et al. [1999] suggested the generation of Pc5 pulsa-

tions driven by KH waves along the dawn magnetopause could generate a prenoon/postnoon asymmetry in FLRs, and Lee and Olson [1980] suggested that the magnetosheath magnetic field, which controls the threshold for the KH instability, can also lead to local time asymmetries. However, since the IMF B_z is due northward and held constant, the latter cannot be a source. The KH generated Pc5 pulsations are a plausible mechanism to explain why the fundamental mode would have more energy in the prenoon quadrant, however the KH waves we observe in our simulation generate Pc5 pulsations that peak at 0.5 mHz, which should not amplify FLRs Earthward of L=10. These pulsations have components in the radial and azimuthal magnetic fields with no additional discernible spectral power in the B_z component. Furthermore, these waves are evanescent and decay rapidly earthward of the magnetopause. For evanescent waves, this cannot explain the sudden reversal in the bias of FLR amplitudes towards the postnoon quadrant sunward of around L=7.

Another explanation we might suggest is that diurnal variations in ionospheric conductance could impact the resonance widths and hence the total amount of energy absorbed per wave period. However, the radial and spectral resonance widths in the prenoon and postnoon quadrants are nearly identical, and this explanation could not explain the harmonic dependence anyway. And as reported by Claudepierre et al. [2010], the radial resonance widths are not responsive to ionospheric conductivity.

Following Southwood [1974], the local density-dependent damping rate may be responsible for at least some of the observations:

$$\varepsilon = 2\left(\pi\omega\mu_0\Sigma_P\frac{1}{\rho(x_0)}\frac{d\rho(x)}{dx}\right)^{-1}. \tag{2.2}$$

As seen in Figure 2.2, the fractional change in number density shows a reduction in density earthward of L=8 in the prenoon quadrant and an increase in density up to L=8 in the postnoon quadrant. Since the amplitude of the radial electric field varies directly with the local mass density [Southwood, 1974], this explains the overall time-

dependent bias towards larger FLR amplitudes in the prenoon quadrant earthward of L=8. After inspecting the density sunward of L=7, this cannot be an explanation for the asymmetry profile seen in Figure 2.5 (b).

Even then, local mass density variations and KH waves along the dawn magnetopause cannot explain why the third harmonic has more power in the postnoon quadrant. In a cold, ideal MHD plasma there should be no damping or excitation mechanisms except for Joule heating in the ionosphere and leakage of energy downtail, which suggests that the partitioning of energy between wave modes–variations in azimuthal mode number–plays a key role. Wright et al. [1995] used numerical simulations to explore how variations in magnetopause motion impact the phase speed of the driver and its resulting frequency and azimuthal mode spectra. Since for finite wave number the poloidal and toroidal wave modes are coupled, his analysis suggests that meridional asymmetries in the phase speed of magnetopause displacements could generate an azimuthal wave number dependent asymmetry in the frequency spectra, which could explain why the third harmonic would have more energy through the partitioning of more energy into the toroidal mode in the postnoon quadrant. Following this, Lee et al. [1990] offer an explanation for the radially dependent behavior of the FLR amplitudes by suggesting the coupling location, strength and total energy can be mediated by radially-dependent azimuthal mode number spectra due to magnetospheric inhomogeneities. Without an analysis of the local time phase variations along the magnetopause and the mode numbers of each driver we cannot determine if this is the case.

Inspecting Figure 2.6 (a) shows that amidst the random variations in the time-averaged ratio of the electric fields are statistically significant time-dependent local time asymmetries as well. We observe that the degree of asymmetry in the postnoon to prenoon quadrant over the entire spectral band at L=8 decreases from about 20 percent to near parity after four hours of simulation run time. While the asymmetry in

the third harmonic at L=8, for instance, stays relatively constant, there is a persistent increase in the fundamental energy at L=6 in the dawn quadrant from about one percent after the start of the solar wind fluctuations to nearly 15 percent by the end of the simulation. Since the only time-dependent quantities are the increasing amplitude of the compressional driver and the fractional changes in the Alfvén wave speeds, we might suggest that this time-dependent asymmetry grows with the energy of the compressional driver. We cannot explain why this is the case nor why the energy in the third harmonic at L=6 shows no asymmetry until after the fifth hour when suddenly it finds preference towards the postnoon quadrant.

The radially dependent estimated coupling efficiency shows broad agreement with literature. We show additionally that the efficiency exhibits a local time asymmetry and generally increases approaching the dawn-dusk terminator, which has not previously been observed nor predicted. Inspection shows that the local time asymmetry shows a preference for the prenoon quadrant for radii less than 7 R_E, and this follows the radially-dependent asymmetry seen in the electric field ratios. Using the units for field energy shows that the total amount of energy absorbed by the standing Alfvén waves from the compressional driver is less than five percent per resonant point.

2.4 Conclusion

This study has demonstrated that the SWMF global MHD model can produce and sustain FLRs driven by broadband fluctuations in the dynamic pressure in the upstream solar wind, which validates previous studies such as Claudepierre et al. [2010]. By analyzing the ratio of the radial electric fields across the noon meridian, we also show a radial, harmonic, and time-dependent local time asymmetry in FLR amplitudes. We discussed two paradigms to account for these observations:

1. Structural mechanisms such as the azimuthal wave number, phase speed vari-

ations along the magnetopause, or local damping rate due to variations in the equatorial mass density distribution, and

2. Additional energy sources such as KH surface waves resonantly coupling to Pc5 band ULF pulsations.

In these cases, we are essentially asking why there is an asymmetry in the compressional driver and time-dependent, meriodional variations in the number density. The ultimate question, however, is whether the 10 to 20 percent difference in FLR amplitudes is significant, i.e. not due to random numerical or statistical fluctuations. We would argue that they are because they are persistent–and in some cases time-dependent, dynamic, and relatively large compared against intrinsic asymmetries one might expect in a simulation with a symmetric driver. Distinguishing the impact of these drivers on resonant mode coupling with rigorous statistical methods should be the focus of future studies.

The calculated estimated coupling efficiency we presented is a measure of the amount of spectral energy the compressional driver makes available to the radial electric field. While the total standing Alfvén wave energy includes the azimuthal magnetic field and fluid velocities, this estimate serves as a measure of the time-averaged spectral energy made available to the azimuthal drift of ions. Indeed, it is also a measure of the free wave energy made available for azimuthal acceleration. In terms of energy, at peak efficiency about 10 keV per resonant wave period is made available to ions for azimuthal acceleration. Figure 2.5 (c) bears remarkable resemblance to L-shell dependent electron intensity profiles used in radiation belt studies, and the peak coupling efficiency between 5 and 6 R_E suggests that an azimuthal electron drift resonance could be ULF wave mediated efficiently via toroidal FLRs in similar global magnetospheric simulations using two-fluid MHD. Even more, the local time asymmetry seen in the coupling efficiency predicts and offers an explanation for any azimuthal asymmetries in radiation belt intensities. This may be explored in

future studies.

Lastly, the local time and radial asymmetry seen in the fractional changes in the Alfvén wave speeds appears to be related to natural diurnal variations in equatorial mass density. However, given the remarks above concerning the coupling efficiency and the fluctuations and radially-dependent monotonic behavior seen in Figure 2.2 entertain whether this is driven by ULF wave dynamics and the amplitude asymmetries. While it is possible that the waves generated in this simulation could mediate the equatorial mass density distribution through radial diffusion, amplification of the convective electric field and azimuthal drifts, we have already concluded that the local damping rates are density dependent and would affect the FLR amplitude asymmetries as well. How these forces interact to shape the equilibrium FLR amplitudes and mass density distribution is an unresolved question.

CHAPTER III

Oblique Parametric Decay Instability of Standing Magnetospheric Surface Waves: Nonlinear Resonant Coupling to Internal Magnetotail Kink Modes

Abstract The transport of energy into the magnetosphere via nonlinear, resonant parametric wave-wave coupling between monochromatic magnetopause surface waves and magnetotail kink modes is analyzed in a global, terrestrial magnetospheric simulation in the Space Weathering Modeling Framework (SWMF). The model is driven by small, linearly increasing temperature fluctuations in a synthetic upstream solar wind driver with northward IMF B_z and bulk flow speed of 600 km/s. Near the dawn-dusk terminators, the MP surface waves with perpendicular wave-vector components $k_{x,y}$ rapidly couple to large-amplitude ($|\delta\mathbf{B}_{x,y}|/|\mathbf{B}_0| \sim 0.1 - 1$) transverse quasi-Alfvénic modes and slow magnetosonic waves that propagate azimuthally across the magnetotail toward the midnight meridian at a large angle to the mean, background field. With periods greater than 5000 seconds, the transverse waves constitute normal modes of the entire magnetotail-lobe cavity. Ponderomotive forces mediated by the beating of the magnetopause surface wave and magnetotail wave mode appear to excite the slow magnetosonic waves, while oblique propagation and

non-circular polarization generate second harmonics and sidebands. Fluctuations in the magnetopause Alfvén wave speed at 1.5 mHz are highly correlated ($\sigma > 0.95$) with the transverse MP modes with frequencies of 0.73 mHz, which suggests the standing surface waves are excited by a parametric excitation mechanism. It is unknown why the frequency of these surface waves is local time invariant. The MP waves linearly saturate without a concomitant increase in wavenumber, indicating pump depletion. Within the magnetotail, the trapped waveguide modes initially penetrate through to the midnight meridian before reflecting back toward the flanks, generating interacting, nonlinear standing wave fields characterized by near zero group speed and steepened wave structures. We measure a small, albeit non-zero net Poynting flux into the magnetotail from the magnetopause. This is the first observation of ponderomotive forces, parametric decay instabilities, second-harmonic generation, large amplitude magnetotail kink modes, the interaction of counterpropagating kink modes, and negative energy surface waves in a global magnetospheric simulation.

3.1 Introduction: Nonlinear Resonances and Internal Kink Modes in the Terrestrial Magnetosphere

Large amplitude, ULF standing and propagating Alfvén waves are often seen in the terrestrial magnetosphere as field line resonances or magnetopause surface waves [*Nosé et al.*, 1995; *Southwood and Kivelson*, 1990]. We examine the stability of magnetopause (MP) surface wave seen in simulations run with nominal solar wind conditions in the SWMF global model. We seek to determine the mechanism that permits mode coupling between the transverse MP mode and a spectrum of observed obliquely propagating transverse and longitudinal waves whose phase speeds and frequencies rule out the Alfvénic and cusp resonances. The prototypical MP surface wave for the magnetosheath flow speeds approaching solar wind speeds of 600 km/s is the

unstable, compressive Kelvin-Helmholtz wave, for which the theoretical treatment detailing their transition to spatially oscillating body modes has been constructed by generations of space physicists. Some, *Mann et al.* [1999], have suggested that in the absence of KH surface waves for an unbounded magnetosphere for flow speeds greater and less than the instability threshold, the excitation of *negative* energy waves can couple evanescently through the Alfvén resonance to field lines within the magnetosphere, which can drive the surface wave unstable, or that the coalescence of negative and positive energy surface waves can excite the KH instability. As mentioned in Chapter 1, our global model does not reproduce the KH instability, and as we will see, none of the conditions mentioned in theory that allow the coupling of surface to body modes exist in our simulation results. This chapter is devoted to examining the necessary and sufficient conditions that support the conclusion that the MP Alfvén waves seen along the dawn-dusk flanks parametrically decay into the large amplitude waveguide modes we observe in the magnetotail. We note that no numerical study has been conducted to analyze the excitation of body modes to confirm current theoretical treatments, and no specific observational or theoretical literature is available to support our conclusion. For the latter, the majority of the literature is devoted to the stability of plasma waves such as the ion cyclotron and hybrid waves, but the theory for parametric instabilities for the general class of large amplitude low frequency ($\omega < \Omega_i$) Alfvén waves is well-developed [*Sagdeev and Galeev*, 1969; *Hollweg*, 1971; *Lashmore-Davies*, 1976; *Hoshino and Goldstein*, 1989; *Ghosh et al.*, 1993].

A number of challenges complicate our analysis and differentiate it from previous global magnetospheric simulations of KH surface waves or simplified, low-dimensional box numerical models of the parametric instabilties. For the latter, most use a uniform magnetic field, whereas ours is a stressed dipole field with significant non-uniformities that permit the degeneracy of the MHD eigenmodes. These numerical models use a homogeneous plasma, but the magnetopause and magnetotail have large gradients

in density, pressure, wave speeds, and plasma beta. The mechanics of the decay of a MP surface wave is also fundamentally different from the freely-propagating pump wave seen in these models as the relative flow velocity from the stationary magnetospheric plasma and the magnetosheath generates vorticity and introduces Doppler shifted spectra. MP also carries a current, and to date, the effect the current has on the propagation and dispersion characteristics of MP surface waves has never been analyzed. The 3D spatial geometry permits oblique propagation, which is not often considered. Nor is the effect of dissipation, particularly nonlocal dissipation from resistive boundaries, such as the ionospheric footpoints. As we will see, this complicates the use of the conservation of energy as a diagnostic tool. Additionally, our geometry is bounded by the ionosphere, MP, and generally the length of the field lines, which introduces frequency selection for the daughter waves. And while field-aligned spatial gradients in the pump wave fields mediate the decay process, we focus exclusively on the equatorial plane where we are forced to infer the presence of ponderomotive forces. Lastly, every study has only considered pump waves with constant initial amplitudes. The MP surface waves we observe, however, grow exponentially from a finite perturbation.

In this chapter, we will analyze the results from one simulation supported by brief comparisons to two additional runs with different solar wind speeds and ionospheric conductances by focusing sequentially on the magnetopause, the mode coupling mechanism in the region near the MP, and the waveguide modes deep within the magnetotail, which through spatial dispersion and wave-wave interactions constitute a number of distinct wave populations. We were motivated to examine this problem because it offers an explanation for several magnetospheric phenonema:

1. The existence of discrete, "magic" frequencies in the solar wind and magnetosphere, many of which are not simple harmonics, explained by a patchwork of external and internal drivers. The parametric decay of MP surface waves offers

a unified explanation for the spectrum of frequencies.

2. Cold dense plasma sheet layer ions and hot dense ions seen in the magnetotail during quiet geomagnetic conditions for elevated solar wind speeds and northward IMF B_z have been explained by solar wind ions leaking into the low-latitude boundary layer through lobe reconnection [*Fujimoto et al.*, 2002]. However, the large-amplitude waveguide modes significantly modulate the magnetotail plasma temperature through pressure-gradient forces, and the strong field-aligned currents they generate suggest a finite k_z and field-aligned magnetic field gradients that could drive ponderomotive forces that pool ionospheric plasma into the plasma sheet. Since slow magnetosonic waves rapidly undergo Landau damping, both the introduction of cold, ionospheric ions through ponderomotive forces and local heating offer solid explanations for both phenomena.

3. ULF waves can mediate magnetotail dynamics. A time-varying guide-field– the tranverse waves with B_y components–can modulate the instability threshold and growth rate for a number of reconnection instabilities and can provide the resonant seed perturbation for ballooning-type instabilities. The local heating can also provide an additional source of free energy that can drive a marginally unstable current sheet towards reconnection onset. And generally for Alfvén waves propagating in a current-carrying plasma, the internal kink mode– observed here–typically associated with tokamak plasmas can excite sawteeth like reconnection events.

We structure the chapter as follows: section 2 addresses the methodology and overview of the results from the simulation; section 3 characterizes the surface wave modes; section 4 outlines our argument for the parametric coupling of the surface and waveguide modes; and section 5 focuses on the waveguide modes within the magnetotail. The goals herein are to: 1) establish working hypotheses for the excitation of

the the magnetopause surface waves and show there exists a negative energy mode; 2) demonstrate that the surface waves are electromagnetically coupled to the magnetotail waves, 3) show that the coupling provisionally obeys energy conservation, 4) ponderomotive forces exist, 5) the magnetotail waves are kink modes with the capacity to significantly impact magnetotail dynamics, and 6) given 1-3 establish that the coupling mechanism is through a parametric decay instability.

3.2 Methodology: Variation of Solar wind Speed, Ionospheric Conductance, and Differences in Local Plasma Properties

The simulation set-up broadly follows the design we employed to reproduce field line resonances in Chapter 2. As before, we use the SWMF global MHD model coupled with a self-consistent ionospheric electric potential solver with an inner boundary placed at 2.5 R_E [*Toth et al.*, 2005]. We set the inner boundary number density to 28 particles per cm^{-3} with an ionospheric conductance moderated by a EUV solar flux of 100×10^{-22} J/m^2 with a 5 Siemen auroral oval Pedersen conductance. We use a Cartesian grid, and SWMF solves the single-fluid, ideal MHD equations using a non-conservative, second-order Rusanov flux scheme with a 0.125 R_E grid resolution throughout the magnetospheric cavity in an Earth-centered box spanning +/- 20 R_E in the equatorial plane and +/- 10 R_E along the GSM z axis. The solar wind and IMF serve as upstream boundary conditions at 20 R_E with open boundary conditions at 92 Re in the tail and +/- 92 R_E in the y and z-directions. A Boris correction to five percent the speed of light ensures a reasonable computational efficiency, and a partially implicit time-stepping scheme with a time step of 5 seconds is used for stability and to capture all the wave dynamics within our spectral domain. The magnetic and rotational axes are aligned–there is no dipole tilt.

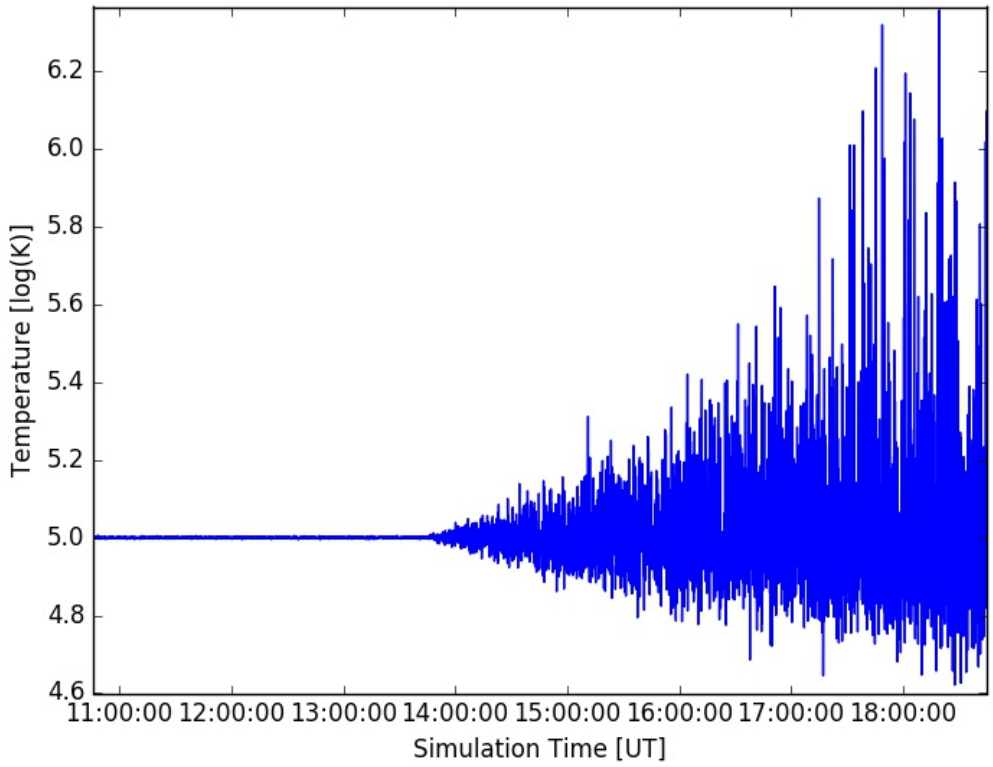

Figure 3.1: Logarithmic scale of solar wind temperature fluctuations with a linearly increasing amplitude profile after the three hour mark.

Shown in Figure 3.1, the upstream solar wind temperature profile includes broadband fluctuations between 0 and 100 mHz with a spectral resolution of 0.03 mHz. This spectral bandwidth matches the time cadence of the numerical solver. Since a small density perturbation is necessary to seed the parametric instability, we introduce random, albeit uniform noise on the order of $\delta[n,T]/[n,T] \leq 0.01$ to the upstream solar wind density (and temperature) lasting the entire run. The temperature and density fluctuations are inversely correlated, so that the thermal pressure before the onset of the temperature fluctuations does not vary, i.e., $\delta p_T(t \leq T) = 0$. The dynamic pressure fluctuations, however, are nonzero for the entire run. The solar wind generated magnetoacoustic waves are not readily observable until the last 1.5 hours of the simulation run even at the subsolar point, which allows us to make a critical

comment about the compressibility and Q factor of the magnetosheath and magnetosphere. Whether the Q factor regulates the excitation of the MP modes, parametric coupling processes, or the development of the KH instability is unknown, however, we are comfortable that the upstream thermal fluctuations do not significantly impact our results. We employ a solar wind velocity of -600 km/s and iniatilize SWMF in a steady-state mode for 5000 seconds in order to establish the magnetospheric dipole field. We note that the magnetosphere does not reach a global equilibrium state until several hours into the simulation run, and we note the presence of a transient shear flow instability at the beginning of the run resembling the KH instability. A northward IMF B_z of 5 nT is maintained for a total of 7 hours. All data are sampled at a 10 second cadence, which is more than sufficient to analyze every wave mode.

Typically for the solar wind conditions used here, we would expect to see the development of the KH instability exemplified by large-scale magnetopause displacements tailward of the dawn-dusk terminators. While we can confirm that the KH instability criterion is satisfied, the mode appears overdamped. We verify this observation by piecewise integrating $|\mathbf{u}|\hat{n}_{MP}$ in time over successive wave periods where we find that the maximum MP displacement is less than 100 km, which is much less than the dimensions of a grid cell. This confirms that the KH instability plays little to no role in the wave dynamics presented here, though we cannot rule out a marginal shear flow instability exciting small compressive fluctuations in the MP.

To examine the global wave structure and plasma properties in the equatorial plane, we plot 4 hours into the simulation where we observe the maximum penetration depth of the wave modes the magnitude of the transverse waves, $|\mathbf{B}_{x,y}|$; j_z and E_z since through $(\mathbf{j} \cdot \mathbf{E})_z$ they couple electromagnetic energy in the equatorial plane to the dissipative ionospheric boundary and contribute to the azimuthal Poynting flux; and β since it influences the admissible types of parametric instabilities and their growth rates. We also normalize the transverse waves by the mean, background

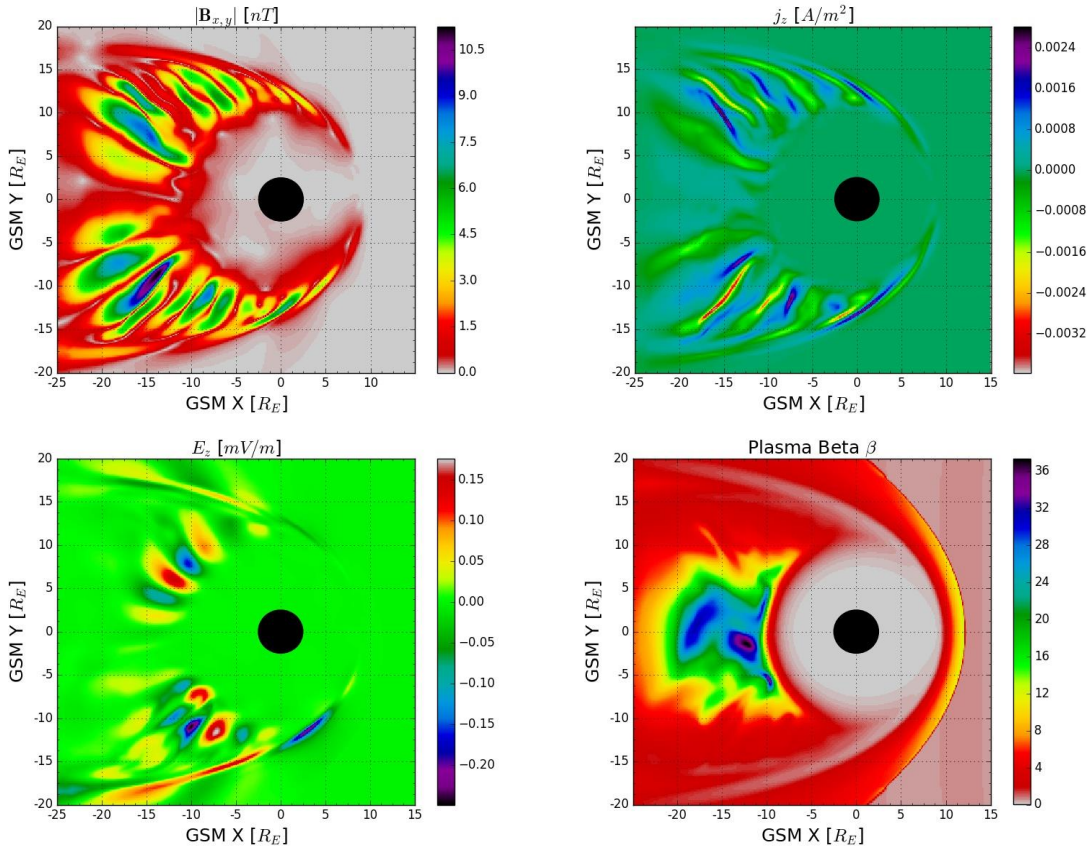

Figure 3.2: Equatorial maps, clockwise from the top left, of the magnitude of the transverse Alfvén waves, field-aligned current density, plasma beta, and field-aligned electric field at four hours into the simulation run. These snapshots occur at the maximum azimuthal extent of the magnetotail kink modes.

field, which shows that these waves are appropriately classified as *large-amplitude*. As shown, these waves can significantly modify the magnetic topology of the magnetotail, complicating the propagation characteristics and introducing nonlinear effects such as wave-steepening, shocks, and self-focusing.

To summarize the overall results of the simulation–regardless of its interpretation, Figures 3.2 and 3.3 illustrate the presence of large-scale, coherent wave fields and their associated field-aligned current fluctuations propagating along the magnetopause and into and across the magnetotail. We see little to no wave activity within the inner dipole region, and the wave fields do not extend past x=- 25 R_E downtail. A dawn-

dusk asymmetry in wave structure and amplitude is also evident, but we focus our attention on the dawn quadrant as a matter of convenience. Lastly, we see that the plasma beta along the MP is generally less than 1.

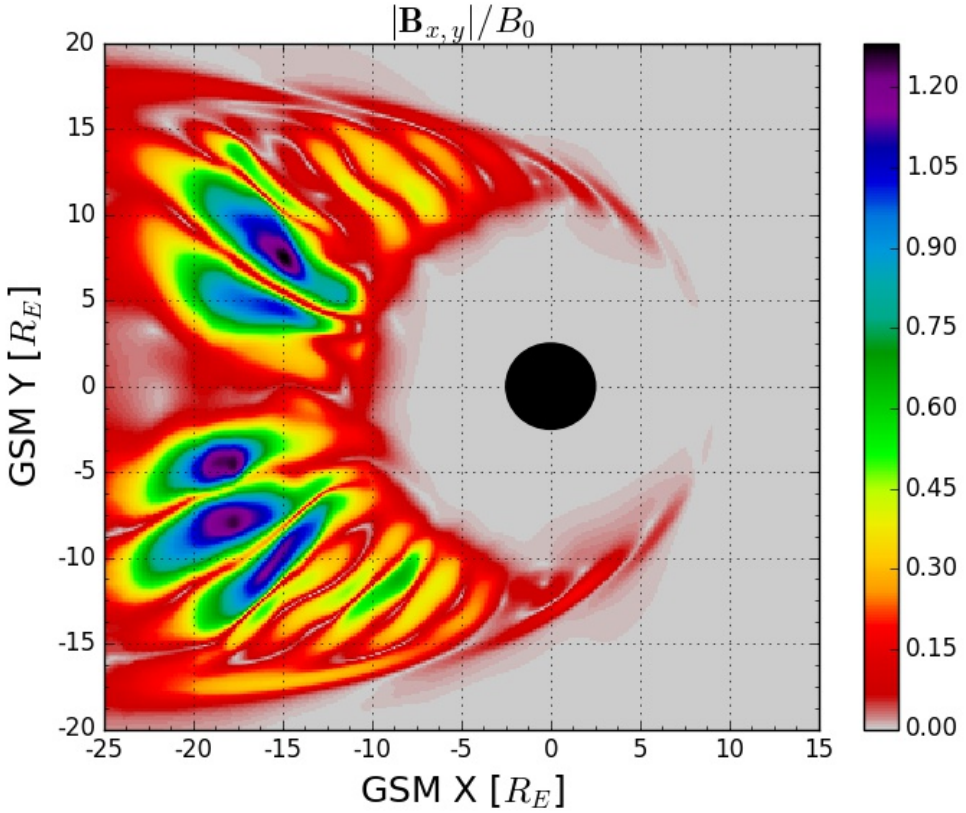

Figure 3.3: Illustration of the large-amplitude transverse Alfvén waves normalized to the background field, B_{z0}, four hours into the simulation where we observe maximum azimuthal penetration across the magnetotail. The wave distribution suggests an internal kink mode externally driven by magnetopause surface waves seen propagating tailward from the dayside.

3.3 Parametric Excitation of Standing Magnetopause Surface Waves: Mode Characteristics

To examine the characteristics of the magnetopause surface waves we observe in our simulation, we take a global and local approach first by inspecting the perturbed

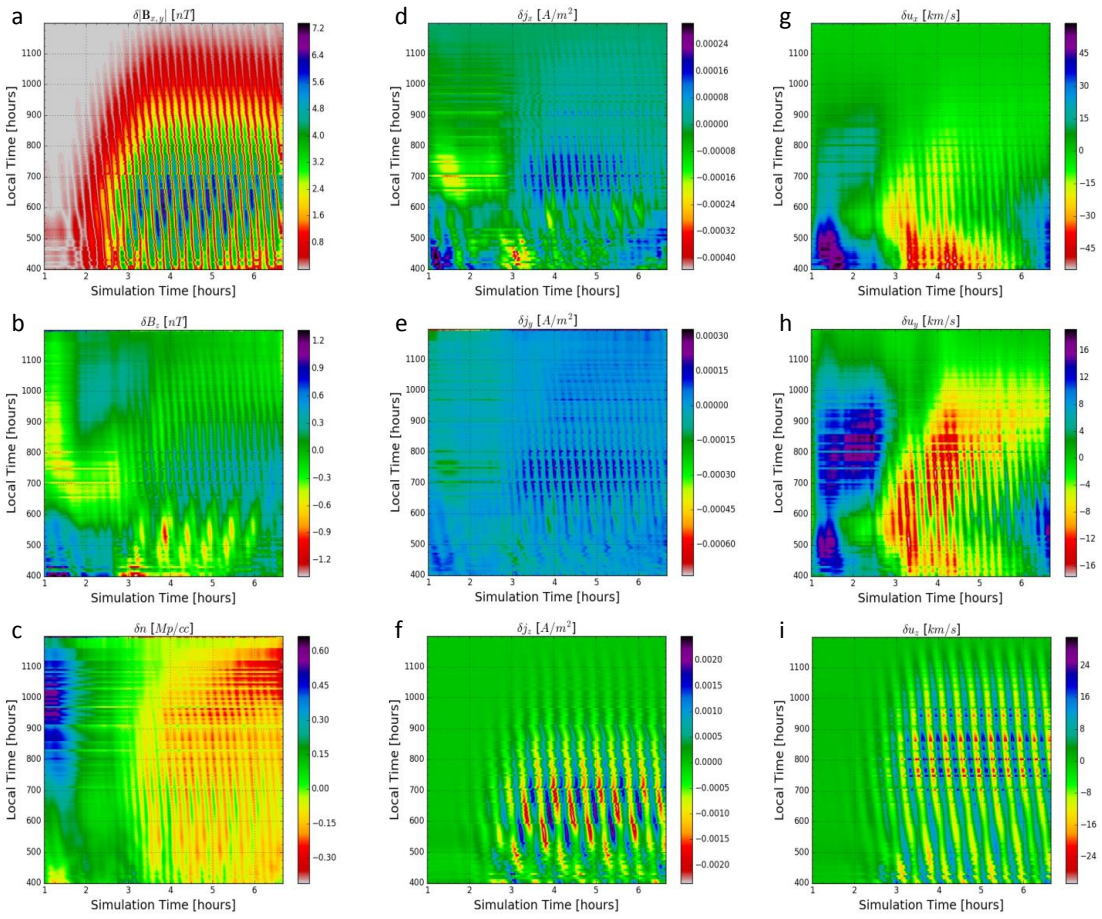

Figure 3.4: Spatiotemporal contour maps along the dawn-side magnetopause of representative detrended MHD state variables: $\delta|\mathbf{B}_{x,y}|$, δB_z, δn, δj_x, δj_y, δj_z, δu_x, δu_y, and δu_z. These data illustrate significant magnetopause surface wave structures.

wave components along the entire length of the MP and then by sampling the surface wave at points in and near the coupling region. By wave characteristics, we mean its frequency, polarization, eigenmode–fast, slow, or shear, phase speed, propagation direction (along the magnetopause, as implied), amplitude, and growth rate and saturation. Generally for plasmas with finite plasma beta, there exist two surface wave modes: an *Alfvénic* mode with principally compressive, B_z, field components with a frequency given by

$$\omega_s^2 = v_A^2 k_z^2 \left(\frac{2k_y^2 + k_z^2}{k_y^2 + k_z^2} \right), \tag{3.1}$$

and a slow magnetoacoustic wave with a frequency of

$$\omega = \frac{c_s k_z^2}{\left(k_z^2 + 2k_y^2\right)^{1/2}}. \tag{3.2}$$

We observe possibly two different wave populations along the magnetopause with frequencies differentiated roughly by these equations. However, we find that the frequencies appear invariant to the local sound and Alfvén wave speeds as they remain constant along the magnetopause, which confounds our analysis. After briefly reviewing the characteristics of these waves, we explore excitation, saturation, and damping mechanisms including the possibility that one of the wave populations is parametrically excited by the other or that they are simply vector projections of the same wave.

In Figure 3.4, we plot spatiotemporal contour plots of nine perturbed quantities related to the transverse and longitudinal components. We construct these plots by identifying the MP coordinates in the equatorial plane from the noon to 400 LT meridian by finding the maximum gradient in the magnetosheath flow speed from successive radial cuts from the inner boundary through to the magnetosheath 3 hours into the simulation. Since the time-averaged dynamic and thermal pressures are

sufficiently constant and the KH mode is damped, these coordinates do not vary as the magnetopause location is static in time. Using these coordinates, we extract the time series for every MHD state variable. The plotted variables are then detrended, $\delta x = x - < x >$.

Figure 3.4 reveals a massive amount of structure in the MP surface waves, and all of these subplots show substantial differences sunward and antisunward of the dawn terminator. Figure 3.4 (a) shows the magnitude of the $B_{x,y}$ transverse wave fields with a maximum amplitude between 500 and 700 LT. Discussed later, the onset of their excitation is well before the onset of the linearly increasing temperature fluctuations in the upstream solar wind. The wave amplitudes taper off rapidly towards the noon meridian and further tailward of 400 LT. Evidence in this subplot and others suggests the phase speed, frequency, and wavelengths are time-independent, which entails invariance to the magnetosheath flow speed. It also means the wave frequency does not vary with the local Alfvén wave speed. We see that the wavelength is approximately 10 R_E with a phase velocity of about -135 km/s antisunward. Seen in all but u_x and u_y is what appears to be a backward-propagating (sunward), amplitude-modulated wave structure with a longer period starting just tailward of the dawn terminator. The amplitude of this structure is appreciable in δB_z, and it seems to decay after the sixth hour of the simulation. This is a characteristic signature of a backward-propagating longitudinal wave mode predicted by the parametric decay of an Alfvén wave. Since the direction of its Poynting flux is opposite the direction of its group velocity, this wave has *negative* energy. After its excitation, it remains stable until it decays, an unlikely situation if resistivity were included [*Mann et al.*, 1998].

Inspecting the line plots in Figure 3.5 of the MHD state variables ($B_{x,y,z}$, n, $u_{x,y,z}$, $j_{x,y,z}$, $E_{x,y,z}$, and c_A and c_S) along the MP at 520, 600, and 640 LT, we can clearly see at least two different wave modes distinguished by wave period and a transition in wave dynamics in crossing the dawn terminator. The transverse modes have a char-

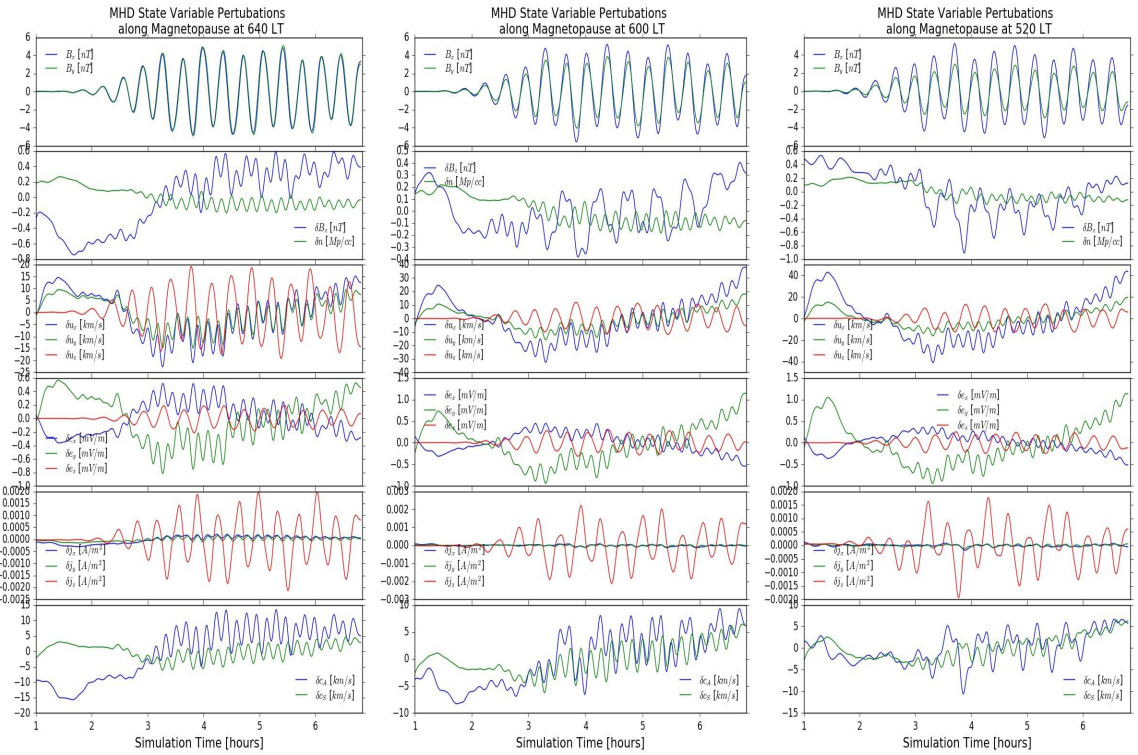

Figure 3.5: Line plots of MHD state variables sampled from within the magnetopause at 640, 600, and 520 LT. Transverse and longitudinal wave signatures are clearly distinguishable by frequency. Note the amplitude modulation in the the magnetic field and current density variables and the additional lower frequency wave component in B_z at 600 and 520 LT. These features suggest and illustrate the products of the transition to a parametrically unstable regime.

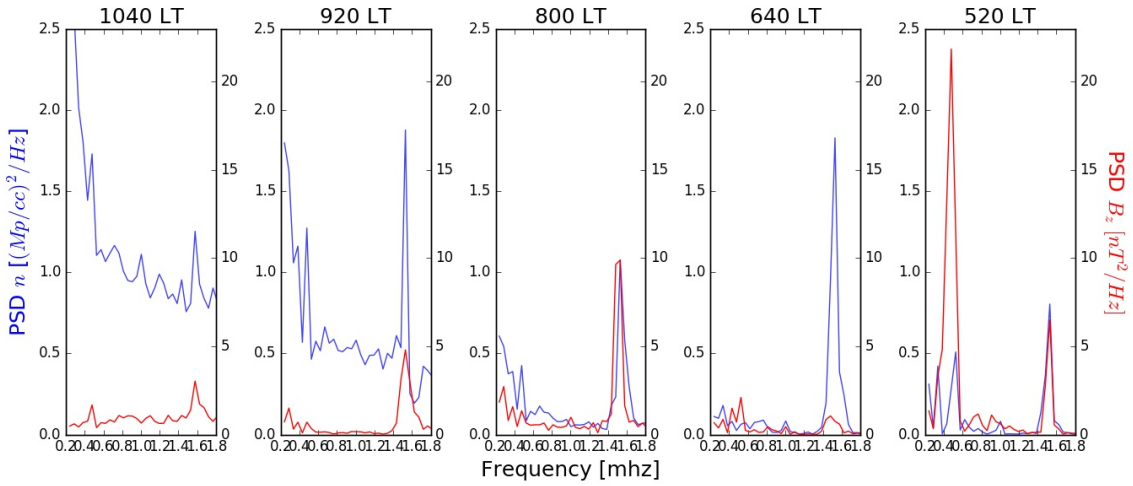

Figure 3.6: Power spectral densities of the compressional B_z field (red lines) and number density (blue line) along the magnetopause. Note the excitation of 1.5 mHz monochromatic signals in B_z and n and an additional 0.5 mHz signal in B_z near the dawn-terminator. B_z and n appear to decouple–no longer spatially linearly correlated–at 640 and 520 LT.

acteristic, spatiotemporally invariant frequency of 0.73 mHz with a slight decrease in the amplitude of B_y moving into the nightside. Comparing the phases of the number density fluctuations to the compressive B_z field shows that the longitudinal wave is a slow magnetosonic wave with both perturbations having a frequency of 1.5 mHz, twice the frequency of the transverse wave mode. The amplitudes are small, however, relative to both the transverse wave and the background dipole field. One issue that may be important is that the density wave has half the phase speed of the B_z fluctuations and twice the wavenumber even though the two are clearly coupled and phase locked. This discrepancy may be resolved by the fact that the slow magnetosonic waves are obliquely propagating, otherwise we would have to consider whether the density fluctuations constitute an ion acoustic mode. Since the x and y components of the electric field, velocity, and current density fluctuations have a dominate frequency of 1.5 mHz, we believe they are associated with the longitudinal wave with the z components being generated by the transverse wave. None of

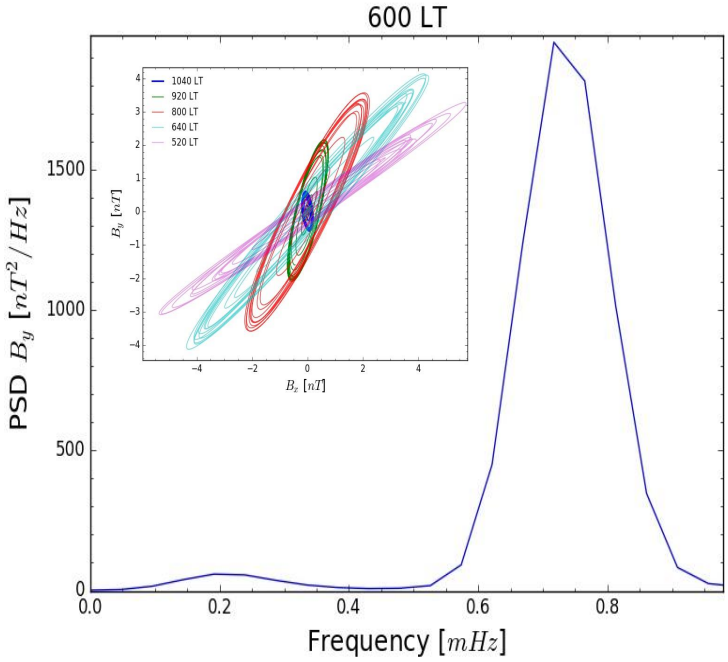

Figure 3.7: Power spectral density of transverse wave component B_y at the 600 LT meridian with an inset of the Lissajous curves of the equatorial transverse wave components sampled along the magnetopause.

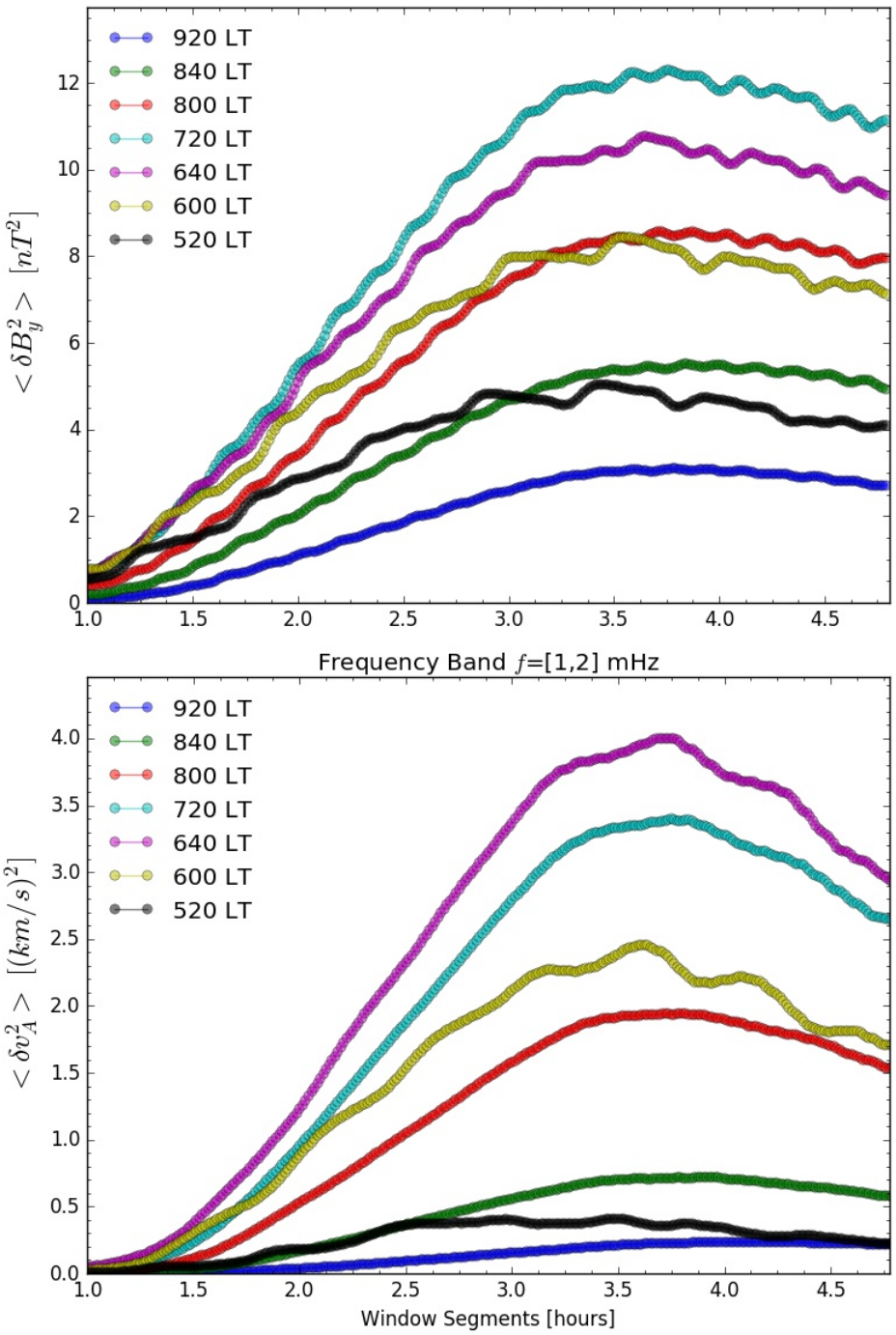

Figure 3.8: Moving time average with two hour time windows of spectral energies along the magnetopause of: *top*, B_y, and *bottom*, v_A bandpass filtered between 1 and 2 mHz. Correspondence between characteristic shapes of curves indicates strong correlation between 1.5 mHz fluctuations in the Alfvén wave speed and the 0.73 mHz fluctuations in the standing Alfvén wave modes. This may be suggestive of a nonlinear excitation mechanism.

these variables show significant amplitude or frequency modulations at the different local times. However, between 640 and 600 LT after 3 hours of simulation time, B_z acquires a larger amplitude frequency component of 0.5 mHz seen in Figure 3.4 as the backward-propagating wave structure. From 600 to 520 LT, these waves appear to decrease in amplitude after the transverse wave mode saturates between the third and fourth hour of simulation time.

In Figures 3.6 we plot the power spectral densities of B_z and n at increments of 10 degrees longitude starting from 1040 LT, and in Figure 3.7 we plot the PSD and Lissajous curves, or equatorial polarization, of the B_y component along the same LTs. There are a couple of important observations. First, all the wave modes are surprisingly monochromatic in the stationary magnetospheric frame and do not vary with local time. The Lissajous curves show that the transverse wave have a right-handed, elliptical polarization principally in B_x, which is expected for a surface wave propagating tailward along the magnetopause, and has a frequency of about 0.73 mHz [*Southwood*, 1974]. The number density shows that there is a significant amount of noise at 1040 LT relative to a small 1.5 mHz signal, but as the noise subsides the amplitude of the 1.5 mHz grows moving tailward. We see a similar trend with the B_z component, which acquires an additional signal at 0.5 mHz at 520 LT with associated density fluctuations. We note that B_z and n appear to decouple at 640 LT as generally there doesn't seem to exist a *local*, linear correlation between the amplitude of the B_z fluctuations and n. The width of these signals may be related to ionospheric conductance as we find in a simulation run with a 0.25 S conductance that the width increases significantly. One pertinent issue, however, is that there is a discrepancy between the PSD inferred frequencies, those calculated given $f = v_p/\lambda$ from measured values, and either frequency from Equations 4.1 and 4.2. In all cases, the *propagating* transverse wave modes should have a frequency greater than 1 mHz. This could imply an oblique propagation with respect to the background B_z field of

81 degrees; but if the surface wave were a standing shear Alfvén wave, then given the equatorial number density and radial distances nearest the magnetopause, we find the field line eigenfrequency–a normal mode–to be near the PSD inferred frequencies near the dawn terminator. Given the evidence mentioned earlier, however, neither explanation could be entirely accurate, and we must conclude that the sub-millihertz transverse modes are not simple normal modes.

There are a few important implications gleaned from these observations. All the wave modes acquire a finite and growing amplitude before the onset of the upstream thermal pressure fluctuations, which means some internal excitation mechanism is liable for the growth of these waves. We confirm that the growth rate of the transverse modes is initially exponential and then linear by inspection of the time derivative, and all the surface modes saturate about four hours into the simulation and then begin to decay. The 0.5 mHz backward propagating compressive wave is excited as the transverse surface wave mode saturates, and it decays as the transverse wave begins to decay as well. By plotting the magnetosheath flow speed as a function of local time in Figure 3.9, we notice that it does not become super-Alfvénic ($U_{sh} \geq c_A + c_S$) until well past the dawn terminator, so the surface waves don't simply become spatially oscillatory near where we observe the coupling between the surface and magnetospheric waves. While we do not have out-of-plane data to resolve the propagation angles, the magnetosheath flow speeds are sufficiently fast to excite fast magnetosonic waves as $U_{sh} > v_A$ from about -70 degrees longitude tailward. The point here is that the variation of the magnetosheath flow speed along the MP does not seem to control any of the observed characteristics of the wave modes.

To close, while we are confident that the dominant surface waves are transverse, with this one simulation we cannot confirm exactly what the excitation mechanism is for any of the MP surface wave modes, but any finite perturbation would excite these modes in a plasma with finite plasma beta with frequencies given by Equations

4.1 and 4.2. Whether the small, noisy density fluctuations in the upstream solar wind provides the seed perturbation or its simply the growth of an under-resolved shear flow instability is unknown. The slow magnetosonic and shear modes cannot propagate purely parallel to the magnetopause in the equatorial plane, and there is no a priori reason to conclude they propagate at the same angle; and while important, we do not have the data to determine this angle. Why this frequency does not vary along the magnetopause is confounding, however, because it suggests the waves are a global, nonlocal phenomena even if for some points along the MP the local plasma parameters and measured equatorial wavelengths support modes with the aforementioned frequencies. In either case, it seems unlikely that the slow magnetosonic surface waves somehow excite the transverse wave modes via a compressive or Alfvénic resonance due to spatial inhomogeneity within the magnetopause as their frequencies, phase speeds, and wavelengths are not equal. We can also rule out the Kruskal-Schwarzchild or magnetopause surface eigenmode, which is a standing wave with dominant compressional signatures in the equatorial plane, the opposite of what we observe. That the transverse wave appears to propagate along the magnetopause is also interesting as there is no theory within the space physics literature to explain how a transverse, nominally standing due to frequency selection, Alfvén wave can couple to adjacent field lines when its frequency is less than the Alfvén continuum. And while we can hypothesize a cogent saturation mechanism, as we will discuss later, the decay mechanism is unknown. Clearly nonlocal ionospheric dissipation and pump depletion play roles, but we would believe that the magnetosheath flow ultimately provides the free energy that drives these wave modes. And while the magnetopause has a finite width embedded within an Alfvén wave speed gradient that suggests resonance damping could come into play, no two wave modes appear to have the same frequency.

One interesting fact remains: the Alfvén wave speed, an intrinsic parameter con-

trolling the propagation characteristics of MHD waves, fluctuates at nearly twice the frequency of the transverse waves. Shown in Figure 3.8, we plot the short-time spectral energies of B_y and v_A at various local times starting from the first simulation hour using 2 hour sliding windows at 50 second increments. We bandpass filter the Alfvén wave speeds in a frequency band from 1 to 2 mHz. There are several important observations. First, the correlation coefficient between the two plots at each local time is greater than 0.95. This means the 1.5 mHz fluctuations in the Alfvén wave speed is *highly* correlated with the 0.73 mHz fluctuations in the transverse wave components. We do not see this in other frequency bands, but obviously this is observed in B_z and n. Second, the growth rates of $< \delta v_A^2 >$ and $< \delta B_y^2 >$ are local time dependent with the former generally less than half the latter.

The correlated fluctuations in the Alfvén wave speed at twice the frequency of the transverse components is the fundamental requirement for a parametric resonance, as we've discussed previously in the Chapter 1. While this condition is satisfied along the magnetopause, it does not mean that it bears out in the reality of the simulation. This is because it is entirely impossible to distinguish between the longitudinal and transverse wave signatures without more data. We can, however, use the transverse and compressive transport ratios given by

$$T_A = \frac{(\delta \mathbf{B} \cdot \delta \mathbf{B} - \delta B_{\parallel}^2)}{\delta B_{\parallel}^2} \tag{3.3}$$

and

$$T_c = \frac{P_0^2}{P^2} \frac{\delta P^2}{\delta \mathbf{B} \cdot \delta \mathbf{B}}, \tag{3.4}$$

respectively, to determine a) the relative power in the transverse and longitudinal wave modes and b) whether the longitudinal components are slow or fast magnetosonic modes. These ratios tell us exactly what we already suspected. The fact that the u_z component has the same frequency as the $B_{x,y}$ components actually implies that

these wave modes are *compressive*, where all the magnetic field components are simply projections of the same wave with the relative amplitudes determined by the ratio of the wavenumbers, k_y/k_z, which also determines the propagation angle. For the wave frequencies to be conserved across local time, the propagation angle would have to vary accordingly. Having one surface wave mode with tranverse and longitudinal components is the simplest explanation for the highly correlated Alfvén speed and (not shown) B_z to B_y wave components. And the growth rates for the longitudinal and transverse components are roughly equal, which corroborates that interpretation. In either case, as we will see, the surface wave(s) parametrically decay, exciting a number of obliquely propagating magnetotail wave modes.

3.4 Parametric Decay Instability: Excitation of Obliquely-Propagating Daughter Waves

Under certain circumstances, normally evanescent, compressive surface waves trapped within the magnetopause can become spatially oscillatory within the magnetosphere. This occurs for suitable magnetosheath flow speeds, which can excite for certain propagation angles, α, slow and fast magnetosonic waves and their corresponding slow and fast cavity modes. In the previous section we established that the magnetopause seems to support at most a longitudinal and transverse wave mode–though possibly a projection of a single wave mode–with the former definitively being a slow magnetosonic wave. While we cannot confirm what the propagation angle is without out-of-plane simulation data, let us suppose for expediency that for λ_y=$10R_E$ and λ_z=$40R_E$ such that for $\alpha = \tan^{-1}(\lambda_z/\lambda_y)$, $\alpha = 76$ degrees. For the observed magnetospheric transverse waves, λ_y=$5R_E$ so that $\alpha = 82$ degrees. Plotting the characteristic Alfvén and sound speeds along with the magnetosheath flow speeds as a function of local time in Figure 3.9 allows us to utilize previous analytical work from

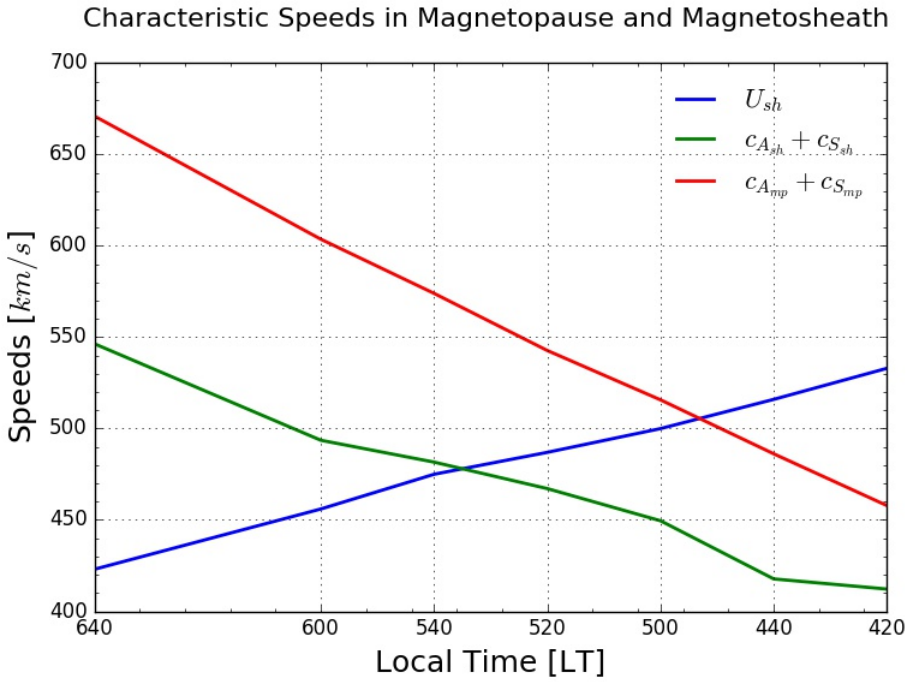

Figure 3.9: Characteristic wave and magnetosheath flow speeds sampled along local times from 640 to 420 LT. While the magnetosheath flow speed monotonically increases towards the solar wind speed of 600 km/s, the sum of the Alfvén and sound speeds decrease accordingly. Flow speeds are supersonic $U_{sh} > c_A$ all along this stretch of magnetopause but become super-Alfvénic between 540 and 500 LT. This transition allows magnetopause surface waves to become spatially oscillatory within the magnetosphere.

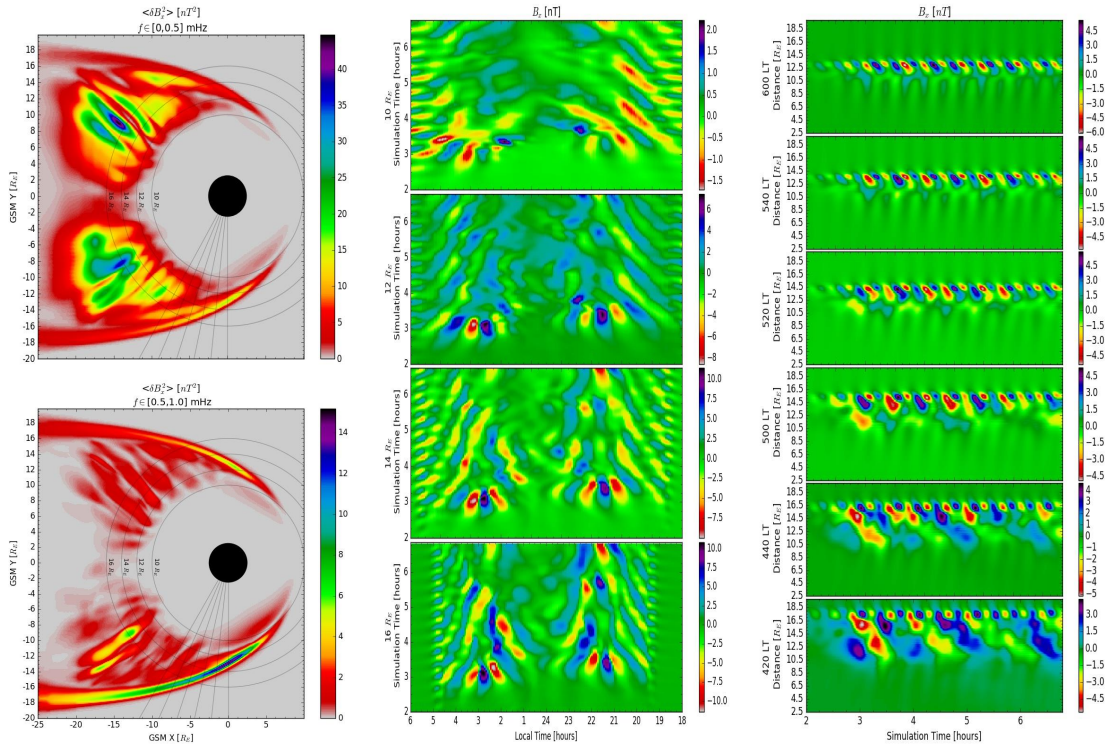

Figure 3.10: Global structure of transverse Alfvén wave component B_x in the equatorial plane illustrating the time-integrated spectral energy in two frequency bands and spatiotemporal contour plots along azimuthal and radial cuts.

Mann et al. [1998] and *Mills et al.* [1999] to confirm and characterize the magnetospheric modes we should expect to see and actually observe in our simulation. From *Mann et al.* [1998], super-Alfvénic magnetosheath flows precipitate the excitation of fast magnetosonic, overreflected waveguide modes that propagate through the magnetosphere for all α. Following *Mills et al.* [1999], fast and slow magnetosonic cavity modes are excited when $U_{sh} \sin\alpha > c_f + c_{s2}$ and $U_{sh} \sin\alpha > c_T + c_{s2}$ where c_T and c_f are the tube and fast magnetosonic speeds, respectively.

There are several notable points: a) spatially oscillatory modes are not necessarily local MHD eigenmodes as their phase speeds vary with the magnetosheath flow and wave speeds, and b) the coupling paradigm requires that for wavenumbers normal to the magnetopause that k_n passes from imaginary to finite real values, requiring what we will coin a *phase speed* resonance. Judging by Figure 3.9, near the coupling region where we observe the excitation of magnetospheric modes, the magnetosheath flow speeds are supersonic and become super-Alfvénic ($U_{sh} > v_A + c_S$ as defined by Mann et al. [1998]) between 540 and 500 LT. These flow speeds of course render the magnetopause KH unstable, so the assumption has always been that the surface waves in this regime are KH surface waves, which is actually false in our simulation. Assuming the analysis is still applicable, this points to three expectations we can glean from our simulation: the initially slow magnetosonic surface waves should transition to fast magnetosonic surface waves near and downstream of the coupling region as the magnetosheath flow speed asymptotically approaches the solar wind bulk speed of 600 km/s; since the flow is super-Alfvénic, fast and/or slow magnetosonic cavity modes should be excited; and the body modes should be overreflected–their amplitudes should grow with time.

However, analyzing the wave characteristics of the magnetotail modes reveal a few suprises. Like the magnetopause, we observe a least two, distinct wave populations each with different frequencies including a slow magnetosonic wave and a transverse

wave mode, which we verify by calculating the transverse and compressive transport ratios. Indeed, the transverse wave mode has a frequency of 0.2 mHz, phase speed of about 42 km/s, and wavelength of 5 R_E, which is almost one-fourth the frequency, one-fourth the phase speed, and one-half the wavelength of the transverse surface waves. The longitudinal magnetotail mode has a frequency of 0.5 mHz; and as we will show later, it seems to be excited through a nonlinear mechanism involving the transverse modes. Additionally, the longitudinal wave field retains its slow magnetosonic characteristics along the entire length of the magnetopause flank. Since from *Mills et al.* [1999], the lowest possible phase speed for a stable slow magnetosonic cavity mode is the tube speed, c_T, which is much larger than 42 km/s to be sure, we must reject the hypothesis that the magnetotail wave modes we observe are simply spatially oscillatory surface waves excited by sufficiently fast magnetosheath flow speeds. Note that there is no known theoretical work addressing the coupling of transverse wave modes across the magnetopause into the magnetosphere. And actually, these magnetotail waves are observed (not shown here) in similar simulations run instead with an upstream solar wind speed of 400 km/s, where the magnetosheath flow speeds do not readily approach the thresholds necessary to excite these waves. Since the frequencies–and phase speeds and wavelengths–of the surface and magnetotail modes are not equal, ruling out the Alfvén and cusp resonances, what is the coupling mechanism?

From the previous section and Chapter 1, even if we accept that the magnetopause surface waves are not parametrically excited by density and Alfvén wave speed fluctuations, these fluctuations render large-amplitude Alfvén waves unstable to nonlinear *parametric* instabilities such as the parametric decay or modulational depending on the local plasma beta and sense of polarization of the pump wave, here being the surface wave. If we accept as fact that the two wave populations are coupled near the magnetopause, which we show later, and the energy flux points into the magnetotail,

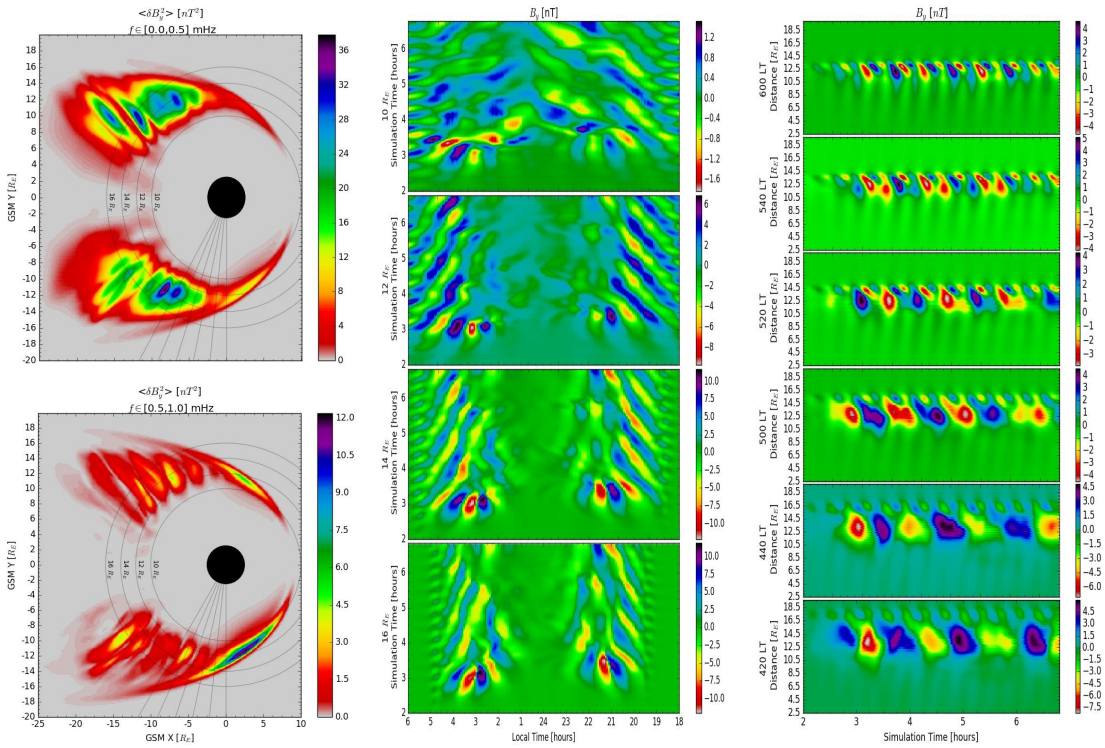

Figure 3.11: Global structure of transverse Alfvén wave component B_y in the equatorial plane illustrating the time-integrated spectral energy in two frequency bands and spatiotemporal contour plots along azimuthal and radial cuts.

then in addition to other corroborating evidence the nonlinear parametric coupling paradigm is not only tenable, but necessary and sufficient.

To examine the global equatorial structure of each wave mode both azimuthally across the magnetotail and radially through MP, we plot in Figures 3.10-3.12 spatiotemporal contour maps of δB_x, δB_y, and δB_z along arcs from 600 to 1800 LT through the magnetotail at 10, 12, 14, and 16 R_E and along radial slices from 2.5 to 19 R_E from 600 to 420 LT at 20 minute increments. We also calculate and plot the spectral energy of each wave component in spectral bands spanning at most one wave population. For the $B_{x,y}$ fields, the spectral bands are 0.0-0.5 mHz and 0.5-1.0 mHz, and 0.0-0.6 mHz and 0.6-1.8 mHz for B_z. Several features are readily apparent. In the radial cuts of Figure 3.11, we can clearly see the gradual transition from the trapped

surface wave to a spatially oscillatory wave mode of about a third of the period starting at about the 3 hour mark at 520 LT. The coupling of these two wave populations deplete the surface wave, as seen at the 420 LT meridian. The azimuthal cuts in Figures 3.10 and 3.11 show the structure of the waves after they have detached from the MP and propagated into the magnetotail; and judging by the phase speeds seen by the slopes of the wave fronts, we can identify multiple wave populations, which we discuss later. We note that B_x and B_y have different structures. This is likely due to some degree of degeneracy of these wave fields with the longitudinal modes and because of aliasing due to transforming from the natural cylindrical coordinates where we find azimuthal wave propagation to the Cartesian components. The energy maps of the transverse waves show that the wave populations are coupled at the magnetopause near the dawn terminator with the magnetotail modes containing several times more energy. As we will speculate later, this doesn't imply a violation of energy conservation as the electric field components vary inversely and the magnetotail modes may be convectively unstable or overreflected from a super-Alfvénic magnetosheath flow. The compressional signatures in Figure 3.12 show many of the same features with several important differences, as will be discussed later. The salient points are as follows: we can unmistakably visualize the coupling and transition of trapped surface waves to magnetotail modes at the magnetopause; from the phase speed, periods, and amplitudes, we can rule out cusp or Alfvénic resonances; and the magnetotail modes detach from the MP and penetrate deep into the magnetotail, ruling out several other competing interprations of the data such as buoyancy driven tail flapping or an unstable low latitude boundary layer.

To summarize our findings and ground our discussion for this section, we present the following points of argument:

1. Parametric decay or modulational instabilities with finite growth rates typically require the excitation of daughter waves that are normal modes of the plasma or

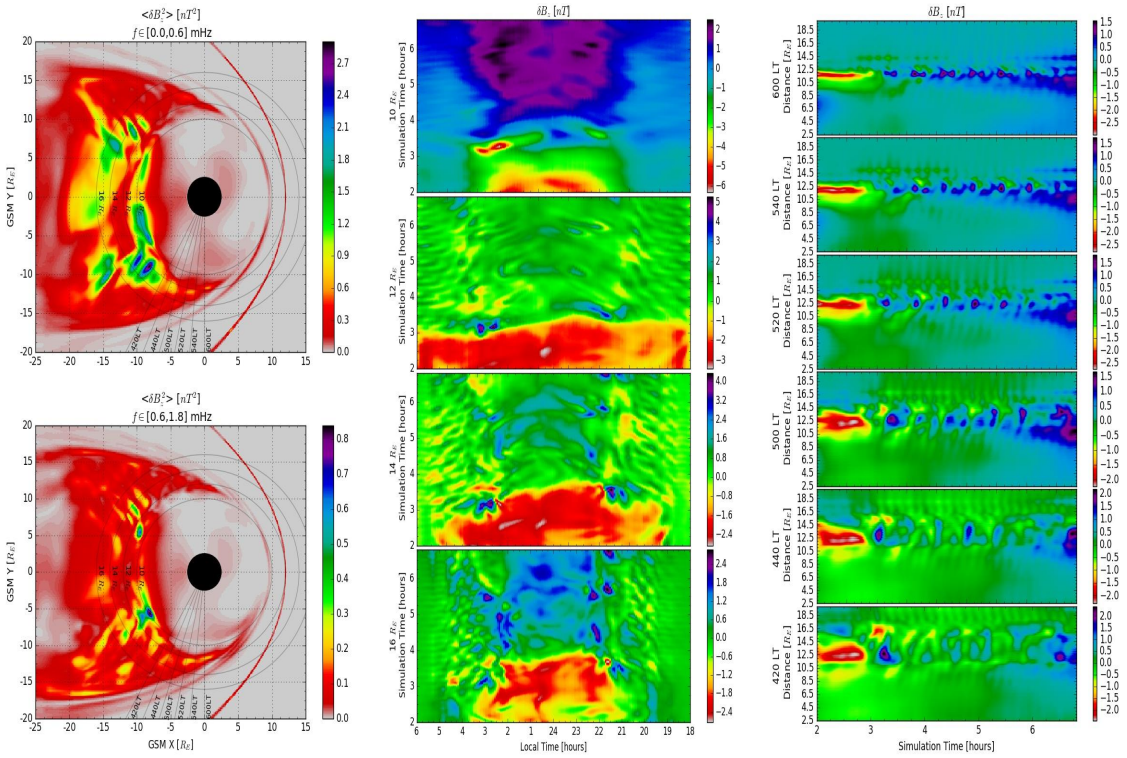

Figure 3.12: Global structure of longitudinal wave component B_z in the equatorial plane illustrating the time-integrated spectral energy in two frequency bands and spatiotemporal contour plots along azimuthal and radial cuts.

cavity. As mentioned, the transverse magnetotail wave mode frequency is $3.5\omega_0$ where ω_0 is the angular frequency of the pump wave. We note that the dispersion relations for the excitation of daughter waves from obliquely propagating pump waves with finite wavelength have not been published. While it is entirely possible that these instabilities could excite virtual modes that have frequencies that scale with the characteristic lengths of the magnetotail lobe cavity, it has also never been seen or reported before.

2. These instabilities are mediated by ponderomotive forces. We restrict our analysis to the equatorial plane, so we cannot directly determine if there are second-order field-aligned spatial gradients in the $B_{x,y}$ fields. However, the field-aligned currents imply finite k_z and since we would expect the power in the transverse waves to decrease rapidly out-of-plane, this gradient should exist. We do, however, verify that ponderomotive forces are at play by the excitation of compressional modes that are beat frequencies of the transverse pump and daughter waves.

3. Parametric coupling requires a backward propagating daughter wave with the same wavelength and either half or the same frequency as the pump wave, which is again a normal mode of the plasma. This implies the coupling spawns a negative energy surface wave. We have already observed a backward-propagating longitudinal wave in the previous section though it isn't a normal mode. Assuming the coupling efficiency between the pump and daughter waves is less than unity implies that the backward and forward propagating pump wave interact somewhere along the magnetopause, but it isn't clear what this would look like in a global MHD model without local dissipation. Basically, this implies the wavenumber of the product of this interaction goes to zero. The rapid increase in wavelength of the magnetopause surface waves tailward of the coupling region

may corroborate this interpretation.

4. This coupling paradigm depends on the amplitude modulation of the pump wave's *envelope*, and as we saw earlier, the pump/surface wave amplitude increases rapidly about 2.5 hours into the simulation. How this changes the paradigm is unkown. However, the deep-magnetotail mode excited with the initial linear growth of the surface wave has twice the amplitude and nearly four times the phase speed of the waves we see later after the surface wave saturates and begins to decay. It is unknown why this is the case.

5. Whether we are witnessing a parametric decay or modulational instability is unknown, but it should be. Insofar as these instabilities are plasma beta dependent, we actually have a strong plasma beta gradient across the magnetopause and into the magnetotail. While the plasma beta is less than 1 along the magnetopause, which means the surface waves should be unstable to the parametric decay instability, the transverse daughter wave has way more power than the longitudinal wave–a slow magnetosonic wave, which is more of a characteristic outcome of a modulational instability. That all the wave modes are phase locked is also more suggestive of a modulational instability [citation]. That can likely be reconciled by the fact that these waves do not constitute normal modes, but the discrepancy is still glaring and the impact of a plasma beta gradient is still unknown. Also, modulational instabilities require some sort of dispersion, and it is unclear whether the spatial dispersion afforded by inhomogeneities across the magnetopause are enough or what impact this has on the excitation of the daughter waves and their characteristics.

6. We have mentioned a 'coupling region' defined as the length of the magnetopause from about -80 to -100 degrees longitude where we can isolate the coupling of the magnetopause surface wave to the magnetotail modes. We have

not, however, determined why the coupling region is here and not elsewhere, or why we don't see parametric decay products within the magnetospheric cavity proper. Perhaps the 0.2 mHz daughter waves are evanescent within the cavity or that the ponderomotive forces and/or density fluctuations reach a maximum and/or threshold near the coupling region. One simulation cannot answer this question conclusively even if these hypotheses would bear out here.

3.4.1 Transverse and Longitudinal Waves: Frequency, Amplitude, and Second-Harmonic Generation

The parametric decay of the magnetopause surface waves excites a forward propagating transverse wave, seen as the kink modes propagating through the magnetotail, and a backward propagating longitudinal wave, seen in Section 4.3 as the backward propagating wave structure in Figure 3.4. Using the transport ratios discussed previously, we can confirm with confidence that the $B_{x,y}$ wave fields are transverse shear modes and the B_z wave field is a compressive, slow magnetosonic wave at 0.2 mHz and 0.5 mHz, respectively. We quickly examine the frequency and power of these wave modes near and in the magnetopause around the coupling region by plotting the 3D and 2D spectrographs along radial cuts at 640, 600, 520, and 440 LT for B_y, B_z, and n.

We can identify several wave populations in Figures 3.13-3.16. The monochromatic 0.73 mHz transverse wave lies within the magnetopause and spatially overlaps within the magnetosphere with a 0.2 mHz mode and much weaker sideband at about 0.25 mHz. The radial position of the spatial overlap between these modes corresponds with a wideband 0.5 mHz signal in B_z and n, with the former showing little wave power across all frequencies spatially co-located with the 0.2 mHz shear mode. This 'barrier' in frequency space is breached by density fluctuations with frequencies less than 0.3 mHz. Both B_z and n exhibit a 1.5 mHz signal extending from the magne-

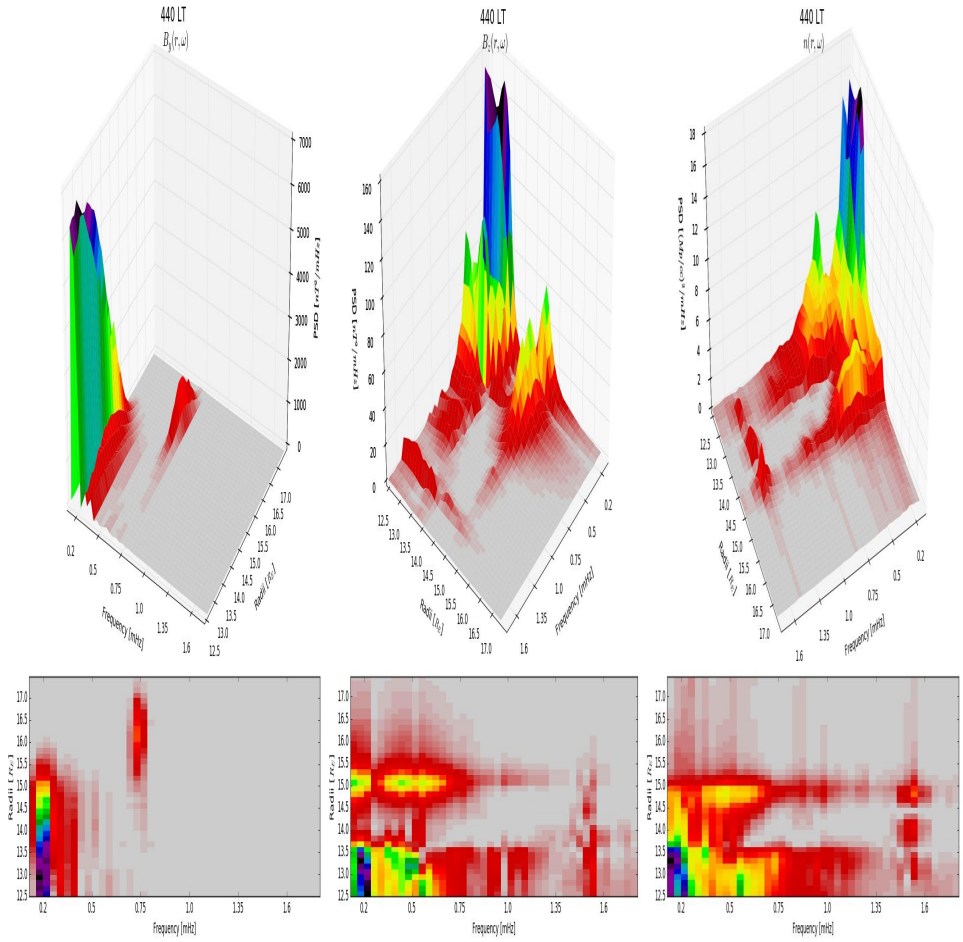

Figure 3.13: 2D and 3D spectrographs of B_y, B_z, and n at the 440 LT meridian. Refer to Figure 3.16 for details.

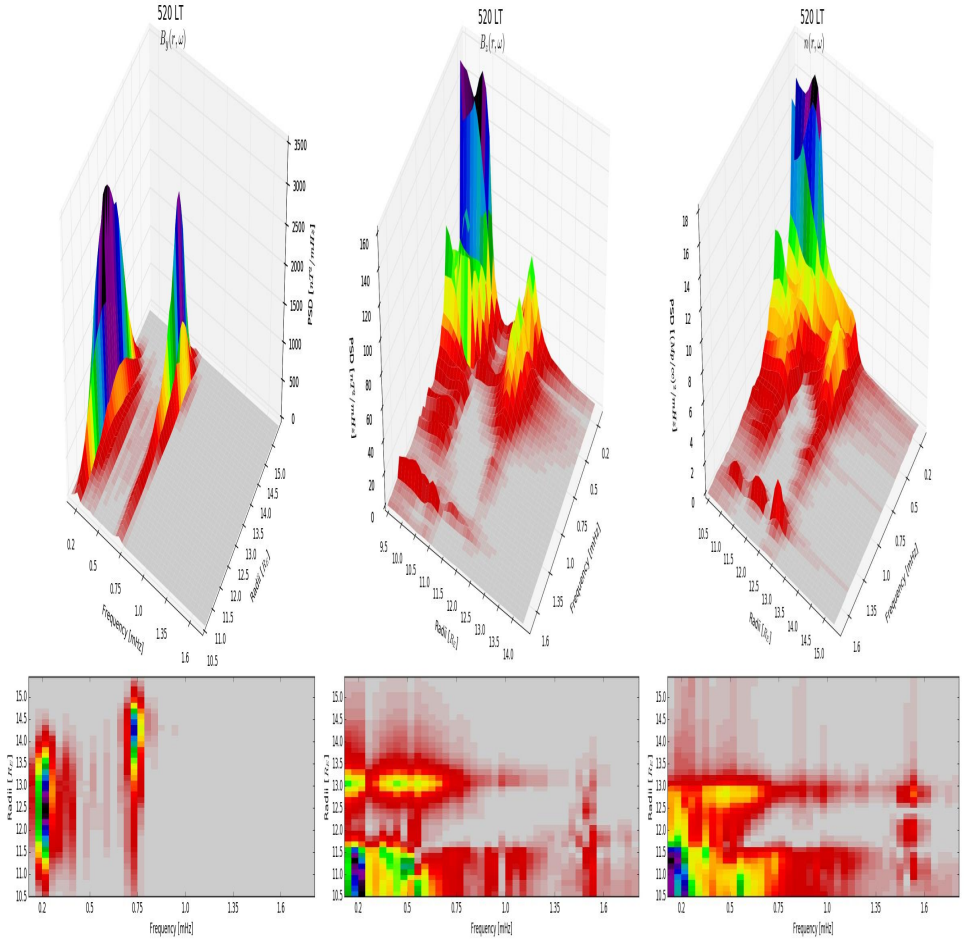

Figure 3.14: 2D and 3D spectrographs of B_y, B_z, and n at the 520 LT meridian. Refer to Figure 3.16 for details.

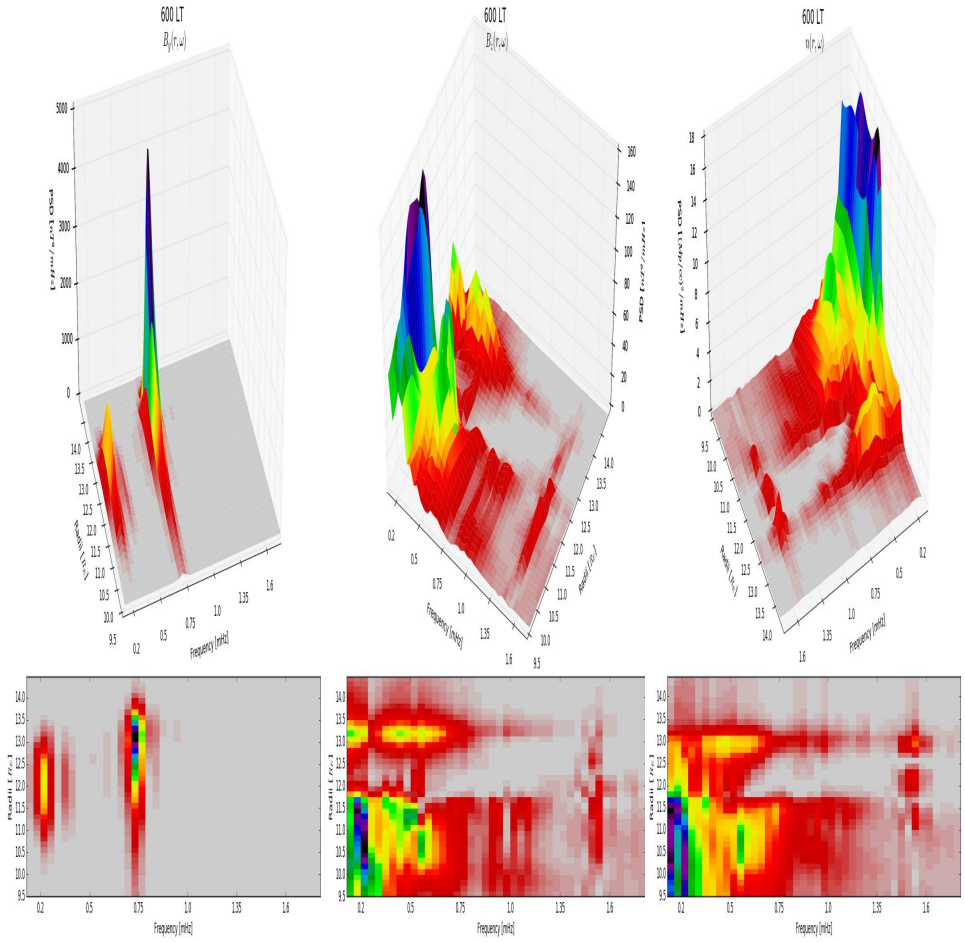

Figure 3.15: 2D and 3D spectrographs of B_y, B_z, and n at the 600 LT meridian. Refer to Figure 3.16 for details.

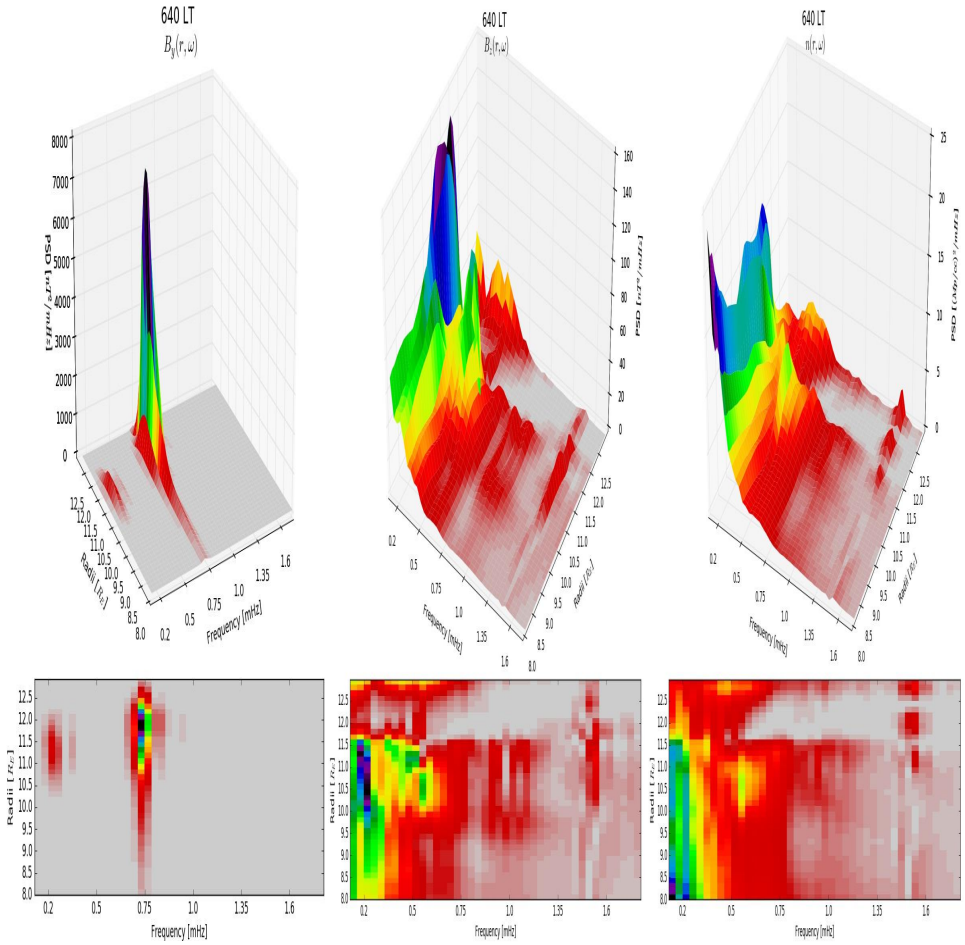

Figure 3.16: 2D and 3D spectrographs of B_y, B_z, and number density n at 640 LTs with PSDs sampled along radial segment in a neighborhood spanning several R_E of the magnetopause. The spatial overlap of the two transverse spectral signals is co-located with signicant power in the density and compressional waves at 0.5 mHz.

topause into the magnetosphere, which suggests this mode either becomes spatially oscillatory–as it is trapped along the dayside magnetopause–or it is sustained within the magnetosphere by the resonance mechanism. Furthermore, the $\omega_0 + \omega_1$ signal at 1.0 mHz has finite, but very little power, which suggests that it is an unsupportable mode, i.e., neither a normal nor virtual mode. Together, the 0.5, 1.0, and 1.5 mHz compressional signals constitute harmonics with the excitation of the 1.0 mHz ordinarily referred to as second-harmonic generation. Second-harmonic generation is thought to be due to higher-order nonlinear couplings from the non-circular polarization of the pump wave and oblique propagation, which can also generate the sidebands in the 0.2 mHz mode [*Hoshino*, 1989; *Goldstein*, 1978]. Deeper within the magnetosphere we see a broadband power spectrum in B_z and n with a <0.2 mHz high-powered signal. These signals seem to arise from large-scale changes in the magnetic topology or convective patterns rather than coherent, periodic wave activity associated with the coupling mechanism, so we ignore them.

3.4.2 Induced Density Fluctuations: Implied Ponderomotive Forces

The magnetotail and magnetopause modes have strong, negatively correlated density and compressional magnetic field fluctuations. We note the use of linear correlation measures is inconclusive and generally inadequate for mode identification as the MHD eigenmodes are degenerate for obliquely propagating waves in non-uniform magnetic topologies characteristic of the magnetotail, beyond the symmetry planes of dipole fields, and where significant nonlinear wave-wave and wave-particle interactions may occur [*Spangler et al.*, 1988]. Following *Holleweg* [1975] and *Spangler and Sheerin* [1982], we can determine if the density fluctuations are due to linear or

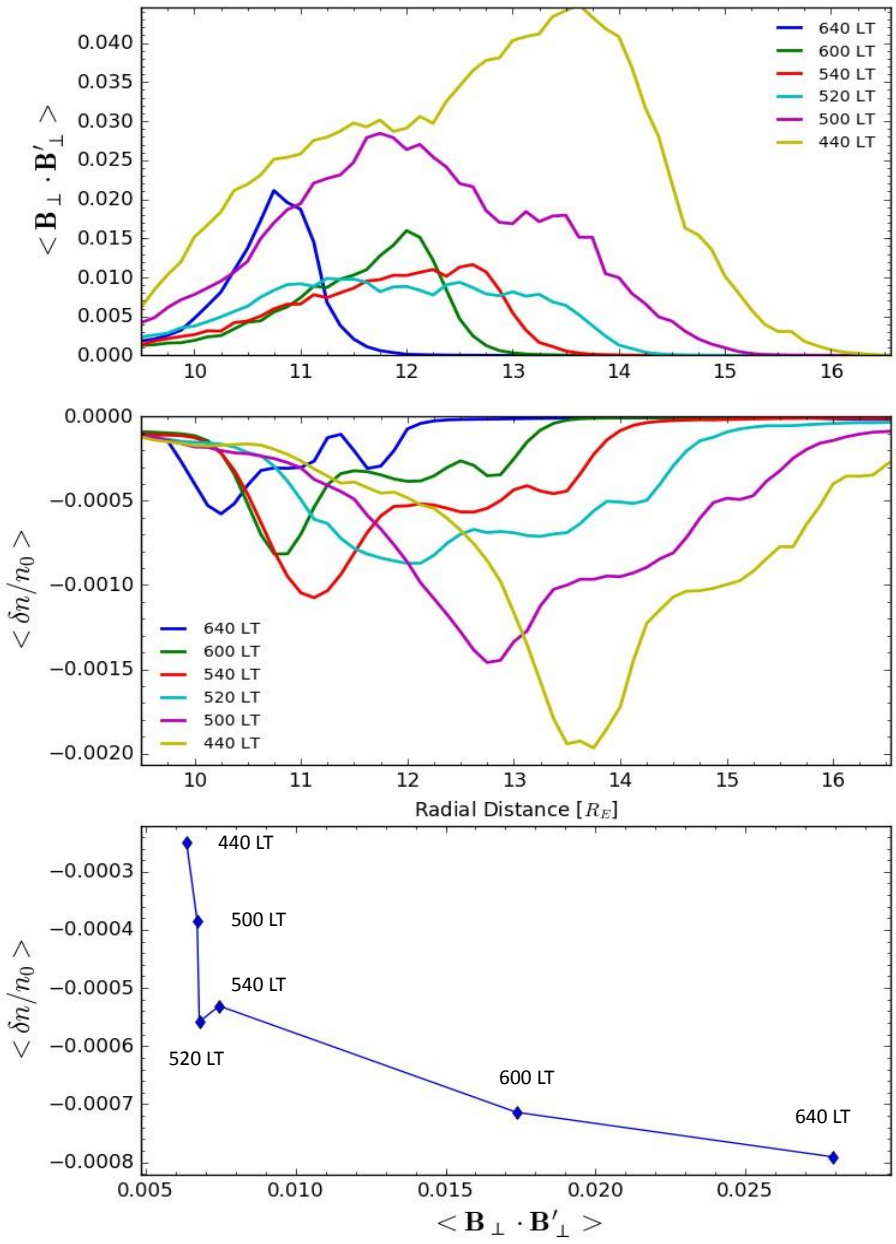

Figure 3.17: *Top*: Normalized, time-averaged density fluctuations over spectral band spanning beat frequencies of shear modes as a function of radii. *Middle*: Time-averaged projection of pump to daughter shear modes–beat waves– as a function of radii. *Bottom*: Plot of top to middle figure spatially-averaged from 10 to 16 R_E depicting expected linear relationship between induced density fluctuations and amplitude of beat waves. Linear relationship implies ponderomotive acceleration.

nonlinear forces given by

$$\frac{\delta n_0}{n} = \begin{cases} \frac{B_{x,y}}{B_{z0}} sin\theta, & \text{linear} \\ \frac{1}{2(1-\beta)} \left(\frac{B_{x,y}}{B_{z0}}\right)^2, & \text{nonlinear.} \end{cases} \tag{3.5}$$

This analysis is necessary because nonlinear forces govern how density fluctuations within the magnetopause precipitate parametric instabilities. While the density fluctuations in the magnetopause and magnetotail are small, they have a well-defined spectra with multiple harmonics. Rather than performing a nonlinear regression to fit the density perturbations, we can calculate the linear and nonlinear distance correlation measure with $B_{x,y,z}$ to determine the respective order of dependence. We find that the density fluctuations have little to no linear correlation with the compressive B_z component within the magnetopause, which we have already reported. However, the square of the perpendicular surface wave components $B_{x,y}$ show a significant negative correlation with density, which prefaces the argument that nonlinear ponderomotive forces are responsible for the coupling between the surface waves and slow magnetosonic waveguide modes.

This is so because ponderomotive forces mediate the parametric decay instability by providing an efficient means to couple spatial gradients in the magnetic energy of transverse wave modes to density and hence compressional waves. We can derive the second equation in Equation 4.5 by Fourier transforming Equation 1.37, yielding

$$\rho'(k,\omega) = \frac{\overline{\varepsilon}}{2\mu_0} \frac{k^2}{(\omega^2 - c_s^2 k^2)} \left(\overline{\mathbf{B}}_\perp \cdot \mathbf{B}'_\perp\right), \tag{3.6}$$

where the last term involves the spatial projection of the perpendicular magnetic field components of the pump into the excited daughter waves, which entails the local beating of two transverse wave modes. We note that for a normal mode, $\omega = kv_A$,

Equation 4.6 becomes

$$\frac{\delta n_0}{n} = \frac{\overline{\varepsilon}}{2(1-\beta)} \frac{\left(\overline{\mathbf{B}}_\perp \cdot \mathbf{B}'_\perp\right)}{B_0^2}. \tag{3.7}$$

This suggests the local plasma beta mediates the coupling efficiency between the transverse and longitudinal wave modes with values close to 1 generating large fluctuations in the number density regardless of the finite amplitude of the spatial overlap of the two transverse waves. It also shows that these induced density fluctuations will have positive or negative linearity for plasma beta less than and greater than 1, respectively. Even where ω isn't necessarily a normal mode, the linearity of this relation gives us an indication of the relative power between the ion acoustic or magnetosonic and transverse wave modes excited during the parametric decay. The significance of Equation 4.6 cannot be overstated.

To illustrate the number density's frequency response and to prepare the discussion later for the frequency sum rules, let us suppose the transverse waves take the form $\mathbf{B}'_\perp = B_1(x,y)\cos(\omega_0 t)$ and $\overline{\mathbf{B}}_\perp = B_0(x,y)\cos(\omega_1 t)$, then $\overline{\mathbf{B}}_\perp \cdot \mathbf{B}'_\perp = B_0 B_1 \cos(\omega_0 t)\cos(\omega_1 t)$. Using trigonometric identities shows that this becomes $B_0 B_1[\cos((\omega_0 - \omega_1)t) + \cos((\omega_0 + \omega_1)t)]$. Therefore the density fluctuations acquire frequency components of $\omega_0 - \omega_1$ and $\omega_0 + \omega_1$. For example, given that the observed pump wave frequency is 0.73 mHz and the excited transverse daughter wave frequency is 0.2 mHz gives possible density fluctuation frequencies of 0.53 and 0.93 mHz. These are the compressional signals we would expect to find near the coupling region.

To verify that there is a ponderomotive force mediating the coupling between the magnetopause surface waves and the magnetospheric wave populations, we probe near the coupling region for spatially co-located transverse wave modes with different frequencies. We take two approaches: first, examine the spectral structure of the waves seen in the two and three dimensional spectrographs shown in the previous section and then using Equation 4.7 plot $\delta n/n_0$ versus $\overline{\mathbf{B}}_\perp \cdot \mathbf{B}'_\perp$ to demonstrate collinearity.

Starting with the latter, in Figure 3.17 we plot along various local times along

a radial path within approximately +/- 3.5 R_E of the magnetopause sampled every 0.125 R_E the time-averaged product of the bandpass-filtered transverse wave modes in the 0.0-0.5 mHz and 0.5-1.0 mHz band in the top figure; the time-averaged, normalized bandpass-filtered number density fluctuations within the 0.0-1.2 mHz band in the middle figure; and those quantities *radially* averaged at each local time and plotted on each axis in the bottom figure. We employ the radial averaging as a statistical maneuver to suss out the aggregate response of the number density to the magnetic beat waves, and it clearly shows the collinearity we would expect for a ponderomotive force. The two principal regions of the curve with different slopes reflect the underlying averaged plasma beta or averaged difference in frequency between the excited wave modes and the local ion acoustic mode. However, plotting these quantities with respect to the radii, or simply plotting the top and middle figures in Figure 3.14, illustrate multiple collinear segments that reflect this difference in frequency on either side and in the magnetopause, which we know exhibits a large gradient in the sound speed.

To take the former approach, we revisit the spectrographs introduced in the previous section. Inspecting the 2D radial spectrograms of the B_y component at each local time, we note the spatial locations of the 0.73 and 0.2 mHz frequency components and the radial distance between their peak powers where the beat waves would have the greatest power. We notice that when inspecting the B_z and n spectrograms at those locations that we observe a relatively wideband 0.5 mHz signal. This together with the simple analysis above shows conclusively that the beating of the transvere pump and excited daughter waves excites a coupled density and compressional wave via the ponderomotive force. It should be made plain that in Equation 1.37 that the spatial gradient of the beat waves *along* the field line induces the field-aligned variations in number density. Thus fluctuations in magnetic energy along field lines mediate the parametric decay of the magnetopause surface waves in the equatorial

plane. In so doing, ponderomotive force modify the equilibrium density distribution along field lines, and that has massive implications for magnetospheric dynamics.

3.4.3 Mode Coupling and the Application of Conservation Laws: Conservation of Energy and Phase Space Evolution

By plotting $|\mathbf{B}|$ for the magnetopause surface and magnetotail waves near the coupling region, we verify they are spatially coupled by calculating their phase difference. Since the phase difference is zero, the wave populations are spatially correlated. This is corroborated further by presenting a plot, Figure 3.18, of their phase space evolutions, δB_y versus $d\delta B_y/dt$, which shows the coupled transition from trapped magnetopause surface waves in the first column to the excitation of the waveguide modes with a period of about $3.5\tau_0$ shown in progression from left to right at 0.5 R_E increments at various local times. The excitation of coupled modes is seen clearly by the appearance of inscribed elliptical structures just Earthward of the magnetopause with generally two embedded in a larger structure. In exception to the 500 LT row, we see a flattening of the phase space evolution as the evanescent magnetopause component decays leaving the much longer period magnetotail mode. The B_x component's (not shown) phase space distribution does not flatten to the same degree. This is important because by Liouville's theorem, energy conservation requires the conservation of phase space density. We note that the phase space evolution of the delocalized waveguide modes convected tailward vary with the local plasma conditions of the magnetotail and can be seen by inspecting the 500 LT meridian where the inscribed elliptical structures all but disappear and the distribution doesn't flatten. The propagation of these modes within the magnetotail will be discussed later.

Wave energy is conserved in parametric coupling, and the Manley-Rowe relation

$$\frac{P_1}{\omega_1} = \frac{P_2}{\omega_2}, \tag{3.8}$$

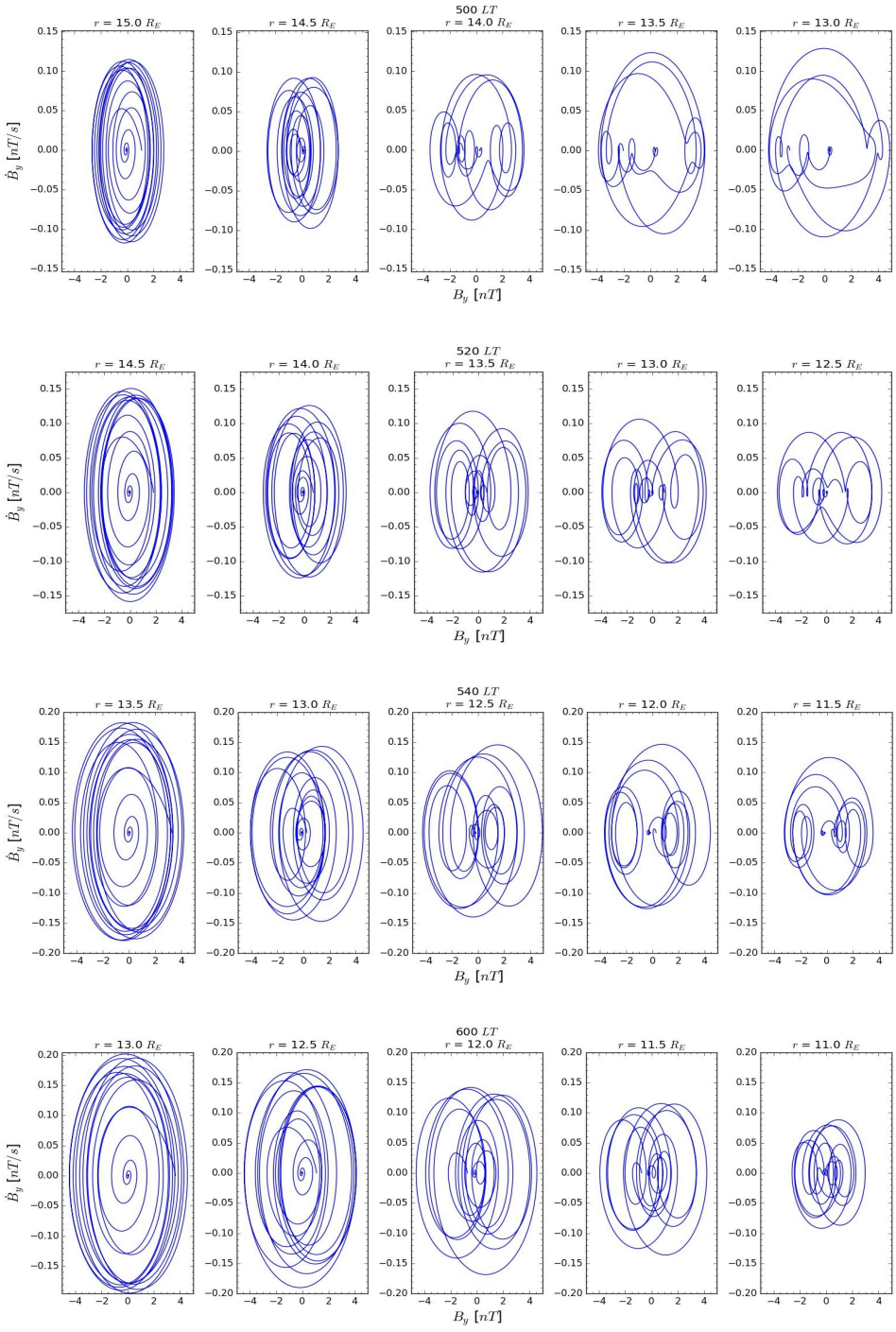

Figure 3.18: Phase space evolution of B_y component of tranverse wave modes starting from magnetopause locations–plots along first column–at 600, 540, 520, and 500 LT moving Earthward by 0.5 R_E increments. Inscribed elliptical structures indicate the presence of an additional co-propagating, coupled wave mode.

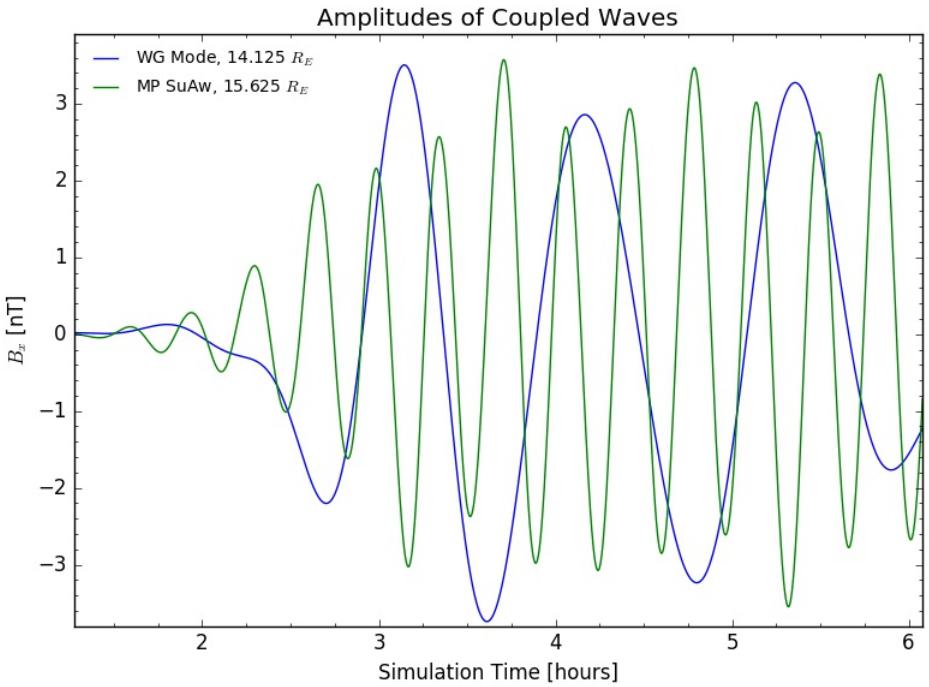

Figure 3.19: Line plots of phase-locked transverse modes along 440 LT across the magnetopause. The phase difference of nearly 0 degrees indicates mode coupling.

where $P_{1,2}$ is the power in the $B_{x,y}$ wave fields and $\omega_{1,2}$ are the respective angluar frequencies of the two coupled waves, is a statement of energy conservation. To observe if this relation holds, we calculate the power in the magnetopause surface waves and waveguide modes along radial cuts in local time tailward of the dawn terminator using the total energy density, Poynting flux, and $\mathbf{J} \cdot \mathbf{E}$ as the conserved quantities. Surprisingly, none satisfy the relation as it appears the magnetotail modes carry more energy than they should. This is unexpected as the finite ionospheric conductance acts as a nonlocal dissipation mechanism for the field-aligned wave components. Insofar as the ionospheric conductance impacts the field-aligned spatial variation of the transverse surface waves, this nonlocal dissipation should impact the local coupling, which again is mediated by ponderomotive forces, as the bounce times should be shorter than the 5000 second wave period of the tail modes. The discrepancy in wave energy should also be radially dependent as the ionospheric conductance has a small

latitudinally-dependent gradient. We can reconcile this by noting that the magnetosheath flow speeds are super-Alfvénic past the coupling region, and the wave fronts of the magnetotail modes expand into the magnetopause. In this case, they would overreflect, gaining energy from the flow.

The apparent violation of this local energy conservation law also implies that the wave frequencies would not be conserved, namely that the frequency sum rule, $\omega_0 = \omega_1 + \omega_2$, doesn't hold. For the transverse magnetopause surface wave frequency, $\omega_0 = 0.73$ mHz, and the magnetotail modes, $\omega_1 = 0.20$ mHz, the longitudinal magnetotail wave should have a frequency of $\omega_2 = 0.53$ mHz, when in fact it's observed to have significant line broadened peaked at 0.5 mHz. This discrepancy is well within error, however, so we can accept provisionally that this standard for energy conservation is satisfied. It also suggests that energy is conserved locally at the point of excitation.

There are other derivations of the Manley-Rowe relations, one of which is provided by *Hoshino et al.* [1989] given as the conserved quantity:

$$\frac{\omega_0}{k_0}|B_{k0}|^2 + \frac{\omega_1}{k_1}|B_{k1}|^2 + \frac{\omega_2}{k_2}|B_{k2}|^2 + \frac{\omega}{k}|\rho_k|^2 = constant, \tag{3.9}$$

where the ω/k terms are simply the phase speeds of the respective waves and $|B_k|^2$ is the spectral energy. Assuming the phase speeds do not spatially vary, by taking the time average of the spectral energies, we can calculate this conserved quantity at each grid cell along local times spanning the coupling region. We find that the sum of the energies are indeed roughly constant along radial paths in the neighborhood around the magnetopause and moving Earthward. This in addition to the frequency conservation gives us confidence that the coupling mechanism is via a parametric decay instability.

3.5 Magnetotail Kink Mode Waves: Propagation of Daughter Waves through Magnetotail

We identify the large amplitude, coherent wave fields carried by $B_{x,y}$ and small amplitude B_z fluctuations in the equatorial plane at sub-millihertz frequencies as transverse kink modes excited by the parametric coupling of MP surface waves. Multiple wavefronts with varying group speeds allow us to identify multiple wave populations, and with phase speeds much less than the Alfvén and sound speeds, to concur that these waves are not simple MHD eigenmodes excited locally. Using transport ratios and correlation functions, these waves are predominately obliquely propagating shear and slow magnetosonic modes, though we note that when the magnitude of the transverse fluctuations, $|\delta B_{x,y}|$ approaches the magnitude of B_{z0} the local, non-equilibrium variation in magnetic topology can alter their propagation characteristics.

Generally, these magnetotail modes all have a wavelength of about 5 R_E at least near the magnetopause. The Lissajous curves show no particular polarization. Initially the waves have a period of roughly 5000 seconds or 0.2 mHz, which is comparable to the characteristic frequency of 0.25 mHz calculated by *Horton et al.* [1998] for the magnetotail-lobe cavity, but then dispersion and wave steepening across the magnetotail introduces frequency shifts.

We distinguish these magnetotail modes from inner magnetopause surface waves by noting that the penetration depth does not vary as $L = 2\pi k$, the waves do not have elliptical or circular polarization, they decouple from the magnetopause as observed by the counterpropagating wave fields, and they lack any identifiable boundary layer that could sustain them near the midnight meridian. We concede the latter point is not evidence against a coupled LLBL mode. We also reject without rigorous analysis the hypothesis that these are simply flapping waves excited by buoyancy or magnetic field gradients given they are clearly excited by a source within the magnetopause

and propagate toward local midnight. While some studies have purported to observe waves with similar frequencies and phase/group speeds, the characteristic size of the current sheet and the vast parameter regimes that could affect those observations could lend support to most conclusions. To accept that otherwise, however, would force us to answer why the growth rate for any of the wave populations, including the magnetopause surface wave, is about the same and why the waves are excited at the same time. Note that if the frequencies of a flapping mode and a magnetopause surface wave-driven magnetotail mode were the same, the former counterfactual would be manifest, for which we would concede that it's possible that magnetopause surface waves could excite pressure-driven flapping modes.

A finite, net energy flux gives significance to the observations presented here because the energy transport from the magnetopause allows these waves to influence the dynamics of the magnetotail. For $B_{x,y}$ fields, really only the E_z electric field can affect an azimuthal transport of energy from the flanks as B_z is very small. In Figure 3.2 we see the electric field amplitudes are at most 0.25 mV/m, and while small afford a non-zero Poynting flux into the magnetotail. The finite ionospheric conductance likely plays a significant role in the dissipation these wave fields assuming the field lines here are bounded in the high-latitude ionosphere.

3.5.1 Wave Spectra and Counterpropagating Modes

There appear to be two different transverse modes: one that propagates slowly at about 40 km/s after the surface waves saturate and another that rapidly propagates across the magnetotail at several hundred km/s at the onset of saturation of the MP waves, both azimuthally away from the magnetopause towards the midnight meridian. There also exists a flankward-propagating wave population beginning about 50 degrees longitude from the midnight meridian whose origin is unknown.

Where the faster wave population encounters the slower body waves propagating

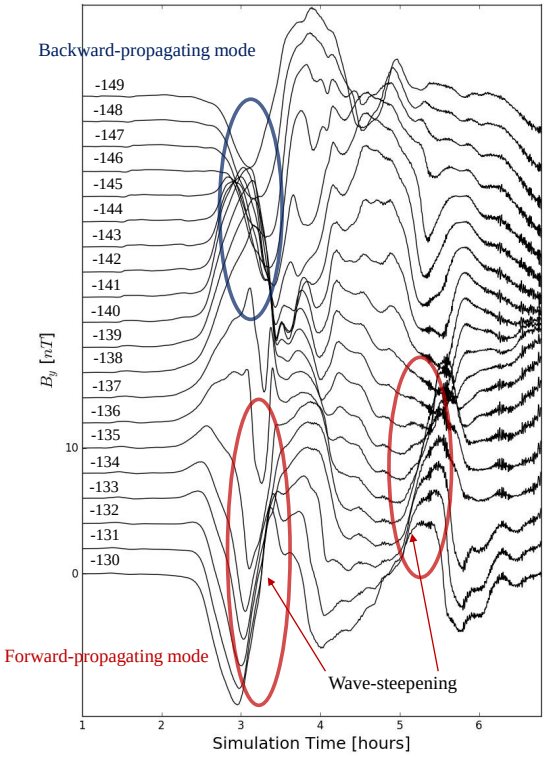

Figure 3.20: Stacked line plots of time series of B_y component from -130 to -149 degrees (bottom to top) longitude depicting amplitude structure of transverse waves as they propagate azimuthally through the magnetotail from the dawn flank. Regions of notable wave steepening of backward and forward-propagating wave populations are marked.

into the magnetotail, the interaction generates a standing wave structure characterized by near zero group velocity, seen in Figure 3.10-3.11, middle figures, as the stagnant wave front around 300 LT that extends vertically in time. In Figure 3.20, by inspecting the time delay between local times of the first amplitude peak, we can observe the transition from initially forward propagating to backward propagating transverse modes and the steeping of the wave fronts. The mechanism responsible for the reflection of the kink waves deep within the magnetotail is unknown. Typically large gradients in Alfvén wave speeds or density, plasma beta, or wave pressure from the kink modes excited along the dusk flank help comprise reflecting boundaries.

3.5.2 Induced Density and Temperature Fluctuations

Despite the lack of large-amplitude compressional waves propagating across the magnetotail, we find narrow, radial density holes with concomittant increases in B_z, E_z, and j_z all spatiotemporally localized where the transverse magnetic field amplitude is largest as seen in Figure 3.20 and 3.21. These quantities are plotted at a 16 R_E arc at -138 degrees longitude, which occurs at the intersection of the two counterpropagating transverse wave modes. The large-amplitude, quasi-periodic wave structures co-located with a compressional signal is an arrangement reminiscent of a resonance process or ponderomotive force; and in either case constitute a standing wave mode extending many R_E up-and-downstream. As we would expect in ideal MHD, we also observe a localized drop in thermal pressure. This drop in thermal pressure appears to be greater than the reduction in number density, so where the amplitude of the transverse wave fields are largest, there is an overall drop in ion temperature. These results are consistent with the propagation of a slow magnetosonic wave.

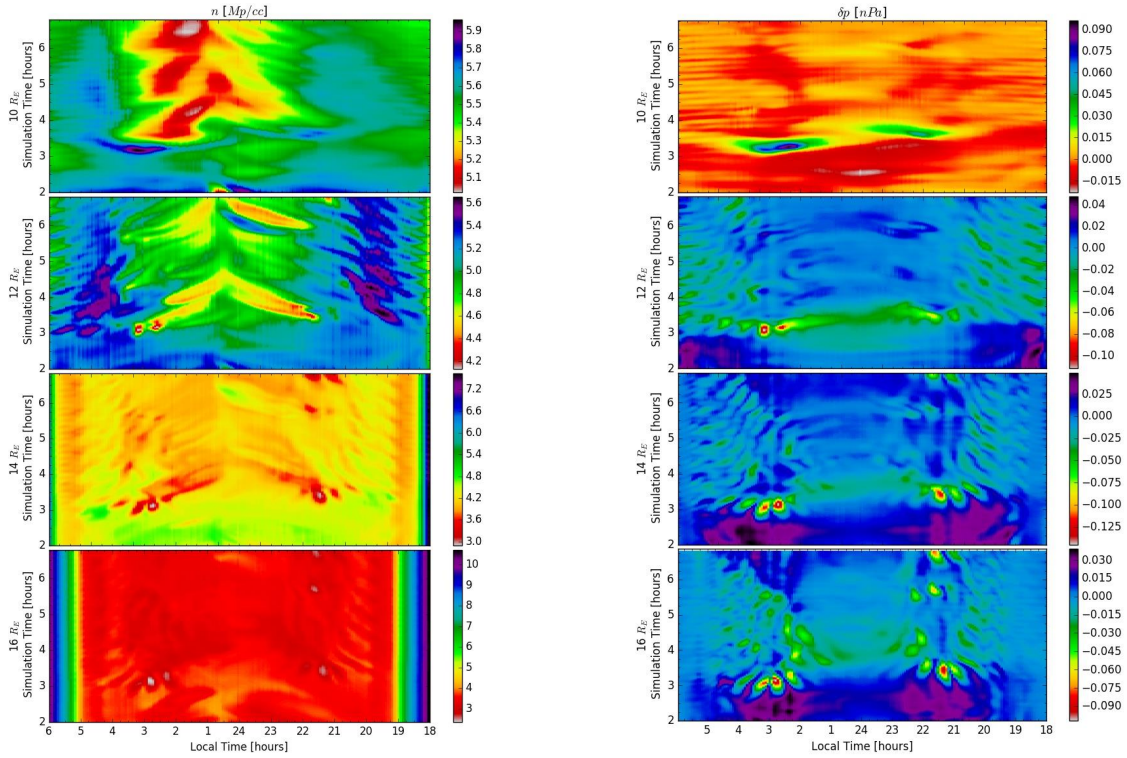

Figure 3.21: Global structure of the number density and thermal pressure taken along semi-circular rays with constant radiis of 10, 12, 14, and 16 R_E spanning from 600 to 1800 LT across magnetotail. Note the spatiotemporally localized depressions in n and p.

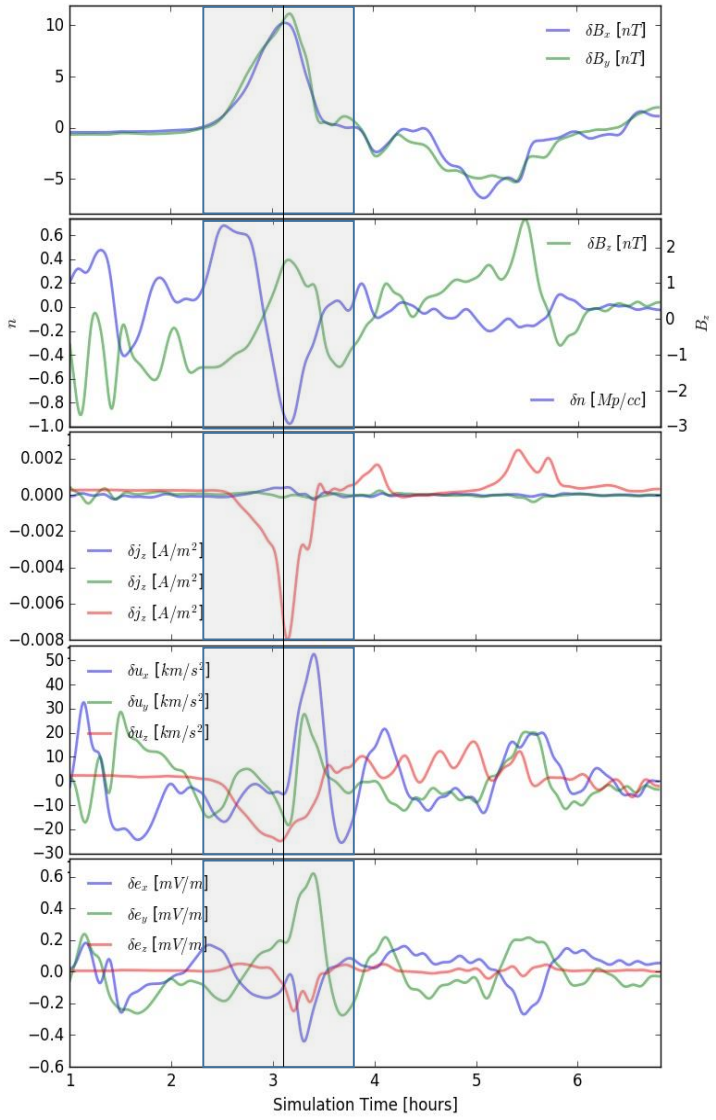

Figure 3.22: Line plots of MHD state variables at -138 degrees longitude and 16 R_E from Earth center. Shaded areas with vertical line indicate times where we observed an enhancement in the amplitude of the transverse kink modes with associated depression in number and field-aligned current densities.

3.6 Discussion and Summary: Numerical Constraints, Cold Dense Plasma Sheet Ions, Magnetotail Dynamics, and Dawn-Dusk Asymmetries

This study has attempted to explain a series of observations from a global magnetospheric simulation driven by small upstream solar wind temperature fluctuations with embedded noisy density fluctuations. We clearly identified the excitation and propagation of several wave modes propagating along the magnetopause and into and across the magnetotail. After ruling out the Kelvin-Helmholtz instability, we found convincing evidence that the dominant transverse surface waves could be parametrically excited by wave speed fluctuations at twice the frequency. After examining the induced density fluctuations and their spectra near the coupling region, we found compelling evidence that the compressive waves were excited via ponderomotive forces by the beating of the transverse surface and magnetotail modes. The magnetopause supported a backward-propagating element of this process. These ponderomotive forces were found to instigate the parametric decay of the surface waves. And after inspecting the propagation of the kink mode waves across the magnetotail, we found counterpropagating waves whose interaction led to wave steepening and the development of a standing wave structure characterized by strong field-aligned currents, number density holes, and the apparent excitation of a slow magnetosonic wave.

One of the obvious issues concerning this simulation was the lack of a Kelvin-Helmholtz instability even where the flanks were clearly KH unstable. We found that the magnetopause displacement was less than the width of a grid cell, so we wonder if these results could ever be seen in nature. Insofar as obliquely propagating surface waves introduce magnetic tension forces that stabilize the KH instability [*Mills et al*, 1999], the natural question becomes: under what circumstances could the KH instability be suppressed? And then, since the growth rate of the MP surface waves was

nearly 3 hours, how many solar wind intervals where the clock angle was identically zero and the solar wind bulk speed was 600 km/s or greater would the KH instability be suppressed and we would see the excitation of predominately transverse surface modes that parametrically decay into the nightside? Note, we haven't yet considered that the slow magnetosonic modes seen in the MP and magnetotail would rapidly Landau damp, leaving only a trace of heated ions. Even then, we must ask, how would our results change if we increased the grid resolution? Of course, in the future, using extended MHD models–resistive, Hall, two-fluid or hybrid–with less diffusive numerical schemes will be important to verify these results and then to include more self-consistent local dissipation mechanisms.

CHAPTER IV

Conclusion

To quickly summarize the main results of this study examining linear and nonlinear wave-wave interactions in global magnetospheric simulations driven by synthetic upstream solar wind drivers, we found that

1. SWMF can reproduce FLRs directly driven by fluctuations in the solar wind in a manner consistent with theoretical treatments and previous numerical studies. We found that a small, but notable and persistent dawn-dusk asymmetry in the FLR spectral energies that were not due to any intrinsic magnetospheric asymmetry or entirely to a corresponding asymmetry in the spectral energy of the compressional driver. These asymmetries were differentiated radially and across local times in frequency and through the course of the simulation. We speculated that large-scale variations in the dawn-dusk equatorial density distribution may be accounted for by corresponding variations in ionospheric damping rates, but in some cases it seemed that variations in azimuthal mode number could account for other asymmetries. We also made an attempt to estimate the local coupling efficiency between the compressional driver and shear wave modes and found broad agreement with literature on its radial profile.

2. In Chapter 3, we found that predominately transverse magnetopause surface waves were excited by an unknown mechanism unrelated to a shear-flow insta-

bility or dynamic pressure pulses. We speculated that the modulation of the wave speeds by slow magnetosonic waves at 1.5 mHz may have parametrically excited the transverse modes, which have a frequency of 0.73 mHz. We also found these surface waves were coupled to kink modes propagating azimuthally through the magnetotail. While no known coupling mechanisms made sense, we found that a parametric decay instability managed to explain every single observation including: a) the presence of a 0.5 mHz negative energy longitudinal surface wave which together with the 0.2 mHz kink modes summed to the frequency of the 0.73 mHz transverse wave, b) the 0.5 mHz wave was excited by ponderomotive forces mediated by the beating of the transverse surface and kink mode wave, and c) harmonics of the longitudinal wave and sidebands of the kink mode waves explained in theory and observation here by non-circular polarization and oblique propagation of the pump wave. Ponderomotive forces until now have never been observed in a global magnetospheric model. Additionally, the kink mode waves were found to consist of forward and backward propagating wave populations. These counterpropagating waves steepened and developed standing transverse wave structures characterized by an enhancement of field-aligned currents, density holes, and the excitation of a slow magnetosonic compressive signature.

Concerning future work, we would take two, broad approaches: using more sophisticated global models and rooting the results in Chapter 3 to a rigorous theoretical treatment. For the latter, the two fundamental problems with using ideal MHD to study Alfvén waves is there isn't a self-consistent dissipation mechanism and it doesn't admit dispersive wave modes, including waves with frequencies up to, including, and higher than the ion cyclotron frequency. This could be an issue in the case of FLRs because in kinetic treatments, kinetic Alfvén waves mediate the coupling mechanism. In other cases, ideal MHD limits the ability of ULF waves to phase mix properly

across gradients and inhomogeneities. And in the magnetopause in particular, mode conversion to high wavenumber modes is precluded entirely, even though it is a well-known mechanism controlling the mass and energy transport into the magnetosphere. By rooting our work to a more rigorous theoretical treatment, we are referring to using the available theories of parametric decay instabilities to compare against the growth and decay rates, saturation mechanisms, dependence on local plasma parameters, and excitation of harmonics and sidebands. Here there are opportunities to extend these theories to the magnetospheric domain. For instance, what if we allowed the plasma beta to vary spatially; what if we allowed the transverse wave modes to couple to the equilibrium current; or what if we allowed the mean amplitude of the pump waves to vary in time?

There are several implications for the space physics community. To summarize two from Chapter 3:

1. The large-amplitude waveguide modes significantly modulate the magnetotail plasma temperature through pressure-gradient forces, and the strong field-aligned currents they generate suggest a finite k_z and field-aligned magnetic field gradients that could drive ponderomotive forces that pool ionospheric plasma into the plasma sheet. Since slow magnetosonic waves rapidly undergo Landau damping, both the introduction of cold, ionospheric ions through ponderomotive forces and local heating offer explanations for cold and heated hydrogen and oxygen ions in the plasma sheet.

2. ULF waves can mediate magnetotail dynamics and magnetic reconnection specificially by providing a free energy source and by locally modulating wave speeds. These impacts could destabilize the current sheet to a number of reconnection instabilities or modulate the reconnection rate therein.

For more specific approaches to analyzing the work on local time asymmetries in

FLRs, we believe we have the tools to answer the mystery of the dawn-dusk asymmetries. By using more rigorous statistical methods with more simulation data, we could determine precisely if and how the equatorial density distribution impacts local dissipation rates. By using the tools in Chapter 3 to explore ponderomotive forces, we could assess the impact the beating of the shear wave modes has on the equilibrium density. And by varying solar wind conditions, we could determine if variations in the magnetopause phase speeds impact the azimuthal mode number distribution of the compressional driver and the partitioning of energy between the poloidal and toroidal FLRs. For the work on parametric decay instabilities and the supposed parametrically excitation of the transverse surface waves, we need to first increase the grid resolution to ensure the numerical solution has converged. The absence of a shear flow instability is disconcerting when the magnetopause is actually unstable to the KH instability. In either case, varying the solar wind conditions–using a southward B_z–in an attempt to control the amplitude and wave properties of the kink mode waves would be interesting because it is quite clear now that ULF waves are capable of significantly impacting magnetotail dynamics. To be sure, this work has opened the door towards studying in greater detail the interaction of ULF waves and their impact on magnetospheric dynamics.

BIBLIOGRAPHY

Alfvén, H. (1942), Existence of Electromagnetic-Hydrodynamic Waves, *Nature*, 150, 3805, 405-406.

Bellan, P.M. (1996), Mode conversion into non-MHD waves at the Alfven layer: The case against the field line resonance concept, *Journal of Geophysical Research: Space Physics*, 101(A11).

Berube, D., Moldwin, M.B., and Weygand J.M. (2003), An automated method for the detection of field line resonance frequencies using ground magnetometer techniques, *Journal of Geophysical Research: Space Physics*, 108(A9), 1348.

Cheng, C.Z., and Q. Qian (1994), Theory of ballooning-mirror instabilities for anisotropic pressure plasmas in the magnetosphere, *Journal of Geophysical Research: Space Physics*, 99(A6), 11193-11209, doi: 10.1029/94JA00657.

Chi, P.J., and C.T. Russell (1998), Phase skipping and Poynting flux of continuous pulsations, *Journal of Geophysical Research: Space Physics*, 103(A12), 29479-29491, doi: 10.1029/98JA02101.

Chian, A.C.L., Lopes, S.R., and Alves, M.V. (1994), Generation of auroral whistler-mode radiation via nonlinear coupling of Langmuir waves and Alfven waves, *Astronomy and Astrophysics*, 290, L13-L16.

Chisham, G., and Orr, D. (1997), A statistical study of the local time asymmetry of Pc5 ULF wave characteristics observed at midlatitudes by SAMNET, *Journal of Geophysical Research: Space Physics*, 102(A11), 24339-24350, doi: 10.1029/97JA01801.

Claudepierre, S. G., M. Wiltberger, S. R. Elkington, W. Lotko, and M. K. Hudson (2009), Magnetospheric cavity modes driven by solar wind dynamic pressure uctuations, Geophys. Res. Lett., 36, L13101, doi:10.1029/2009GL039045.

Claudepierre, S.G., M.K. Hudson, W. Lotko, J.G. Lyon and R.E. Denton (2010), Solar wind driving of magnetospheric ULF waves: Field line resonances driven by dynamic pressure fluctuations, *Journal of Geophysical Research: Space Physics*, 115(A11), doi: 10.1029/2010JA015399.

Claudepierre, S. G., S. R. Elkington, and M. Wiltberger (2008), Solar wind driving of magnetospheric ULF waves: Pulsations driven by velocity shear at the magnetopause, *J. Geophys. Res.*, 113, A05218, doi:10.1029/2007JA012890.

Cramer, N.F. (1977), Parametric excitation of magnetoacoustic waves by a pump magnetic field in a high β plasma, *Journal of Plasma Physics*, 17, 93-103.

Degeling, A.W., R. Rankin, K. Kabin, I.J. Rae and F.R. Fenrich (2010), Modeling ULF waves in a compressed dipole magnetic field, *Journal of Geophysical Research: Space Physics*, 115(A10), doi: 10.1029/2010JA015410.

Elkington, S. R., M. K. Hudson, and A. A. Chan (1999), Acceleration of relativistic electrons via drift-resonant interaction with toroidal-mode Pc-5 ULF oscillations, *Geophysical Research Letters*, 26, 3273.

Engebretson, M.J., L.J. Zanetti, T.A. Potemra, W. Baumjohann, H. Lhr and M.H. Acuna (1987), Simultaneous observation of Pc 3-4 pulsations in the solar wind and in the Earth's magnetosphere, *Journal of Geophysical Research: Space Physics*, 92(A9), 10053-10062, doi: 10.1029/JA092iA09p10053.

Feinrich, F.R., and J.C. Samson (1997), Growth and decay of field line resonances, *Journal of Geophysical Research: Space Physics*, 102(A9), 20031-20039, doi:10.1029/97JA01376.

Fujimoto, M. et al. (2002), Cold-dense plasma sheet and hot-dense ions in the inner-magnetosphere, *Advances in Space Research*, 30, 10, 22792288.

Glassmeier, K.H. and Stellmacher, M. (2000), Concerning the local time asymmetry of Pc5 wave power at the ground and field line resonance widths, *Journal of Geophysical Research: Space Physics*, 105(A8), 18847-18855, doi: 10.1029/2000JA900037.

Goldstein, M.L. (1978), An instability of finite amplitude circularly polarized Alfven waves, *Astrophysical Journal*, 219, 700-704.

Golovchanskaya, I. V., and Y. P. Maltsev (2005), On the identification of plasma sheet flapping waves observed by Cluster, Geophys. Res. Lett., 32.

Guo, X. C., C. Wang, and Y. Q. Hu (2010), Global MHD simulation of the Kelvin-Helmholtz instability at the magnetopause for northward interplanetary magnetic field, J. Geophys. Res., 115, A10218, doi:10.1029/2009JA015193.

Hartinger, M.D., Welling, D., Viall, N.M., Moldwin, M.B., and Ridley, A. (2014), The global structure and time evolution of dayside magnetopause surface eigenmodes, *Journal of Geophysical Research: Space Physics*, 119, 82128227.

Hasegawa, Akira (1969), Drift Mirror Instability in the Magnetosphere, *Physics of Fluids* (1958-1988), 12, 2642-2650, doi:http://dx.doi.org/10.1063/1.1692407.

Hollweg, J. V. (1975), Waves and instabilities in the solar wind, *Reviews of Geo-*

physics, 13, 263.

Horton, W., Pekker, M., and Doxas, I. (1998), Magnetic energy storage and the nightside magnetosphere-ionosphere coupling, *Geophysical Research Letters*, 25, 21, 4083-4086.

Hoshino, M., and Goldstein, M.L. (1989), Time evolution from linear to nonlinear stages in magnetohydrodynamic parametric instabilities, *Physics of Fluids B*, 1, 1405.

Hughes, W.J.: Magnetospheric ULF waves: a tutorial with a historical perspective. In: Engebretson, M.J., Takahashi, K., Scholer, M. (eds.) Solar Wind Sources of Magnetospheric Ultra-Low-Frequency Waves. American Geophysical Union Geophysical Monograph Series, vol. 81, pp. 111. American Geophysical Union, Washington, DC (1994)

Jacobs, J. A., Y. Kato, S. Matsushita, and V. A. Troitskaya (1964), Classification of geomagnetic micropulsations, J. Geophys. Res., 69(1), 180181.

Kivelson, M.G., and Russell, C.T. (1995), Introduction to Space Physics, *Cambridge University Press*.

Kivelson, M.G., and D.J. Southwood (1986), Coupling of global magnetospheric MHD eigenmodes to field line resonances, *Journal of Geophysical Research: Space Physics*, 91(A4), 4345-4351, doi: 10.1029/JA091iA04p04345.

Lee, D., and R.L. Lysak (1990), Effects of azimuthal asymmetry on ULF waves in the dipole magnetosphere, *Geophysical Research Letters*, 17(1), 53-56.

Lee, L. C., and J. V. Olson (1980), Kelvin-Helmholtz Instability and the Variation of Geomagnetic Pulsation Activity, *Geophysical Research Letters*, 7(10), 777-780.

Mann, I.R., A.N. Wright and P.S. Cally (1995), Coupling of magnetospheric cavity modes to field line resonances: A study of resonance widths, *Journal of Geophysical Research: Space Physics*, 100(A10), 19441-19456, doi: 10.1029/95JA00820.

Mann, I.R., and A.N. Wright (1999), Diagnosing the excitation mechanisms of Pc5 magnetospheric flank waveguide modes and FLRs, *Geophysical Research Letters*, 26, 16, 2609-2612, doi: 10.1029/1999GL900573.

Mann, I.R., A.N. Wright, K.J. Mills and V.M. Nakariakov (1999), Excitation of magnetospheric waveguide modes by magnetosheath flows, *Journal of Geophysical Research: Space Physics*, 104(A1), 333-353, doi: 10.1029/1998JA900026.

Merkin, V. G., J. G. Lyon, and S. G. Claudepierre (2013), Kelvin-Helmholtz instability of the magnetospheric boundary in a three-dimensional global MHD simulation

during northward IMF conditions, *J. Geophys. Res. Space Physics*, 118, 54785496, doi:10.1002/jgra.50520.

Mills, K.J., Mann, I.R. (1999), Kelvin-Helmholtz driven modes of the magnetosphere, *Physics of Plasmas*, 6, 4070-4087.

Newton, R.S., D.J. Southwood and W.J. Hughes (1978), Damping of geomagnetic pulsations by the ionosphere, *Planetary Space Sciences*, 26(3), 201-209, doi:10.1016/0032-0633(78)90085-5.

Nosé, M., Iyemore, T., Sugiura, M., and Slavin, J.A. (1995), A strong dawn/dusk asymmetry in Pc5 pulsation occurrence observed by the DE-1 satellite, *Geophysical Review Letters*, 22, 15 2053-2056, doi: 10.1029/95GL01794.

Ozeke, L. G., and I. R. Mann (2008), Energization of radiation belt electrons by ring current ion driven ULF waves, J. Geophys. Res., 113, doi:10.1029/2007JA012468.

Plaschke, F. and Glassmeier, K. H. (2011), Properties of standing Kruskal-Schwarzschild-modes at the magnetopause, *Annales Geophysicae*, 29(10), 1793-1807.

Pu, Z.-Y., and M. G. Kivelson (1983), Kelvin-Helmholtz Instability at the magnetopause: Energy flux into the magnetosphere, J. Geophys. Res., 88(A2), 853861, doi:10.1029/JA088iA02p00853.

Pu, Z.-Y., and M. G. Kivelson (1983), Kelvin:Helmholtz Instability at the magnetopause: Solution for compressible plasmas, *J. Geophys. Res.*, 88(A2), 841852, doi:10.1029/JA088iA02p00841.

Radoski, H.R., and R.L. Carovillano (1966), Axisymmetric Plasmasphere Resonances: Toroidal Mode, *Physics of Fluids*, 9(2), 285, doi: 10.1063/1.1761671.

Ridley, A. J., Crowley, G., and Freitas, C. (2000), An empirical model of the ionospheric electric potential, *Geophysical Research Letters*, 27(22), 3675-3678.

Ruderman, M. S., and A. N. Wright (1998), Excitation of resonant Alfvn waves in the magnetosphere by negative energy surface waves on the magnetopause, *J. Geophys. Res.*, 103(A11), 2657326584, doi:10.1029/98JA02296.

Sagdeev, R. Z., and Galeev, A. A., *Nonlinear Plasma Theory*, p. 7, W. A. Benjamin, New York, 1969.

Samson, J.C., B.G. Harrold, J.M. Ruohoniemi, R.A. Greenwald and A.D.M. Walker (1992), Field line reasonance associated with MHD waveguides in the magnetosphere, *Geophysics Research Letters*, 19, 441.

Sarris, T.E., T. E. Sarris, A. N. Wright and X. Li (2009), Observations and analysis of Alfvén wave phase mixing in the Earth's magnetosphere, *Journal of Geophysical Research*, 114(a3), A03218.

Shergelashvili, B.M, Zaqarashvili, T.V., Poedts, S., Roberts, B. (2004), Swing absorption of fast magnetosonic waves in inhomogeneous media, *Astronomy and Astrophysics*, 429, 767-777, doi:10.1051/0004-6361:20041494.

Southwood, D.J. (1974), Some features of field line resonances in the magnetosphere, *Planetary Space Sciences*, 22, 483-491.

Southwood, D.J., and M.G. Kivelson (1990), The magnetohydrodynamic response of the magnetospheric cavity to changes in solar wind pressure, *Journal of Geophysical Research: Space Physics*,95(a3), 2301-2309.

Spangler, S., Fuselier, S, Anderson, G., Fey, A. (1988), An observationl study of MHD wave-induced density fluctuations upstream of the Earth's bow shock, *Journal of Geophysical Research: Space Physics*, 93(A4), 845-857.

Spangler, S.R., Sheering, J.P. (1982), Properties of Alfven solitons in a finite-β plasma, *Journal of Plasma Physics*, 27, 193.

Stellmacher, M., K., Glassmeier, R.L. Lysak and M.G. Kivelson (1997), Field line resonances in discretized magnetospheric models: an artifact study, *Annals Geophysicae*, 15(6), 614-624, doi: 10.1007/s00585-997-0614-0.

Takahashi, K., T. A. Potemra, R. W. McEntire, L. J. Zanetti, and L. M. Kistler (1988), Magnetospheric ULF waves observed during the major magnetospheric compression of November 1, 1984, *Journal of Geophysical Research: Space Physics*, 93, 14,36914,382, doi:10.1029/JA093iA12p14369.

Taroyan, Y. and Erdelyi, R. Resonant and Kelvin-Helmholtz instabilities on the magnetopause, *Phys. Plasmas*, 9, 3121 (2002).

Toth, G., I.V. Sokolov, T.I. Gombosi, D.R. Chesney, C.R. Clauer, D.L. De Zeeuw, K.C. Hansen, K.J. Kane, W.B. Manchester, R.C. Oehmke, K.G. Powell, A.J. Ridley, I.I. Roussev, Q.F. Stout, O. Volberg, R.A. Wolf, S. Sazykin, A. Chan, B. Yu and J. Kta (2005), Space Weather Modeling Framework: A new tool for the space science community, *Journal of Geophysical Research: Space Physics*, 110(A12), - A12226, doi: 10.1029/2005JA011126.

Turkakin, H., R. Rankin, and I. R. Mann (2013), Primary and secondary compressible Kelvin-Helmholtz surface wave instabilities on the Earth's magnetopause, J. Geophys. Res. Space Physics, 118, 4161-4175, doi:10.1002/jgra.50394.

Wright, A.N. and Rickard G.J. (1995), ULF pulsations driven by magnetopause motions: azimuthal phase characteristics, *Journal of Geophysical Research: Space Physics*, 100(A12), 23703-23710, doi: 10.1029/95JA011765.

Yumoto, K. and Saito, T. [1982], Nonlinear resonance theory of Pc 3 Magnetic Pulsation, *Journal Geophysical Research: Space Physics*, 87(A7), 5159-5168.

Zhu, X. and Kivelson, M.G. (1988), Analytic formulation and quantitative solutions of the coupled ULF wave problem, *Journal of Geophysical Research: Space Physics*, 93(A8), 8602-8612, doi: 0.1029/JA093iA08p08602.